UNIVERSITY OF SURREY

Testing and Characterisation of Scintillator Materials for X-ray Detection



by

Daniel Packham

supervised by

Dr Annika Lohstroh

A thesis submitted in partial fulfillment for the degree of Master of Physics

in the

Faculty of Engineering and Physical Sciences
Department of Physics

February 2010

Abstract

This investigation studies some of the possible performance parameters of different scintillator materials for X-ray detection. These will be mounted onto a complementary metal-oxide semiconductor (CMOS) technology active-pixel sensor (APS) called the Large Area Sensor (LAS) in order to characterise the output scintillation light. Since the most common form of X-ray detection is to use a Photomultiplier (PM) tube, using a scintillator mounted onto a MAPS device is a rather innovative idea.

Performance parameters such as; attenuation properties, light output and spatial resolution will all be studied, with the raw data analysed using software such as MATLAB to produce clear and coherent results. Many different scintillator materials were researched with their expected performance properties discussed and displayed throughout this dissertation. Tried and tested materials however included: Bismuth Germanium Oxide, Cadmium Tungstate, Caesium Iodide, Gadolinium Oxide, Lutetium Yttrium Silicon Oxide and Zinc Tungstate. The attenuation (or stopping power) tests were carried out on all these materials, however Gadolinium Oxide was not tested further due to its amorphous nature.

The spatial resolution parameter is focused on to a larger extent than other properties as it is more difficult and time consuming to experiment upon. The thick, 1.5mm Caesium Iodide scintillator purchased from Hamamatsu Photonics Inc. resulted in a 50% image modulation of up to 3 cycles/mm spatial frequency. Other Caesium Iodide substrates mounted upon LAS confirmed very close results, especially with frame rate alteration of the sensor's software and height adjustments in the X-ray collimator head. These results were found to be better than those expected from previous published data.

The work which has been carried out in this investigation and discussed in this report subsequently lead to further funding from the Centre for Instrumentation program to continue the application for a high energy X-ray imaging detector for the I12 beamline at the Diamond Light Source. The work the author completed will also aid in developing further imaging devices within the Detector Division at the Rutherford Appleton Laboratory with the use of scintillators bonded to APS technology.

Acknowledgements

I would like to thank my supervising tutor Dr Annika Lohstroh for her help and support throughout the duration of the year's placement and her insight into the physics discussed. Also, a thank you to the staff within the physics department at the University of Surrey who helped secure this placement; Cressida Briggs, Dr Paul Sellin and Professor Paddy Regan.

I would also like to say a huge thank you to my line manager Matt Wilson and senior line manager Paul Seller in the Detector Division at the Rutherford Appleton Laboratory; for their knowledge, wisdom and patience with me over the past year. Thanks also to all my other colleagues both in the Division and outside; especially to Julien Marchal who was the contact at Diamond for the project.

A very special thank you must go to my colleague Dr Matthew Veale also with the Detector Division for all his help, encouragement and kind guidance throughout my time spent at RAL.

A final thank you must go to Go Ono, a student at the University of Bath who was also on placement with the Detector Division. A big thanks to his aid with MATLAB programming and other tasks he helped with throughout his time at RAL.

"Technological progress is like an axe in the hands of a pathological criminal."

A.Einstein

Contents

A	bstra	ct		j
A	ckno	wledge	ements	ii
P	hysic	al Con	astants	vi
A	bbre	viation	as and Scintillators	vii
1	Inti	roduct	ion	1
	1.1	RAL a	and the Detector Division	. 2
	1.2	X-ray	Radiation	. 3
	1.3	Scintil	llators	. 4
	1.4	Scintil	llation Detection	. 5
		1.4.1	The Photomultiplier tube	. 5
		1.4.2	Monolithic Active Pixel Sensors (MAPS)	. 5
	1.5	Struct	ture of the remaining Dissertation	. 7
2	Scie	entific	Background and Theory	8
	2.1	I12 De	etector Background	. 8
	2.2	Chara	cteristic X-rays	. 9
	2.3	X-ray	Interaction with Matter	. 11
		2.3.1	Photoelectric Absorption	. 12
		2.3.2	Compton Scattering	. 13
		2.3.3	Pair Production	. 14
	2.4	Scintil	llation Material	. 15
		2.4.1	Fluorescence and Phosphorescence: Luminescence	. 17
	2.5	Scintil	llation Mechanism	. 18
		2.5.1	Activators	. 19
		2.5.2	Radiation Interaction	. 20
		2.5.3	Emission and Absorption	. 22
	2.6	Other	Inorganic Scintillator measurable parameters	. 23
		2.6.1	Light Yield and Signal-to-Noise Ratio	. 23
		2.6.2	Rise and Decay Times	. 25
		2.6.3	Efficiency	. 26
	27	TAQ.	A CMOS Imaga Songar	28

Contents

		2.7.1 The Active Pixel Sensor	28
		2.7.2 LAS properties: Dynamic range, imaging area and regions of reset	31
		2.7.3 Analogue-to-Digital Conversion	33
	2.8	Spatial Resolution	35
		2.8.1 Crosstalk	35
			36
		2.8.3 Spread and Transfer Functions	
		2.8.3.1 ESF	
		2.8.3.2 The Modulation Transfer Function	
	2.9	Quantum Efficiency	
3	Ext	perimental Arrangement	11
	3.1	LabVIEW	
	9	3.1.1 Linear and Rotational Movement of LAS	
	3.2	X-ray Cabinet Upgrade and Workshop Products	
	3.3	LAS and OptoDAQ	
	0.0	3.3.1 Hardware	
		3.3.2 Software	
	3.4	Dark box set-up and Temperature Correction	
	3.5	The Silicon Pin Detector	
	3.6	Experimental Measurements	
	0.0	3.6.1 Scintillator Materials	
		3.6.2 MTF procedure	
	3.7	MATLAB	
4	Res	sults and Discussions	31
	4.1	Initial Testing and Preliminary Characterisation of LAS	32
		4.1.1 Dark Pedestal Image	
		4.1.2 Columns of Readout Error	
		4.1.3 Mask Testing with Polychromatic Light	34
		4.1.4 Temperature Dependance on Signal Output	36
	4.2	Scintillators and Characterisation of the APFPI	
		4.2.1 Researched Scintillators	7 0
		4.2.2 Amorphous GadOx and Stopping Power	73
		4.2.3 Scintillator samples courtesy of Hilger Crystals	75
	4.3	Hamamatsu Scintillators	30
		4.3.1 Frame Rate Alteration	34
		4.3.2 Spatial Resolution Measurements	35
			38
	4.4	Micron-Scale Spatial Resolution	38
	4.5	Imaging Experiments	91
		4.5.1 Imaging at Diamond	93
5	Cor	nclusions	95
	5.1	Pedestal Images and Temperature Dependance	95
	5.2	Researched Scintillators	96
	5.3	Hamamatsu Characterisations and Results	96

Contents	V

	5.4 Further Work and Summary	97
A	Workshop Sketches	99
В	OptoDAQ user manual	101
\mathbf{C}	MATLAB MTF code	116
Bi	bliography	123

Physical Constants

Abbreviations and Scintillators

ACS Amorphous-Carbon Scintillator

ADC Analogue-to-Digital Conversion

ALS Aluminium Scintillator

APFPI Active-Pixel Flat Panel Imager

APS Active-Pixel Sensor

ASIC Application-Specific Integrated Circuit

BGO Bismuth Germanium Oxide

CaF Calcium Fluoride

CCD Charged Coupled Device

CDS Correlated Double Sampling

CdWO₄ Cadmium Tungstate

CERN Conseil Europen pour la Recherche Nuclaire

CfI Centre for Instrumentation

CMOS Complementary Metal-Oxide Semiconductor

CsI Caesium Iodide

CZT Cadmium Zinc Telluride

DQE Detective Quantum Efficiency

ESA European Space Agency

ESF Edge Spread Function

 ${f eV}$ electron ${
m Volt}(s)$

FOS Fibre-Optic Scintillator

FPGA Field Programmable Gate Array

fps frames per second

FWHM Full Width at Half Maximum

GadOx Gadolinium Oxide

GSO Gadolinium Silicon Oxide

HDD Hard Disk Drive

HEXITEC High Energy X-ray Imaging Technology

IDE Integrated Drive Electronics

LaBr₃ Lanthanum Bromide

LabVIEW Laboratory Virtual Instrumentation Engineering Workbench

 \mathbf{LaCl}_3 Lanthanum Chloride

LAS Large Area Sensor

LHC Large Hadron Collider

LSB Least Significant Bit

LSF Line Spread Function

LSO Lutetium Silicon Oxide

LuAP Lutetium Aluminum Perovskite

LYSO Lutetium Yttrium Silicon Oxide

MAPS Monolithic Active Pixel Sensor

M-I³ Multidimensional Integrated Intelligence Imaging

MOS Metal Oxide Semiconductor

MOSFET Metal Oxide Semiconducting Field Effect Transistor

MTF Modulation Transfer Function

MTR Modulation Transfer Ratio

NaI Sodium Iodide

NASA National Aeronautics and Space Administration

NBWO Double Natrium-Bismuth Tungstate

NIST National Institute of Standards and Technology

PbWO₄ Lead Tungstate

PCB Printed Circuit Board

PCI Peripheral Component Interconnect

PM tube Photo-multiplier tubePSF Point Spread Function

QE Quantum Efficiency

RAL Rutherford Appleton Laboratory

ROI Region Of Interest
ROR Region Of Reset

RS Row Select

SF Source Follower

SNR Signal-to-Noise Ratio

STFC Science and Technology Facilities Council

VI Visual Instrument

XFEL X-ray Free Electron Laser

YAP Yttrium Aluminium Perovskite

YSO Yttrium Silicon Oxide

ZnSe Zinc SelenideZnWO₄ Zinc Tungstate

Chapter 1

Introduction

The Testing and Characterisation of Scintillator Materials for X-ray Detection is a new research project for the Detector Division at the Rutherford Appleton Laboratory (RAL). The aim of the project is to study a position sensitive, high energy X-ray diffraction detector developed for use on beamline I12 at the Diamond Light Source. The Diamond Light Source at RAL on the Harwell Science and Innovation Campus is the UK national synchrotron facility. A synchrotron will generate beams of light from infra-red to X-ray wavelengths (called synchrotron light) where they are detected in experimental stations known as beamlines [1]. The project is funded by the Centre for Instrumentation (CfI) which is a key area for the Science and Technology Facilities Council (STFC) to develop capability for science and industry. The CfI undertakes strategic research to provide for the future instrumentation needs of the UK Research Councils, funding major research and development programmes; such as sensors, detectors, robotics and optics. This project so far has already secured 300K in funding from I12 due to the success of the application so far with some thanks to the results produced as part of this project. If successful there is a future potential for this project to be used in medical imaging, security and industrial inspection.

I12 is a high energy (up to 150keV) beamline providing flexibility in the type and complexity of the experiments it can accommodate. The beamline is currently under construction, and when complete will consist of two Experimental Hutches. EH1 will provide a very high intensity beam for diffraction and imaging experiments while EH2 will provide a space where large-scale engineering and processing experiments can be performed. The new beamline will allow ground breaking experiments that simulate the service conditions experienced by real engineering components while their internal stress state and structures are continually monitored by an X-ray beam. The high energy x-rays that

will be used on I12 mean that materials with high stopping power are an essential requirement for any potential detector [2].

The experiments carried out in this project aim to develop the Science and Technology Facilities Council (STFC)'s scintillator detector program for X-ray measurements resulting in the production of a detector suitable for the I12 beamline. Specifically work will focus on the development of an active-pixel sensor known as the Large Area Sensor (LAS) in place of the more traditional photo-multiplier tube. Concepts of attenuation (stopping power), spatial resolution, modulation transfer function and count rate have all been considered as part of this research project.

The aim is to study, and be able to measure, the performance of monolithic active-pixel sensors (MAPS) at visible wavelengths and also the X-ray performance of MAPS when coupled to scintillators; otherwise known as an Active Pixel flat panel imager (APFPI). Structured scintillators and how their columnar nature affects efficiency and spatial resolution when used with MAPS will also be studied. As part of this project a literature review of scintillator research was completed and is summarised in this dissertation. It includes some of the key factors that affect detector and scintillator performance; rise and decay times, quenching (of which there are different forms such as self, impurity, thermal and energy quenching), density, stability, optical properties and temperature dependence. The key output of this investigation, as indicated in this dissertation thesis, is to test and characterise a new scintillator based X-ray detector.

1.1 RAL and the Detector Division

The Rutherford Appleton Laboratory is one of the foremost laboratories of its kind, possessing a global reputation for excellence. From astrophysics and satellite design to particle physics, RAL is committed to supporting high-quality scientific and engineering research. The laboratory enables scientific application within schools, colleges, universities and industries on a global scale. With departments such as ISIS (not an abbreviation but rather a name), Diamond Light Source (Synchrotron research facility) and central laser facilities, not to mention research carried out for the Mauna Kea observatories, the Large Hadron Collider (LHC) at the Conseil Europen pour la Recherche Nuclaire (CERN) and frequent European Space Agency (ESA) and National Aeronautics and Space Administration (NASA) missions, RAL is at the international fore front of scientific research and engineering.

Some of the most unique and ground breaking work associated with RAL is carried out within the Detector Division, for example, the design of the readout application-specific integrated circuit (ASIC) for the ATLAS project on the LHC was recently completed by

the group. Professor Renato Turchetta and Mr. Paul Seller head up the two groups associated with detector design and characterisation, and scientific application respectively. Previous and existing projects within Mr. Seller's group include the HEXITEC (High Energy X-ray Imaging Technology) project, an investigation of Cadmium Zinc Telluride (CZT) detectors which are high Z, direct band gap semiconductors, and also the design of a large area pixel detector for the XFEL (X-ray Free Electron Laser) project in Hamburg. Applications of the detectors developed in the group range from the development of retinal implants to the production of star tracking systems.

1.2 X-ray Radiation

Visible light has been known since organisms developed eyes. The electromagnetic spectrum contains a potentially infinite range of wavelengths some of which are familiar such as that detected by mobile phones and radios and television. These are classed however as types of "invisible" radiation. The idea of this "invisible" radiation is relatively new though. In 1800 William Herschel discovered infrared radiation when he found infrared light to affect a thermometer more than sunlight. Another example was the discovery of ultraviolet by Johann Bitter who found that ultraviolet radiation affected silver chloride more than visible light [3].

Throughout the 19th Century Maxwell, Hertz and Crookes all contributed significant research and findings on "invisible" radiation. It wasn't until 1895 when Roentgen noticed a barium platinocyanide screen fluorescing in his laboratory that he discovered X-ray radiation. He had generated cathode rays in a Crookes tube that was positioned near to the barium material [4]; the tube consisted of a glass bulb with positive and negative electrodes inside it. With the air evacuated and a high voltage applied the tube developed a fluorescent glow. It was only after shielding the Crookes tube with black paper that he observed the barium platinocyanide screen continuing to glow [5]. Realising the new type of radiation could pass through paper, he experimented with other objects of which the most famous was his wife's hand.

The first use of x-rays were for industrial applications which was first demonstrated by Roentgen who produced a radiograph of a set of weights in a box. Within a very short space of time x-rays were also being used in the field of medicine with radiographs in Europe and the States. Other applications included; location of bullets in wounded soldiers, dentistry, imaging metal plates, X-ray generators by the General Electric Company and X-ray approval of fusion welded pressure vessels once high vacuum tubes had been invented by William Coolidge in 1913.

1.3 Scintillators

Scintillation materials and detectors form the basis for many radiation-detection devices. Conversion of different ionising radiations to visible light gave rise to a new type of physics and engineering called 'scintillation material science' and 'detection systems engineering'. The difference between the two is that the later is when a detection device is developed using one or another material rather than pure scintillation materials production [6].

The first application of the scintillation technique dates from the period of Roentgen's discovery of x-rays in 1895 and Rutherford's research on alpha particle scattering in 1909. Over the last hundred years or so detectors have experienced a constant evolution. The first real-time detector and the precursor to the modern scintillation crystal detectors was the phosphorescent screen which Roentgen first used to observe x-rays. In the early 1920's the Geiger counter or G-M counter was produced as a refinement from the original gas filled radiation detector invented by Ernest Rutherford. With an inability to provide information on the energy of the radiation it detects, the G-M counter was soon superseded by scintillation crystals (although G-M counters are still widely used) and semiconductor radiation detectors which produce a response that is proportional to the energy of the photon stopped in the crystal [7].

The most commonly used scintillation materials are Caesium Iodide (CsI) and Sodium Iodide (NaI); the first high-performance Thallium doped Sodium Iodide (NaI(Tl)) scintillator was first grown only 55 years ago. Over the last 50 years thousands of different scintillation materials have been studied each intended to be more efficient and beneficial than the previous. Only a handful of these materials have been practically applied and made commercially available as scintillation detectors. Some of the most widely used scintillators are shown below in figure 1.1. These represent some of the materials considered for this project. The advantages and disadvantages of these different materials will be discussed further in the theory section of this report.

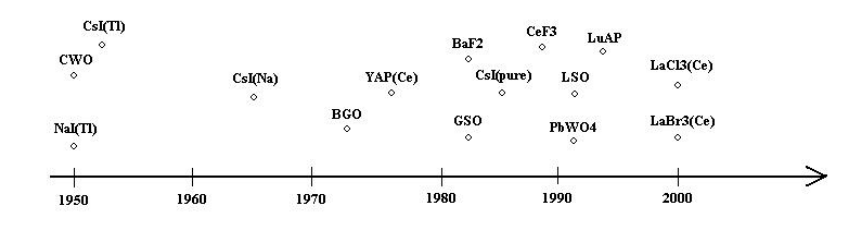


FIGURE 1.1: Commercially Available Scintillator History Line

1.4 Scintillation Detection

1.4.1 The Photomultiplier tube

At present the most common form of reading out light from a scintillator is to use a photomultiplier (PM) tube. Thus using a scintillator mounted onto a MAPS device is a rather innovative idea. Application of the PM tube range from optical spectroscopy to astronomy.

Vacuum conditions are maintained within a glass envelope so that low-energy electrons can be accelerated by the electric fields within the casing. One of the two main components of a PM tube is the photocathode which converts light photons into low-energy electrons called photoelectrons. The conversion will have a set efficiency assigned to it depending on the model of the PM tube. As only a few hundred photoelectrons will be present in one pulse, the second main part to the PM tube's structure is vital; the electron multiplier. This provides a good collection geometry and near ideal amplification of the photoelectrons to increase their numbers so that a convenient electrical signal can be detected. After amplification the detected pulse will contain 10⁸ strong electrons; this pulse is then collected at the output stage of the multiplier structure after the pulse has passed through a pre-amplifier, an amplifier and a pulse height analyser [8] [9]. The multiplication of electrons is due to a series of electrodes called dynodes. These electrodes are held at a large positive potential so electrons are accelerated towards them, and by doing so their energy increases. A common potential difference between each dynode is around 100V, therefore electrons strike the dynode with 100eV of energy. Dynodes make use of a phenomenon known as secondary electron emission. This is when a particle of sufficient energy hits a surface or passes straight through and induces the emission of more electrons, thus it may take 3eV to release an electron from the dynode surface and thus the gain factor of electrons will be around 30 [10]. A typical set-up of a photomultiplier tube is shown in figure 1.2 where the idea of electron multiplication is illustrated.

1.4.2 Monolithic Active Pixel Sensors (MAPS)

Monolithic Active Pixel Sensors (more commonly known as MAPS devices) are integrated circuits of active pixels formed in a single chip. An active pixel senor (APS) is an imaging sensor consisting of an integrated circuit containing an array of pixel sensors, each pixel containing a photodetector, an active amplifier and at least one transistor. Made in a Complementary Metal Oxide Semi-conductor (CMOS) technology, they are

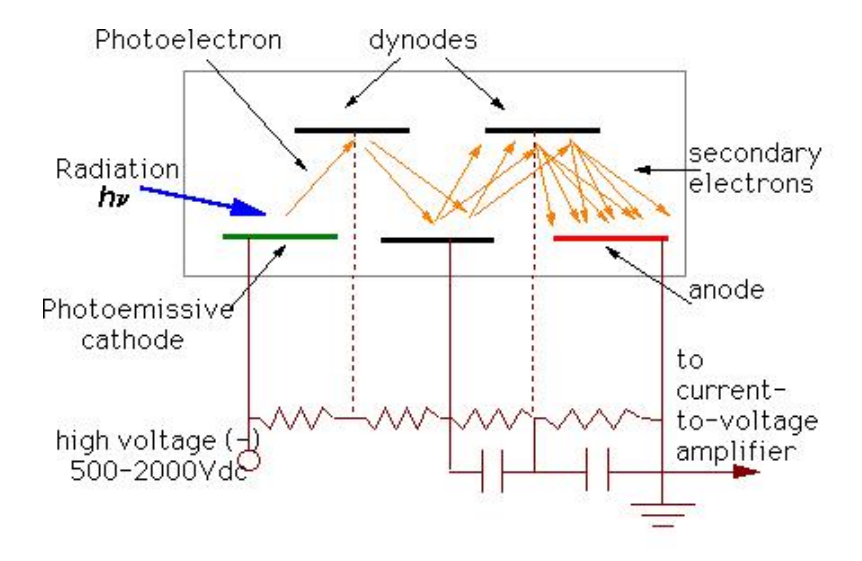


Figure 1.2: Photomultiplier operation and dynode illustration with emphasis on secondary electron emission

[11]

used as an alternative to Charged Coupled Devices (CCD) in visible light imaging applications [12].

The term active pixel sensor was named by Tsutomu Nakamura who worked on the Charge Modulation Device active pixel sensor at Olympus. It was further defined in a 1993 paper by Eric Fossum [13]. Noble, Chamberlain and Weimer et al all described image sensor elements with in-pixel amplifiers around the late 1960's when pixel sensors without their own amplifiers were being researched. However these suffered from many limitations, such as high noise, slow readout, and lack of scalability. Adding an amplifier to each pixel solved such problems and hence the active-pixel sensor was created [14]. The CCD was invented in 1970 at Bell Labs. Because the metal-oxide semiconductor (MOS) process was so variable and MOS transistors had characteristics that changed over time, the CCD's were more preferable and so quickly took over from the active pixel sensor. But by the late 1980s and early 1990s, the CMOS process was well established as well controlled and stable and provided the baseline process for the production of almost all logic and microprocessors [15]. Fossum then went further and invented the image sensor that used intra-pixel charge transfer along with an in-pixel amplifier to achieve true correlated double sampling (CDS), low temporal noise operation and on-chip circuits for fixed-pattern noise reduction. With this break-through APS imagers became the commercial successor of CCDs [13].

Between 1993 and 1995 prototype devices for a number of applications such as web cams, high speed and motion capture cameras, digital radiography, endoscopy cameras, and of course camera-phones were developed by the Jet Propulsion Laboratory using these new APS imagers. CCDs soon became the inferior with a higher temporal and fixed-pattern

noise. It is the CMOS MAPS devices which are currently use on a day-to-day basis.

1.5 Structure of the remaining Dissertation

The remainder of this dissertation thesis will discuss the procedure carried out on the relevant experimental testing of the scintillator materials and the CMOS APS. Work has been completed with computer programming software such as Laboratory Virtual Instrumentation Engineering Workbench (LabVIEW) and MATLAB (a numerical computing environment and fourth generation programming language). The need for additional products from the campus workshop was also required. The experimental set-up of the apparatus is discussed along with the results produced. The theory behind the physics involved and the scintillators required will also be an important part of the rest of this report. Finally, conclusion on the work carried out and the findings discussed will also be included, aiming with the result in taking a step further to producing a high energy X-ray imaging detector for I12 at the Diamond Light Source.

Chapter 2

Scientific Background and Theory

When investigating with different scintillation materials and considering the changing properties of the APFPI, is it essential to know the mechanisms and fundamentals both experimentally and theoretically behind the interactions and physics which will occur. This chapter discusses such necessities. First however the scientific background behind the application of the project will be discussed.

2.1 I12 Detector Background

The end product of this investigation is to produce a suitable detector system for the I12 beamline on the synchrotron at the Diamond Light Source. The position sensitive high energy X-ray diffraction detector was ideally asked to have the specifications listed in table 2.1.

While some of these specifications were easily achievable (energy range and pixel size for example) others such as the dynamic range and peak data rate are less feasible and would need a lot more funding than is available to drastically enhance the performance of the Large Area Sensor. As these parameters are as a whole quite ambitious, the author's line manager Matthew Wilson calculated some preliminary expected properties of the detector system with a 1.5mm thick CsI(Tl) scintillator with a fibre optic shield and coupling gel, using some basic results and theoretical knowledge. Table 2.2 outlines these.

Some of these results were obtainable by use of the scientific background and theory that follows.

Requirement	Ideal	Priority
Dynamic Range	Photon counting or 10^5	Н
Image latency	Below noise	Н
Energy range	$50\text{-}150\mathrm{keV}$	Н
Readout time	<30% max frame rate	Н
Framing rate	>1kHz	Н
Peak data rate	3Gbyte/s	Н
Pixel size	$100\mu\mathrm{m}^2$	M
Defective pixels	< 0.01%	M
No. of pixels	>1000 x 1000	M
Resolution	Pixel size	M
Dead area	<1%	M
Shape	Plane	M
Counting rate	$>2x10^6/pixel/s$	M
Average data rate	600Gbytes/day	M

Table 2.1: Ideal Detector Specifications for I12 [16] In the table H and M are regarded as High and Medium priority respectively.

Property	$50 \mathrm{keV}$	$150 \mathrm{keV}$
Spatial Resolution From a Single Image	$300 \mu \mathrm{m}$	$300 \mu \mathrm{m}$
Spatial Resolution From Averaged Images	$250 \mu \mathrm{m}$	$250 \mu \mathrm{m}$
Stopping Efficiency 1.5mm thick CsI	98.8%	30.6%
Dynamic Range in X-ray Photons (6x6 pixels)	20 to 12500	7 to 4166
Quantum Efficiency of Entire Detector	20%	6%
Full Frame Readout Speed	$40 \mathrm{Hz}$	40Hz
54x10mm Active Region Readout Speed	160Hz	160Hz
54x1.6mm Active Region Readout Speed	1kHZ	1kHZ

Table 2.2: Expected detector properties with a 1.5mm thick CsI(Tl) scintillator [17] Table obtained from Matthew Wilson *et al* internal report.

2.2 Characteristic X-rays

X-rays are classified as being high energy photons (ranging from hundreds of eV to hundreds of keV) and are produced in strictly controlled laboratory environments due to the damaging effects they have on soft tissue. A high Z target (an element with many protons) such as tungsten is bombarded by high velocity electrons producing Bremsstrahlung and characteristic x-rays; both are forms of X-ray radiation. Figure 2.1 illustrates the mechanism within the X-ray tube for the production of both types of x-rays.

Bremsstrahlung (or breaking radiation) is the emitted radiation from charged particles decelerating in a medium. The Bremsstrahlung energy spectrum is a continuum since there are no quantised energy transitions to dictate otherwise. Characteristic x-rays on the other hand, are the result of varying electron energy transitions. Due to some excitation processes and interaction with the electrons incident on the target the orbital

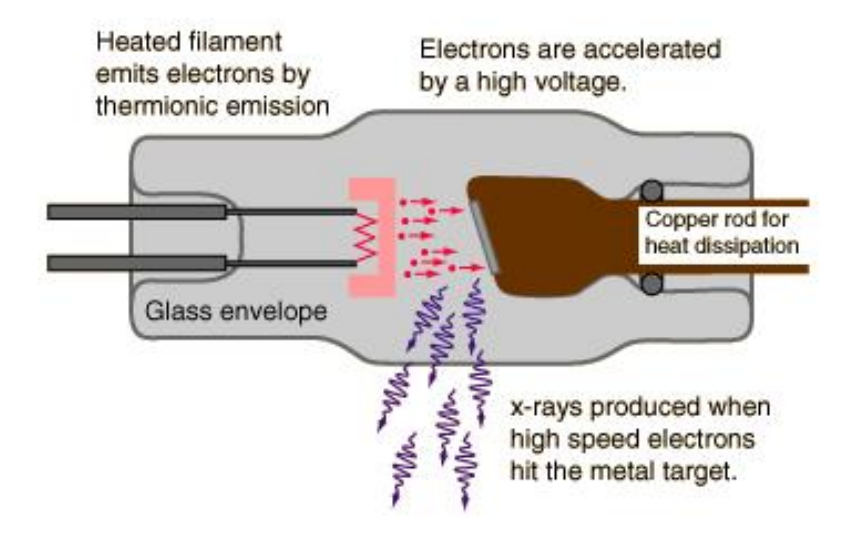


FIGURE 2.1: Production of X-ray radiation inside a typical X-ray tube [18]

electrons in an atom can be knocked from their shells leaving unstable states behind. The electrons naturally try to rearrange themselves so the atom can be returned to its ground state (or lowest energy). Atomic stability is regained by electrons moving from higher energy levels, however such electrons possess an energy much greater than needed to stay in their new orbits and so excess energy is emitted in the form of characteristic x-rays. Figure 2.2 explains this schematically.

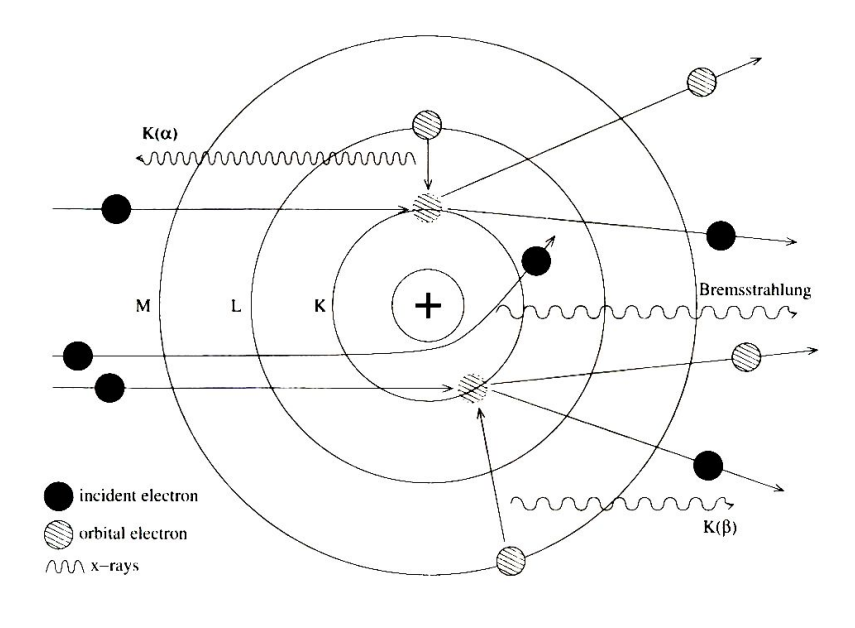


Figure 2.2: Generation of Bremsstrahlung and characteristic x-rays [19]

The energy of a characteristic X-ray photon is given by the energy difference between

the initial and final states of the transition therefore it does not depend on the intensity of the incident beam of electrons. If the vacancy was created in the K shell of the atom, a characteristic K X-ray is produced when said vacancy is filled by an electron from a higher level than the vacancy. Say that electron originates from the L shell, then a K_{alpha} photon is released. The energy of such a photon will be equal to the binding energy between K and L shells. Comparatively a K_{beta} photon arises from a M to K level transition [8] and so on. The spectra for Bremsstrahlung and characteristic x-rays are often plotted simultaneously characteristic X-ray emission lines superimposed on the continuous Bremsstrahlung data, as seen in figure 2.3.

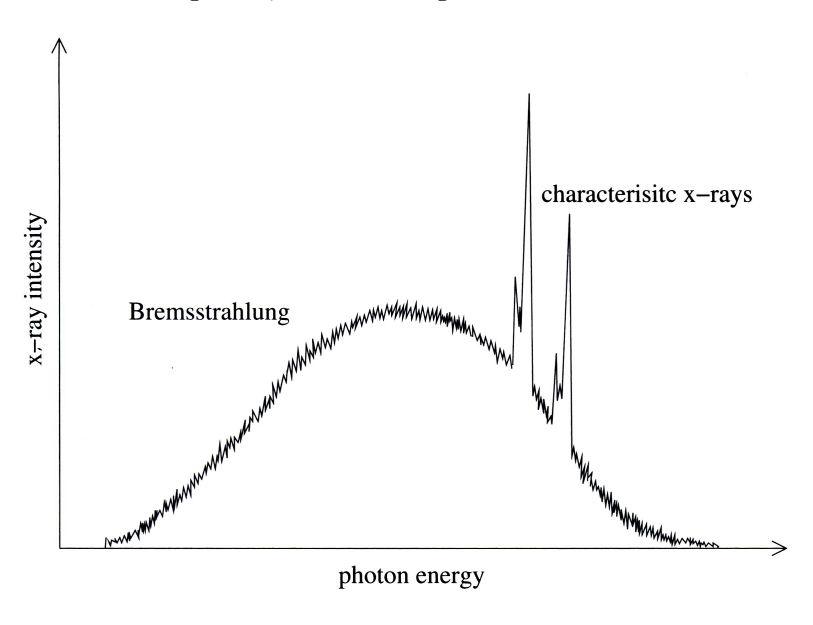


Figure 2.3: Characteristic x-rays peaks of K_{alpha} and K_{beta} on a Bremsstrahlung continuum

[19]

2.3 X-ray Interaction with Matter

To understand how the X-ray radiation produced in the tungsten filament affects our various scintillation materials the physics behind such interactions must be studied. The processes which occur in the material itself, and the effect this has on the produced light yield, will be discussed in sections to follow on Scintillation Material and Mechanism. The interaction mechanisms of x-rays and γ -rays are fundamentally different to those of charged particles i.e. α particles and protons. The two main processes for heavy charged particles are Rutherford Scattering and Coulomb scattering. Coulomb's law gives rise to both of these, consequently describing the force (F) exerted on one particle by another due to their differing charges. The experiments in this investigation though require the knowledge of the electromagnetic interactions only.

Interactions occur through three dominant processes; Compton Scattering, pair production and photoelectric absorption. These processes lead to the partial or complete transfer of X-ray energy to atomic electrons by means of entire absorption or scattering through a significant angle.

Figure 2.4 displays the contribution of each of these processes along with the total attenuation for CsI(Tl). As each process is described below the dependance on each with regards to X-ray energy should be referred back to the figure.

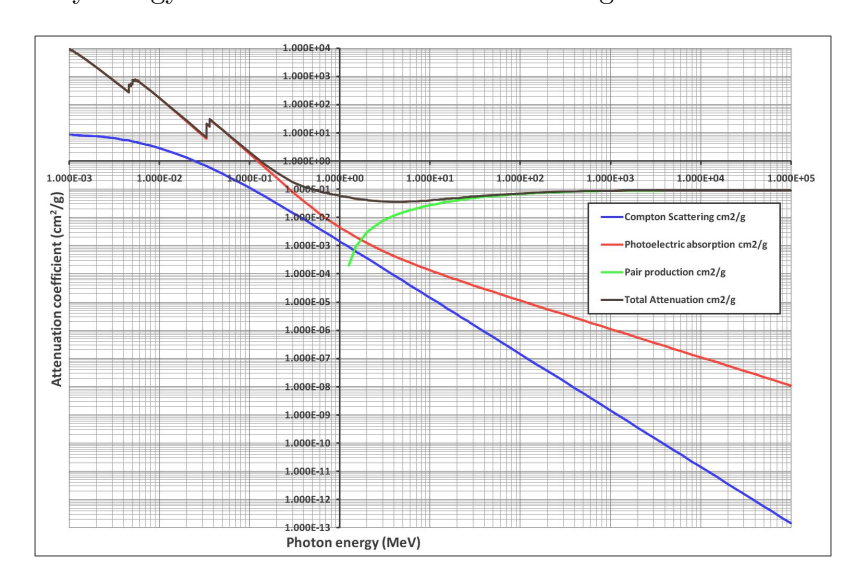


FIGURE 2.4: Three key processes of radiation interaction including the total attenuation through CsI(Tl) as a function of photon energy. The jumps in photoelectric absorption and therefore total attenuation at low photon energies are due to the binding energies of electrons in specific shells in the atoms

The values were estimated using a program named XCOM and are given in the energy range 1keV to 100GeV. XCOM was published in June 2005 by the National Institute of Standards and Technology (NIST) Physics Laboratory. The authors are N. J. Berger; J. H. Hubbell and S. M. Seltzer [20].

2.3.1 Photoelectric Absorption

Possessing the greatest range of energies at which this interaction occurs, photoelectric absorption is often the dominant process of the three discussed. Similar to the Compton effect, an incident photon collides with a target atom. On doing so the entire photon's energy is transferred to an inner orbital electron (bound in its atomic state). Ionisation occurs at sufficient energies (greater than a few hundred keV), meaning that the electron has received enough energy to break free from its bound state and is ejected from the

atom. This is a photoelectron of energy E_e .

$$E_e = h\nu - E_b \tag{2.1}$$

where E_b is the binding energy of the electron in its shell, before it interacts with the incident photon and subsequently becomes a photoelectron. h is plank's constant and ν is the frequency of the radiation.

The atom is now in an excited state and is also ionised. The vacancy left behind by the photoelectron is rapidly filled by another electron from an adjacent atom or a higher shell electron dropping into the hole. In doing so a characteristic X-ray is created, however due to photoelectric absorption many of these x-rays are reabsorbed by outer shell orbital electrons.

The probability of an interaction to occur (τ) is given by:

$$\tau \cong C \cdot \frac{Z^n}{E_{\gamma}^{3.5}} \tag{2.2}$$

where C is an arbitrary constant, Z is the atomic number of the absorber material, n is an exponent whose value varies between 4 and 5, and $E\gamma$ is the γ - or X-ray energy. As can be concluded from the equation the process is enhanced for higher Z materials, hence a key variable for X-ray detection and shielding.

2.3.2 Compton Scattering

Named after the physicist Arthur Holly Compton, the Compton effect was observed in 1923 and won him the Noble Prize in Physics in 1927. Compton scattering is an interaction involving the inelastic scattering of an incident X-ray or γ -ray photon from outer level electrons which are loosely bound (binding energies are a few hundred eV while x-or γ -ray energies are a few hundred keV) to the material by the electromagnetic force. These electrons are considered to be at rest due to the difference in their binding energy with the incident photon energy and so posses a rest-mass energy of $m_o c^2$ (511keV) [8]. On interaction with the atom the incident photon is scattered by an angle θ due to the energy dissipated from the photon to the electron, which is no longer at rest and becomes a recoil electron projected through an angle ϕ from its original location. The energy transferred to the electron is dependant upon the incident photon energy and the scattering angle of the photon which ranges as equation 2.3 models. The sketch of figure 2.5 illustrates this theory and aids in the understanding of equation 2.3.

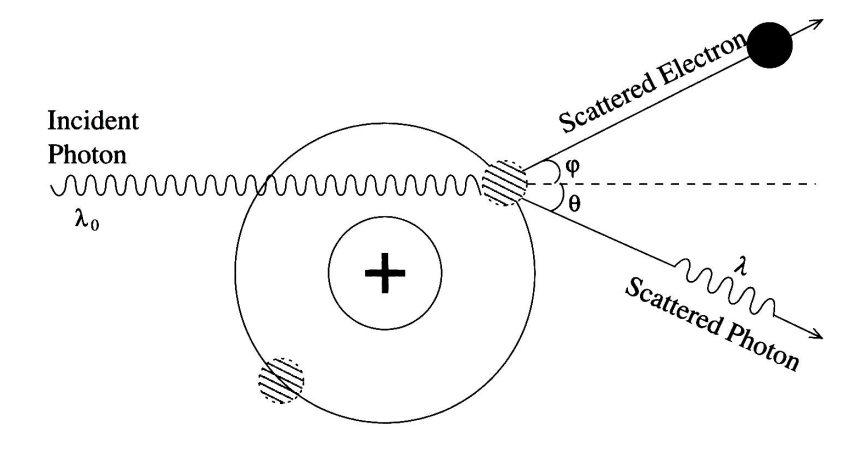


FIGURE 2.5: Compton scattering of a photon whose frequency $\nu = c/\lambda_o$, where c is the speed of an electromagnetic wave in free space [19]

$$h\nu t = \frac{h\nu}{1 + \frac{h\nu}{m_0 c^2} \cdot (1 - \cos\theta)}$$
 (2.3)

The interaction and equation holds true to the conservation of energy and momentum, hence the ability to obtain $h\nu$ (the energy) of the scattered photon.

The abundance of orbital electrons is the key variable in the probability of Compton scattering per atom of the absorber. The interaction will therefore increase linearly with atomic number Z. The dependance on X-ray energy can be seen in the previous figure 2.4. This decreases gradually with increased incident energy. The experiments shall be concerned with Thallium activated Caesium Iodide; the attenuation coefficients plotted will be negligibly affected by the addition of this dopant as the amount of dopant is relatively small.

2.3.3 Pair Production

Pair production is the dominant interaction at high energies of x- or γ -rays; the process results in the conversion of a photon into an electron-positron pair (hence the name given to the interaction). The energy of the incident photon must exceed 1.02MeV (twice the rest mass of an electron) for the interaction to occur. As photons have no rest mass themselves but positrons and electrons do, this is a process which converts energy into mass, given by Einstein's famous $E=mc^2$ equation. As the interaction takes place in the coulomb field of the nucleus (in order to conserve momentum), all of the incident photon energy above 1.02MeV is converted into kinetic energy equally shared by the electron and positron (as conservation of energy permits). Once the medium slows the positron

down it will annihilate producing two 511keV back-to-back photons.

The probability of pair production per nucleus is not well defined, however equation 2.4 is a good estimate for the magnitude of the interaction, hence the interaction will be more probable in high-Z materials.

$$PP_{magnitude} \simeq C \cdot Z_{absorber}^2$$
 (2.4)

C is an arbitrary constant and Z is the atomic number.

2.4 Scintillation Material

A scintillation material is one which exhibits the property of luminescence when excited by radiation; it is the detection of this scintillation light that forms the detector signal. Scintillators can be used to detect both charged particles and γ - and x-rays by coupling to a Photomultiplier tube (or other sensor) with a medium of refractive index roughly 1.5 (that of glass) being used. Other key properties should include:

- Proportionality of light yield to deposited energy over a wide range.
- Good light collection; the material should be transparent to the wavelength of its own emission.
- A fast signal pulse, so decay time of induced luminescence should be short.
- A refractive index similar to that of glass, allowing efficient coupling of the scintillation light to the photosensor.
- A good optical quality of the material and should be readily available in sizes convenient for a practical detector [8].

No scintillation material as yet has been found to successfully meet all key properties; hence a compromise of those listed above is used. The reasoning behind the fact that the refractive index of the medium should be roughly that of glass is because scintillators produce light in the visible region of the spectrum, thus photons must pass through the

material without significant attenuation. If this occurs information can be lost causing non-linearities in detector response.

Scintillators can be grouped as those that are organic or inorganic. Organic scintillators are generally faster but yield less light, whereas inorganics often have the best light output and linearity. As shall be seen later the intended detector application has a major influence on the scintillator choice. Inorganic crystals typically consist of high-Z components meaning they have a high density, favouring detection of gamma-rays. On the contrary, organics are used in beta spectroscopy and fast neutron detection measurements due to high levels of hydrogen. Hydrogen abundance is important as it has a relatively high interaction cross section (2.5 barns(b) for 2.5MeV neutrons). This is an indication of the relative probability for an interaction to occur [10], thus contributing to the high efficiency of the scintillator. When multiplied by the number of nuclei N per unit volume, the cross section σ is converted into the macroscopic cross section Σ . Each nuclei possesses an elastic scattering cross section $\Sigma_{elasticscat}$, a radiative capture cross section $\Sigma_{radiativecap}$, etc etc. and therefore the resulting Σ_{total} becomes the probability per unit path length that any type of reaction will occur [8]. Defined by equations 2.5 and 2.6

$$\Sigma = N \cdot \sigma \tag{2.5}$$

$$\Sigma_{total} = \Sigma_{elasticscat} + \Sigma_{radiative cap} + etc...etc...$$
 (2.6)

The actual reaction cross section σ relies on three parameters: the rate of the produced particle from the reaction R_b , the incident current of particles per unit time I_a , and the amount of target nuclei per unit area N.

$$\sigma = \frac{R_b}{I_a \cdot N} \tag{2.7}$$

With a high cross section (2.5 b) it is likely that there are many interactions within the scintillation material making it more efficient.

It is the Σ_{total} that has the same significance as the linear attenuation coefficient for γ and x-rays. The total attenuation coefficient as a function of energy can be compared
between inorganic and organic scintillator material. Figure 2.6 shows the differing attenuation coefficients as obtained by XCOM once again. In the energy range concerned
with in this investigation (roughly 1 - 100 keV), the graph shows that inorganics are
much better for our purpose due to increased attenuation.

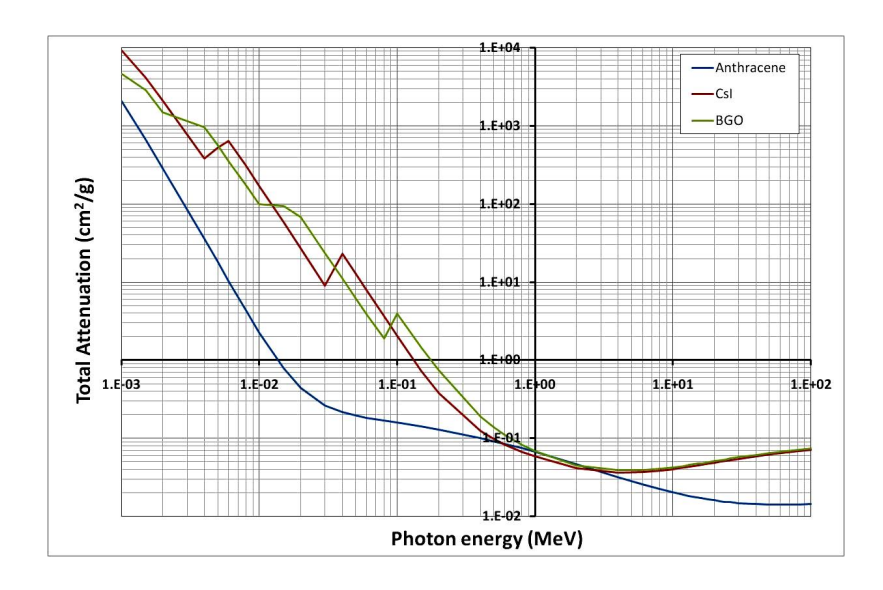


Figure 2.6: Total attenuation coefficients for three different scintillator materials. The graph clearly displays a higher stopping power (greater attenuation length) for inorganic materials

2.4.1 Fluorescence and Phosphorescence: Luminescence

The propagation of light is regarded as a wave phenomenon and upon striking matter it can either pass through with no absorption occurring or it can be either entirely or partially absorbed. In the case of absorption energy is transferred to the atom, which must occur in integral units; quanta. An atom can go from a lower to a higher energy level (of which there are a series of, that are closely spaced) by absorption of a discrete quantum of light, this will be equal to the energy difference between the states it is moving from and to. When an atom is raised to this higher excited state the de-excitation results in luminescence [21].

Luminescence is the emission of light from any substance occurring from electronically excited states [22]. Luminescence is divided into two categories; fluorescence and phosphorescence. Both of which are exhibited in figure 2.7. Which one occurs depends on the nature of the excited state. Fluorescence is the emission of visible light from singlet states by a substance that has absorbed light of a differing, usually invisible, light. A singlet state is where the electron in the orbital is paired by opposite spin to the second electron in the ground state. Conversely phosphorescence is emission from triplet excited states, where by the excited orbital electron has the same spin as the ground state electron. Due to these spin parities a fluorophore (a fluorescence photon) lifetime is roughly one nanosecond (time between its excitation and return to the ground state) whereas a phosphorescence lifetime is typically one second because transitions directly to the ground state are forbidden. This gives rise to a longer lifetime as the excited state must decay to another state via a non-luminescing process. This is the principle

behind 'glow-in-the-dark' objects following a phosphorescence substances exposure to light. Perhaps a more simple way to define between these two categories is to consider basic wave mechanics. A longer wavelength light is produced by phosphorescence hence possessing a slower characteristic time than that of fluorescence light. There is also delayed fluorescence which is the result of the same emission as prompt fluorescence however again, this has a much longer emission time following excitation [8] due to trapping of the electron in the forbidden gap, as explained in the following section.

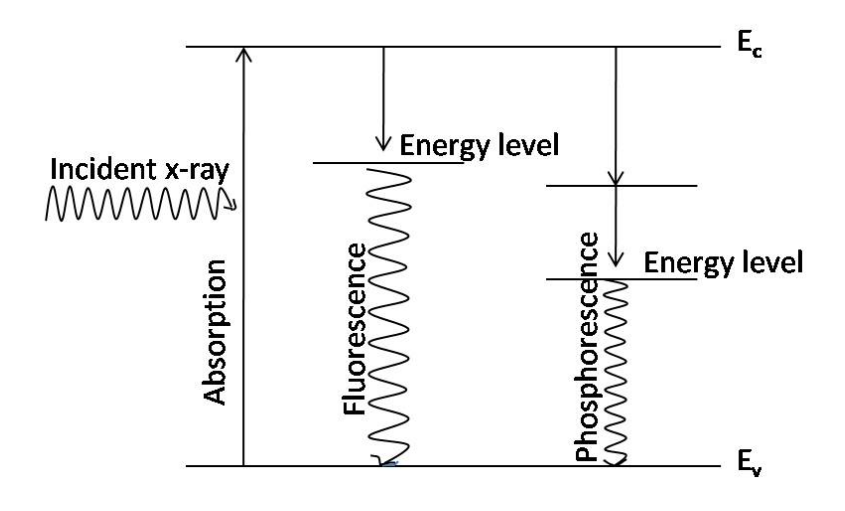


FIGURE 2.7: The concepts of absorption, fluorescence and phosphorescence are shown with respect to varied energy levels. It should be noted that the wavelengths of phosphorescence are not shorter than fluorescence as possibly misconceived from the diagram

2.5 Scintillation Mechanism

The mechanism theory differs between organic and inorganic scintillators. For the purpose of this dissertation only the mechanism relevant to inorganic scintillators shall be considered, as all materials researched were of inorganic nature.

Scintillators are like insulators, they have a wide gap between valence and conduction bands. In this gap, luminescence points/centres are found. As seen in figure 2.8. These are key in producing scintillation light. Luminescence centres comprise of two energy levels, where the difference is equal to the energy of the photons in the visible region of the electromagnetic spectrum. So a scintillation photon is emitted when an electron moves from the higher of these two states (levels) to the lower. This may not always be the case however, as energy may be dissipated by phonons (heat carrying particles) due to non-radiation transfer. This phenomenon is known as quenching [19] and is a random event, i.e. there is nothing to characterise whether a photon or phonon will be

dissipated.

In the case of crystalline scintillators, once the electron is in the conduction band, it may pass into a metastable energy state formed from impurities and defects. This state is called an electron trap. Periods in this state range from hours to nanoseconds, but eventually due to thermal agitation caused by continual vibration within the lattice, the electron will jump back into the conduction band. As these are 'delayed electrons', a build up of delayed photons with a long emission lifetime shall be seen.

The following figure, figure 2.8, schematically details how a general inorganic scintillation mechanism works. This would be for a typical material which has been "activated". In many materials intrinsic defects do not provide an efficient scintillation mechanism; for those materials to perform efficiently they must be "activated". A discussion of activation will follow.

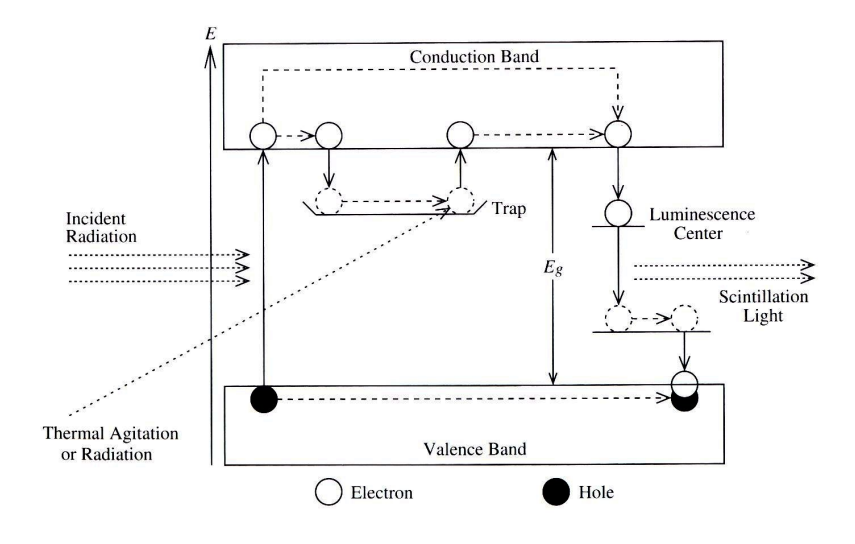


FIGURE 2.8: Principle of scintillation light production and scintillation mechanism [19]

2.5.1 Activators

Activators (also known as dopants) enhance the probability of visible photon dissipation as a result of de-excitation in the luminescence centres. They are deliberately added impurities; commonly used activators are Thallium(Tl), Sodium(Na), Cerium(Ce) and Europium(Eu) in materials that shortly follow and these are a few examples of many. Scintillators which have been activated may have the following abbreviated names: CsI(Tl) (Thallium activated Caesium Iodide), CsI(Na), YAP(Ce) (Cerium activated Yttrium

Aluminum Perovskite), and CaF(Eu) (Europium activated Calcium Fluoride). The addition of activator impurities create special states in the forbidden gap of the band structure of the material (between the valence and conduction bands). Through careful selection of the activator element it is possible to produce scintillation at visible wavelengths. Figure 2.9 illustrates the presence of such additional sites. It does not show the mechanism of the scintillator as in figure 2.8; simply a visual aid to where the Activator excited states are located.

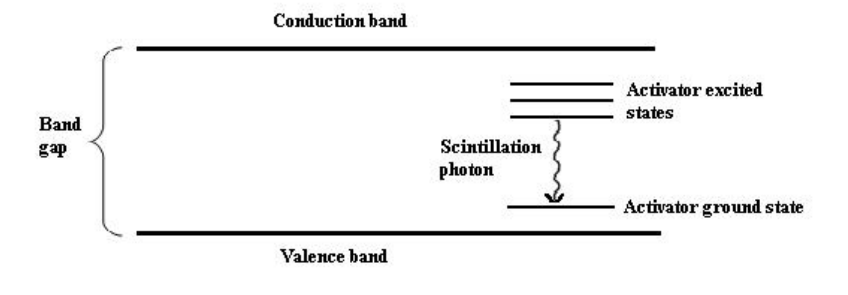


Figure 2.9: Presence of Activator excited states appear at a lower energy than the conduction band

[8]

As the energy required to reach one of these Activator excited states is less than that of the full forbidden gap, more photons are dissipated making the scintillator more efficient. More importantly (due to ease of detection) these photons are of visible wavelengths. Figure 2.10 graphically displays how the addition of an Activator to the material alters the wavelength of the emission photon, which importantly is not re-absorbed by the scintillator.

2.5.2 Radiation Interaction

As this investigation only requires the need for X-ray interaction, the focus shall be on how electromagnetic radiation affects the scintillation mechanism. Later on in this chapter the general theory of different types of interaction is discussed.

While traversing the material radiation energy is transferred to the particles of the scintillation medium via the process described in section 2.3, causing electrons in the valence band to be promoted to the conduction band, provided the radiation energy is greater than the band gap as seen in figure 2.8. A high energy X-ray will lead to the creation of a large number of electron-hole pairs; the electron is raised to the conduction band leaving a positive charge (to allow charge conservation), also known as a hole, in the valence band [19]. The electron in the conduction band de-excites through the emission

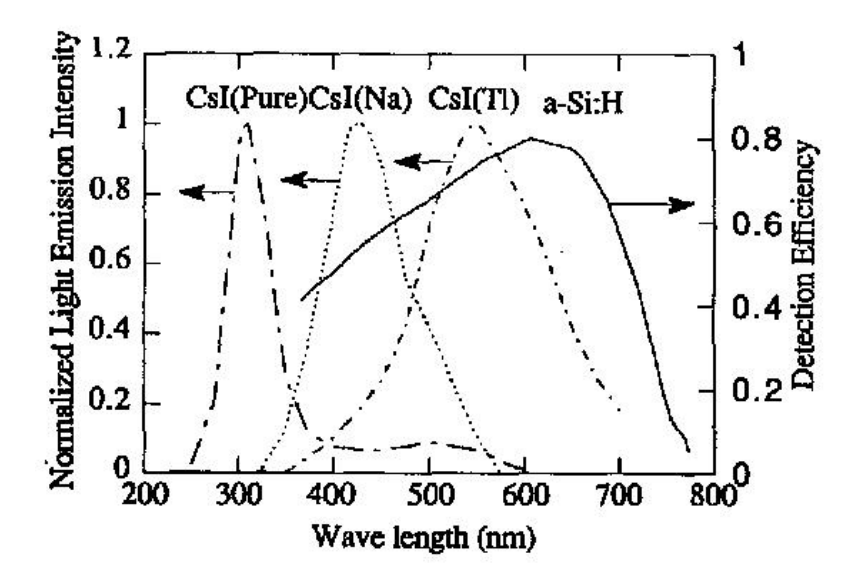


Figure 2.10: The addition of an Activator to a material commonly enables the emission photon to be within the visible range of the spectrum. Certain Activators aid in this principle better than others

[23]

of a thermal phonon to the lower energy excited activation site. This then de-excites through the emission of a photon to the activator ground state. Finally the electron and the hole in the valence band recombine. The emitted photon is often in the visible energy range with excited state half-lives of a few hundred nanoseconds. These decays determine the time characteristics of the emitted scintillation light [19].

Forbidden transitions may exist in the band gaps that do not result in the production of a visible photon; further energy is required to remove electrons from these trapped states. Previously mentioned as electron traps. The position of the trap in the forbidden gap will effect the energy required E to empty the trap. The probability P of emptying the trap is given by the Boltzmann distribution of

$$P \propto exp\left(-\frac{E}{k_B T}\right) \tag{2.8}$$

where T is the temperature of the lattice and k_B is the Boltzmann constant. The equation demonstrates that a larger energy value required, will correspond to a smaller probability of events occurring, therefore less chance of de-excitation from the allowed transition state meaning less photon production. This assumes however that the temperature (T) remains constant. As temperature (commonly from thermal agitation) is clearly a variable in the expression, a rise in temperature will allow de-excitation and so fluorescence and phosphorescence to occur with a higher probability than if temperature were not an influence.

An *exciton* is an alternative means of migration and is the name give to electron and a hole paired together that is free to drift throughout the lattice until reaching the site of an activator atom. Similar excitations can then occur as described above, giving rise to scintillation light once more by de-excitation to the ground state.

2.5.3 Emission and Absorption

In activated scintillators there is little self-absorption due to transparency to the scintillation light. In a pure crystal the energy required to form an electron-hole pair is similar to the recombination energy; this leads to heavy self-absorption. However, in an activated scintillator the emission wavelength is much less than the electron-hole pair energy [8]. An ideal photosensor for a particular type of scintillator will have a maximum quantum efficiency near the peak of the emission spectrum of that scintillator. Figure 2.11 illustrates this with the use of a PM tube and three common scintillation materials all of inorganic nature.

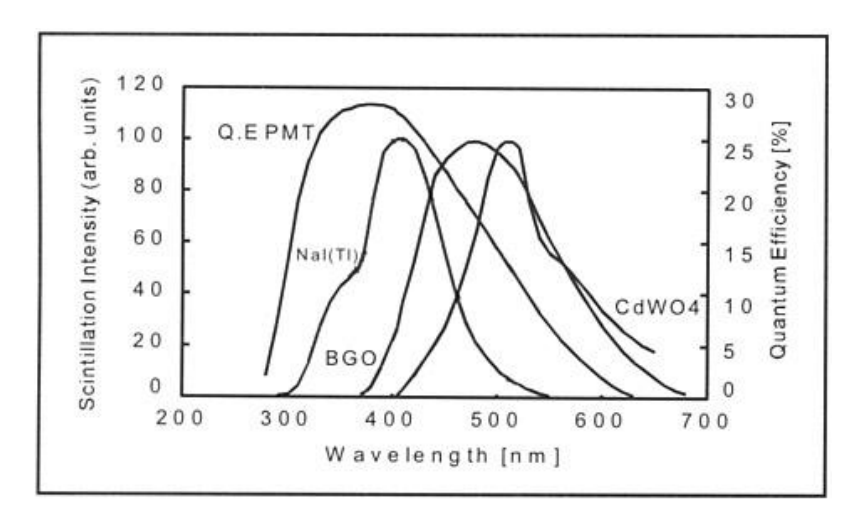


Figure 2.11: Emission spectra of NaI(Tl), Bismuth Germanate and Cadmium Tungstate compared to the quantum efficiency of a PM tube [24]

The quantum efficiency of the Large Area Sensor is an important parameter which will help us to use the scintillator with the best light output for this monolithic active-pixel device, as seen from figure 2.11. However, there are other more desirable factors such as spatial resolution and the stopping power of the material that will limit this. The quantum efficiency of an active-pixel sensor will be discussed later in this chapter.

Where the energy transition is less than required for the electron-hole pair production, the emission from an activated crystal will occur at an activator site. Resulting from this the spectrum is shifted to longer wavelengths where it is not affected by the absorption bands within the material. Luminescence bands are wide in inorganics due to broadening of the photon transitions by vibronic coupling. This is determined by a factor known as the Huang-Rhys factor; denoted S. As the emission band increases so too does the number of vibration quanta. The width of the emission band is therefore proportional to [25]

$$Bandwidth_{em} \propto \sqrt{S} \cdot \hbar \omega$$
 (2.9)

Note: the Huang-Rhys factor S is defined as the average number of vibrations emitted after optical transitions between excited and ground states. In the case of inorganic scintillators strong electron-phonon coupling exists (S>10) and emission band halfwidths are observed to be 0.2 to 0.5 eV [25]. S is obtained by a complex set of calculations and is dependant upon the number of photons captured in the light output, the capture rate, the mean number of phonons produced in transitions, angular frequency, the temperature of the lattice, and a dimensionless parameter determined by electron-phonon interaction. The equations need to be solved iteratively starting with S=0.

2.6 Other Inorganic Scintillator measurable parameters

2.6.1 Light Yield and Signal-to-Noise Ratio

An essential feature of any scintillator is the ability to be able to effectively convert ionising X-ray radiation to visible light. The light yield is a measure of how capable a scintillator is at doing this. The light yield can be quantified by the average energy loss per scintillation photon. The conversion or energy efficiency η is defined as;

$$\eta = \frac{\langle h\nu_r \rangle \cdot N_{ph}}{E_{\gamma}} \tag{2.10}$$

In equation 2.15, N_{ph} is the number of photons emitted due to the ionising radiation energy E_{γ} . $\langle h\nu_r \rangle$ is the average energy of emitted photons. The light yield being the number of emitted photons per unit of absorbed energy, relates to the energy efficiency by equation 2.11 [25].

$$L_R = \frac{N_{ph}}{E_{\gamma}} \cong \frac{\eta}{h\nu_m} \tag{2.11}$$

 L_R is the relative light output. This assumes that $\langle h\nu_r \rangle$ is roughly equal to the maximum of the emission spectrum $h\nu_m$.

Light yield is often measured in number of photons per MeV of absorbed radiation and is commonly dependent upon the type of scintillation material, the form of incident particles, the energy of these particles and lattice temperature. Temperature is important as the electron-hole pairs can be associated with semiconductor properties, therefore an increase in temperature will reduce the amount of light output detected. Considering the direct excitation of a luminescence centre, it is the probability of non-radiative transitions p_{nr} which affect the quantum efficiency q. p_{nr} is proportional to the Boltzmann factor. The probability of radiative transitions p_r is not affected by temperature. Thus giving;

$$q(T) = \frac{p_r}{p_r + p_{nr}} = \frac{1}{1 + Cexp\left(-\frac{E_q}{k_B T}\right)}$$

$$(2.12)$$

In equation 2.12 [25] E_q is the quenching energy and C is the quenching constant. When $k_B T \ll E_q$ the radiative transition dominates, hence a higher light output. Proving that an increase in temperature will reduce the amount of light output detected.

The light output is emitted in all directions due to the random angle and movement of the photon. Total internal reflection will be the most likely means of dissipation of the scintillation light through the medium, however micro-columnar structures of roughly 15μ m in the materials used allow for internal refraction. *i.e.* light passing between columns. This is not to be confused with the design of a structured scintillator. Columnar structures are fabricated to allow good spatial resolution. A comparison of the two is shown in figure 2.12.

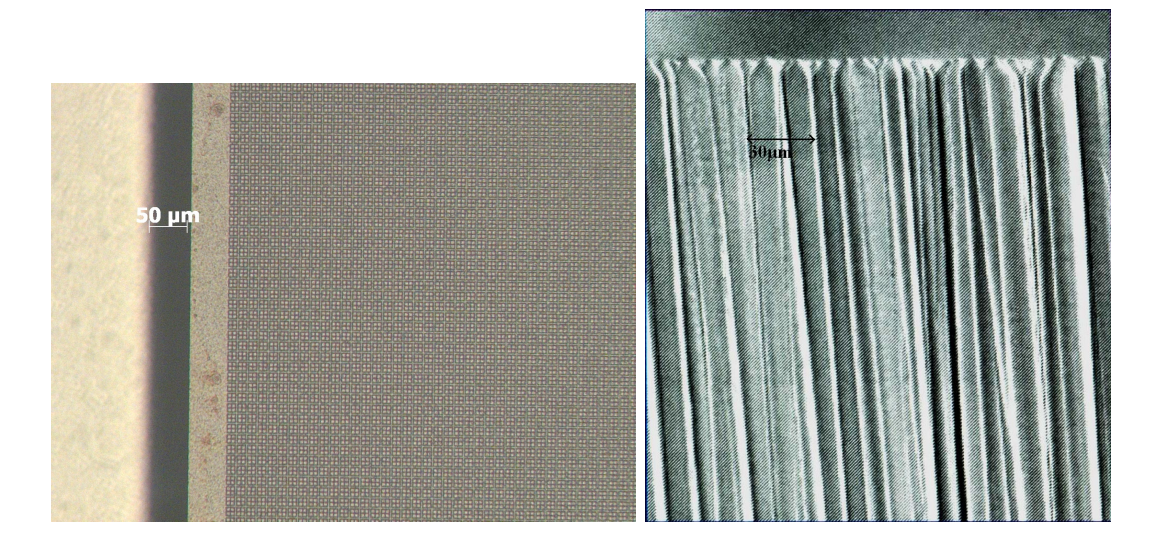


FIGURE 2.12: Structured and columnar scintillators from Hilger Crystals and Hamamatsu Photonics respectively

Attenuation will occur in columnar structures, inhibiting light yield. This may happen for several reasons such as: imperfections between interfaces; overlap of emission and absorption bands causing scintillation light to be reabsorbed; and Rayleigh scattering from density fluctuations (due to a region of higher or lower density with a slightly different refractive index than the surrounding medium) [26].

The light yield can also be measured as relative to another scintillator (this may be any other scintillator and there is not a standard reference used). If such a relation factor is found to be very low, the signal-to-noise ratio (SNR) of the photo-detector may not be acceptable. SNR is the power ratio between signal and background noise. By plotting SNR against the mean signal different noise regimes can be seen. It can be expressed using the following simple equation;

$$SNR = \left(\frac{A_{signal}}{A_{noise}}\right)^2 \tag{2.13}$$

Here, A is the root mean square amplitude.

2.6.2 Rise and Decay Times

As mentioned earlier scintillators can be closely compared to capacitors, therefore all scintillators have a characteristic rise and decay time. The time profile of a scintillation light pulse exhibits the form of a Boltzmann distribution where by the time after which the intensity of the light pulse has returned to 1/e of its maximum value, given by the Boltzmann factor. The pulse rises quickly with a rise time of about a nanosecond and then tails off with decay at a slower rate, usually of the order of a few hundred nanoseconds (however some scintillators possess extremely long decay times in the order of milliseconds; Gadolinium Oxide for example). In high rate situations, this slow decay time causes an overall efficiency drop in the scintillators performance. Each decay profile is unique to each scintillator. The rise and decay times for CsI(Tl) are roughly 20ns [25] and 4000ns [25] respectively. The latter being a summation of two decays. A typical pulse shape for CsI(Tl) is illustrated in figure 2.13.

The energy of an incoming X-ray or γ -ray photon is what causes varying decay times of pulses. Those photons or more generally particles with a higher dE/dx (change in energy as a function of distance travelled; stopping power or attenuation) will fill more long lived states due to the depletion of more energy, hence a longer time exists before de-excitation to the ground state occurs. This leads to significant emission of delayed light, as more electrons have been trapped in the metastable states. The published decay time constant is always an average of many decay constants, due to the availability of many metastable states. Temperature dependence will also vary the decay constant;

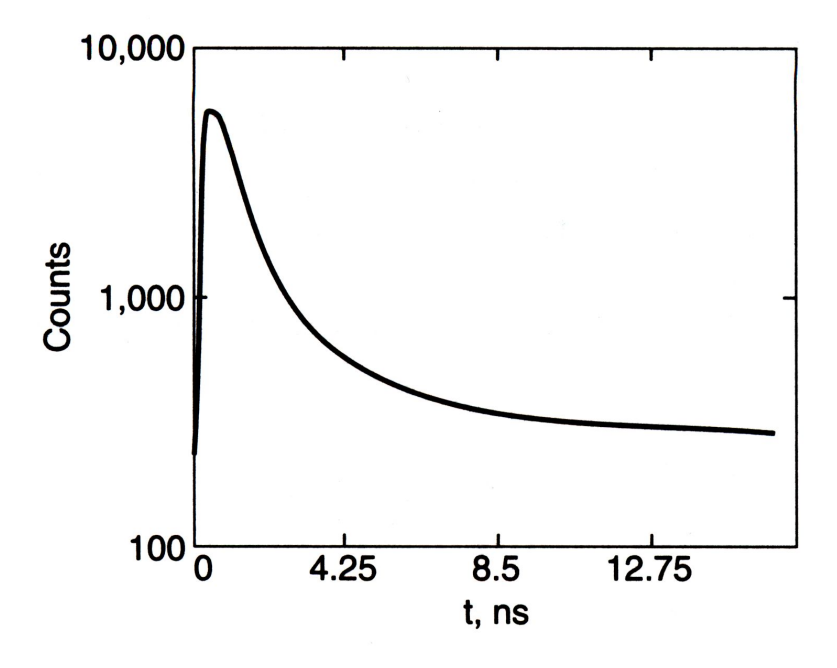


FIGURE 2.13: Room temperature pulse shape for Thallium activated Caesium Iodide [25]

reducing it if there is a rise in temperature. Reducing the decay constant means making the time quicker, hence the faster time constant. because of this, scintillators are aimed to operate at low temperatures due to the amount of thermal energy the particles possess in the material.

2.6.3 Efficiency

Inorganic scintillation materials consist of high atomic number elements; these have high X-ray absorption properties. Efficiencies are defined as a ratio of one property to another:

$$\eta = \frac{E_s}{E_i} \tag{2.14}$$

Efficiency is denoted by the Greek symbol η . E_s is the total energy of scintillation photons and E_i is the energy deposited by the incident radiation.

Due to the many parameters an inorganic scintillator may posses, there are a number of different efficiencies associated with each material. Scintillation efficiency is the collective of these as described by equation 2.14. The average amount of photons produced by every electron-hole pair depends on the transfer efficiency and the light collection efficiency of the luminescence process in each scintillator. The energy efficiency is the combined efficiency of these two:

$$\eta_{energy} = \frac{\alpha}{\beta} \cdot \frac{h\nu_m}{E_q} \tag{2.15}$$

Where α and β are the average number of photons produced and the numerical coefficient of the scintillator respectively. For ionic crystals β ranges between 1.5 and 2.0. The energy of the maximum of the emission spectrum $h\nu_m$ and the band gap width of the crystal E_q will depict whether or not a material has a high scintillation efficiency.

- Transfer efficiency is dependent upon a few factors, these include:
 - uniformity of transmission of the scintillator,
 - ability of the reflector covering to reflect light,
 - uniformity of the photocathode,
 - variance in quantum efficiency of photosensor,
 - uniformity of optical coupling to the photosensor surface [25].

The transfer efficiency will rely less on these factors through the application of better materials and good geometry of the detector. The total number of photons emitted from the luminescence centres in the material can be given as;

$$N_{ph} = T \cdot q \cdot N_{eh}, \tag{2.16}$$

where N_{ph} and N_{eh} are the mean numbers of emitted photons and electron hole pairs respectively. q is the quantum efficiency of the luminescence centres and is often close to unity for many activators in the absence of quenching. T is the transfer efficiency. In the luminescence centres this corresponds to the migration losses of energy, which is often the main source of energy loss resulting in a low scintillation yield.

Kalashnikov et al measured the scintillation efficiency of CsI(Tl) for excitation with 1.5 - 2.5 eV x-rays from a laser plasma. Figure 2.14 summarises their results in graphical form.

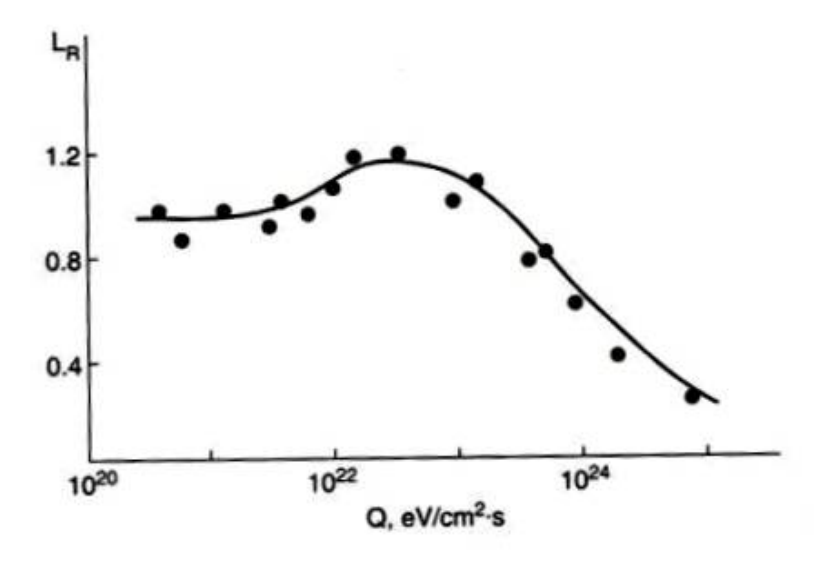


Figure 2.14: Relative scintillation yield against density of flux of x-rays. An increase of yield L_R is present due to an increase of scintillation rise time. This is the range of the maximum efficiency

[27]

2.7 LAS: A CMOS Image Sensor

This report will not cover the finer details regarding CMOS technology and the theoretical functioning of LAS. This is because such theory and scientific understanding was not needed to complete the investigation which was set.

The terminology of active-pixel sensors, charged coupled devices and CMOS technology was previously described in the Introduction chapter to this report. The remaining sections of this Scientific Background and Theory chapter will briefly explain the fundamentals of the Large Area Sensor and the equations that shall be focused upon in the results of this investigation so far.

2.7.1 The Active Pixel Sensor

CMOS pixels are divided into two groups, active-pixel senors and passive pixel sensors, however it is only active-pixel sensors which this report is concerned with. Monolithic active-pixel sensors (MAPS) are integrated circuits of active pixels formed in a single chip. A common CMOS active-pixel sensor contains a n-well/p-substrate type photodiode and three transistors ('3-T') per pixel. CMOS MAPS are known as charged particle or photon tracking devices. Active pixels in the sensor usually have a fill factor (the ratio of detectable area on each pixel) of around 60%, reducing the photon-generation signal. As there is therefore a reduced capacitance, a lower read noise is apparent for

the array, increasing the dynamic range (largest possible signal divided by the smallest possible signal it can generate, where the largest possible signal is directly proportional to the full well capacity of the pixel and the lowest signal is the noise level when the sensor is not exposed to any light: the noise floor) and signal-to-noise ratio of the sensor.

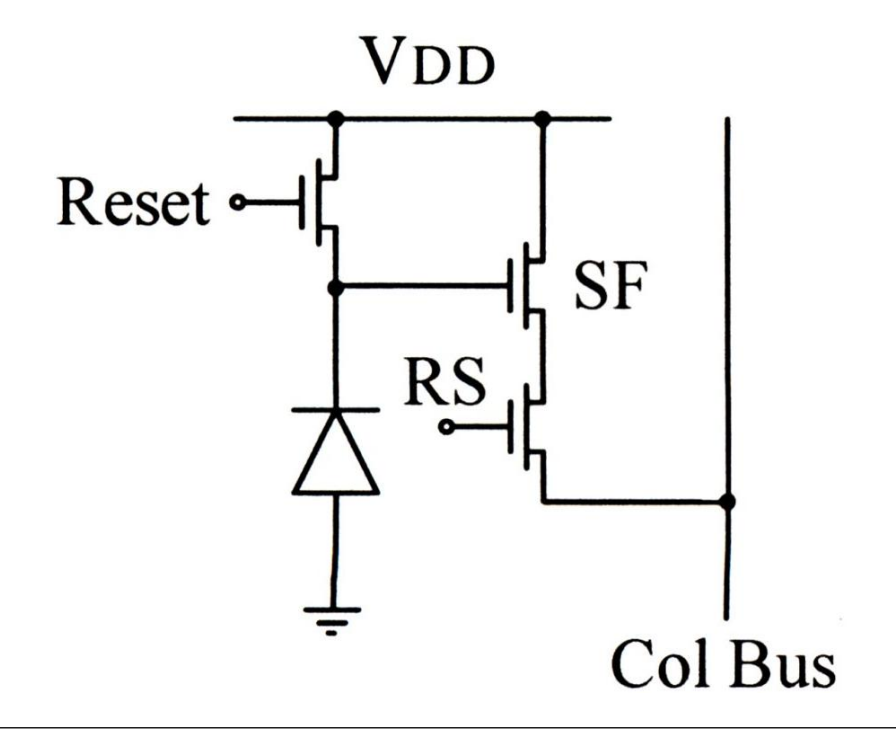


FIGURE 2.15: APS pixel schematic

Figure 2.15 [28] schematically details the pixel layout of an active-pixel sensor. Where V_{DD} is the drain voltage. The three transistors can be clearly seen as the reset, the row select (RS) and the source follower (SF). The reset transistor clears the pixel of integrated charge, the source follower transistor is the input of a simple amplifier and the row select transistor 'activates' the pixel for readout and presents its voltage to the column bus. Each pixel responds as an individual detector element, the operation of which can be separated into three phases: reset, integration and readout [29]. The column-bus connects all pixels in a vertical line; it is simply a thin strip of wiring. A row of pixels at any one time is transferred to each column, of which has an amplifier. The outputs of all the columns are then multiplexed together and sent to one or more output amplifiers. An analogue-to-digital converter then produces the measured digital output. For further explanation on pixel operation of reset and phototransduction stages, see "CMOS Imagers: From Phototransduction to Image Processing" [28].

The actual sensor itself is constructed from a thin substrate which allows production of vertex detectors with an extremely favourable material budget. A partially depleted thin epitaxial layer of a low-resistivity silicon wafer is often used as a sensitive detector volume from which the charge liberated by ionising particles is collected by diffusion [30]. Initially, all monolithic pixel sensors were made-up using a CMOS process. In this substrate type a 10μ m lightly p-doped silicon epitaxial layer is grown on a heavily p++ doped 500μ m supporting structure. On this n+ and p+ wells are formed giving rise to implantation of CMOS transistors. A cross section of the epitaxial type wafer is shown in figure 2.16 [31].

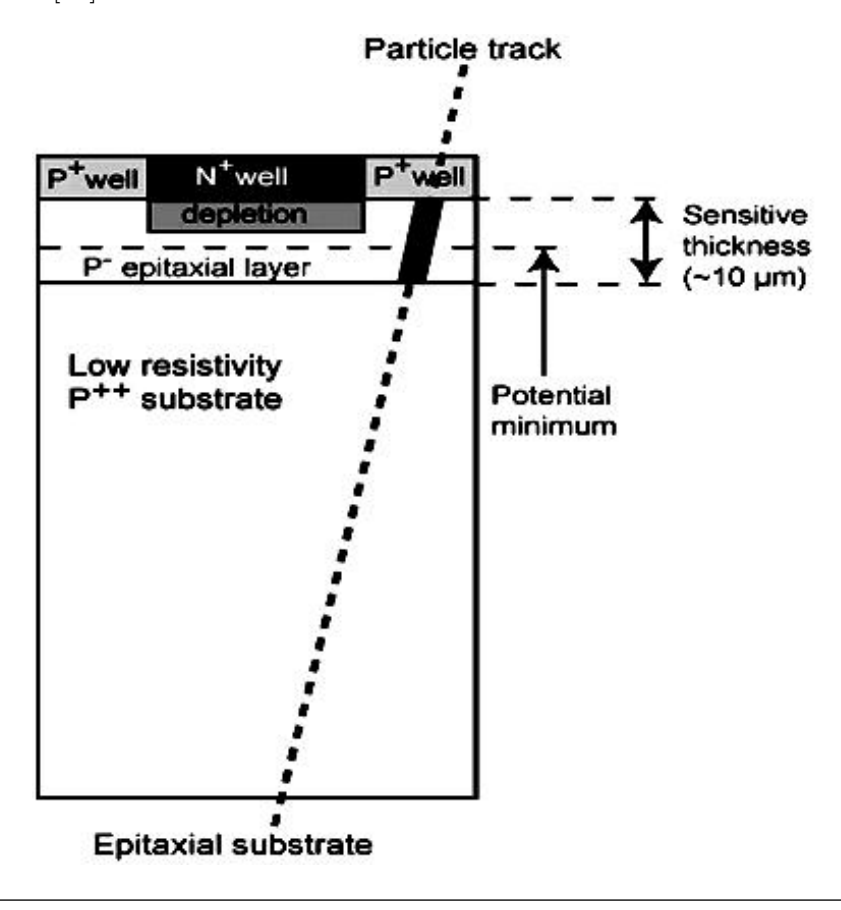


Figure 2.16: Cross section of the epitaxial type wafer used for the fabrication of CMOS MAPS

CMOS technology makes MAPSs use complementary and symmetrical pairs of p-type and n-type metal oxide semiconductor field effect transistors (MOSFETs) for logic functions. These then generate a voltage proportional to the charge in the pixel. The type of transistor (for example, N-MOS) is determined by the relevant doping of its source and gate. For instance, holes are pushed away and electrons gather at the surface of the substrate if a positive voltage is applied across the material. This creates a path of surface electrons between the source and drain of the N-MOS transistor [32]. Cut-off, Linear and Ohmic, and Saturation are the three modes of operation a transistor of this type can run in.

The important properties of an X-ray diffraction detector such as LAS include large area, low noise, high dynamic range, good linearity, fast readout, high frame rate and

high quantum efficiency. The active-pixel sensors investigated here was produced by the RC-UK M-I³ consortium (Multidimensional Integrated Intelligent Imaging) [29]. LAS was designed for X-ray diffraction measurements, attempting to combine low noise, high speed readout and wide dynamic range in a large area device.

2.7.2 LAS properties: Dynamic range, imaging area and regions of reset

LAS is a large area, 54mmx54mm, 1.8 Megapixel CMOS image sensor. It is structured by a 1350x1350 array of pixels on a 40 μ m pitch, each of which contains 9 transistors each with different integration times. A frame rate of up to 20 frames per second (fps) with full frame readout is accomplished using ten parallel outputs. LAS was originally designed for medical X-ray imaging research, although is a good device for X-ray diffraction studies. These applications require a large, effective sensing area and a high dynamic range.

As previously mentioned an ideal imager for X-ray diffraction studies would have a high dynamic range, ideally in excess of 120dB. Dynamic range is met by minimising the noise detected which is electronically accomplished by reducing the capacitances of the photodiode and other built in pixels. More importantly, this includes the ability to reset the pixel a number of times during the integration time. This is known as "multiple reset architecture" [33]; a development of "individual pixel reset architecture" enabling the creation of three different integration time regions across the array for dynamic range enhancement. This updated architecture benefits the sensor more than self-resetting pixels which require a more complex pixel design, thus reducing integration time and quantum efficiency of the system.

The large area parameter that LAS meets was overcome using stitching techniques in order to achieve a large desirable design. The boundary between stitched sections is seamless, resulting in no loss of pixel space. A reticle was used to produce the stitched sensor, this can be seen in figure 2.17. The process of fabrication is similar to that used in CCD production. Stitch blocks A,B, C and D in figure 2.17 are repeated with precision across the entire wafer, constituting the 54mm square design. Block B is a 270x270 pixel array, therefore a 5x5 matrix of stitched blocks compose one sensor. Stitch block D is the top or bottom and contains the reset circuitry or the readout shift registers respectively. Block A holds the row logic. The corner stitching (block C) is merely to 'fill the gaps'. It is used as a bonding site and also holds a some circuitry on the corner stitched blocks which is only required once, such as a reset bias [33].

Regions Of Reset (ROR) and Regions of Interest (ROI) are defined using configuration shift registers. These are located in the vertical and horizontal edges of the stitching.

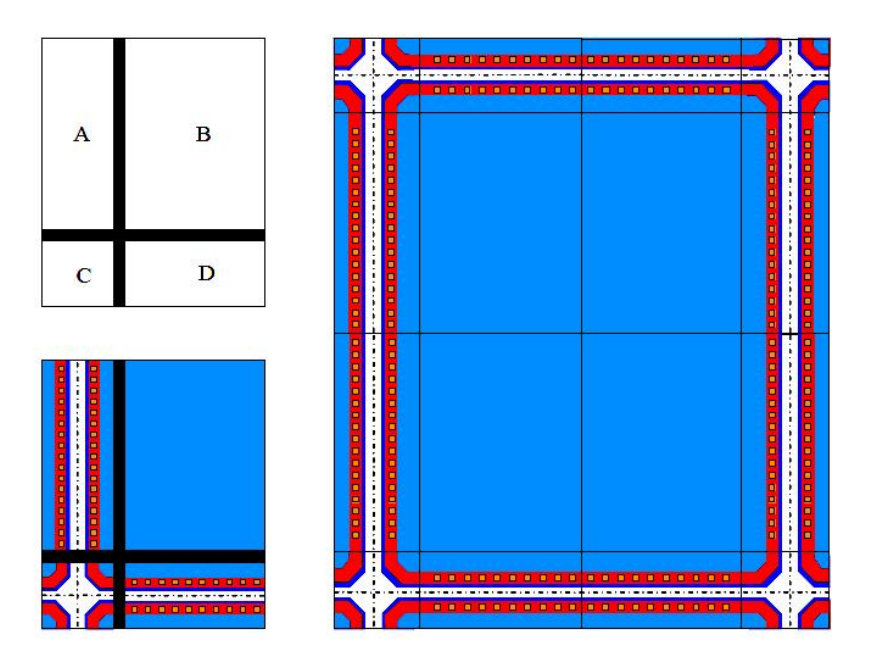


Figure 2.17: A CMOS reticle illustrating the stitching patterns used to fabricate the Large Area Sensor

By programming the registers regions of increasing integration time can be defined. The shortest integration time will always be in the centre of the array or at one corner, as it is not possible to have longer integration times surrounded by shorter ones. The regions can be set for any number of rows or columns. The sensor provides up to three regions of different integration times. Figure 2.18 illustrates this principle. As seen from the right side image in this figure, the ratio between different reset sizes can be varied. This is achieved by varying the number of rows read out between each reset token in the registers [34].

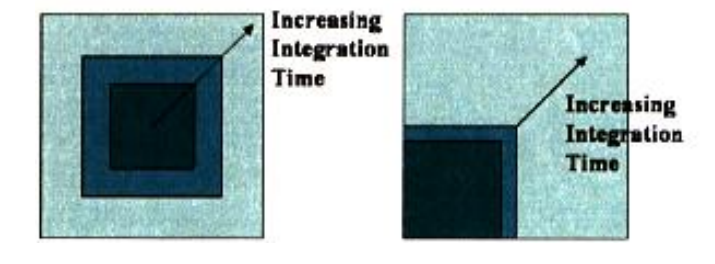


Figure 2.18: Regions of reset defined by varying integration times

Due to the dependance on the number of rows, dynamic range is therefore dependant on the frame rate (integration time). At a maximum of 20 fps the maximum integration ratio is 1350:1, giving an effective gain in dynamic range of 62dB (maximum) [34]. More information concerning readout and Regions of Reset can be found in the IEEE Transactions on Nuclear Science paper by Andy T. Clark et al. [34]

Table 2.3 summarises the measured performance of LAS from testing and characterisation carried out by the CMOS Sensor Design group at the Rutherford Appleton Laboratory.

Measured Performance	Value			
Pixel Size	$40\mu\mathrm{m} \times 40\mu\mathrm{m}$			
Array Format	1350×1350			
Die size	58mm x 58mm			
Full Well	90000 e ⁻			
Read Noise (Soft - Hard reset)	40e ⁻ - 62e ⁻			
Dynamic Range (for single Direct reset)	$66.9 \mathrm{dB}$			
Gain	$7.7e^{-} DN^{-1}$			
Full Well (with multiple resets per reset)	$35000e^{-}$			
Dynamic Range (multiple resets)	>135dB			
Maximum frame rate	20 fps			
Analogue Outputs at 5MHz	10			

Table 2.3: Measured sensor performance of LAS to date. Table obtained from Andy T. Clark *et al* [34] published report.

2.7.3 Analogue-to-Digital Conversion

When an image is obtained from an active-pixel sensor it is done so because of analogue-to-digital conversion (ADC). As the name implies, this is when an analogue signal (commonly a pulse shape) is converted into a digital signal of binary code (1's and 0's). An analogue-to-digital converter controls how many samples are taken per second (sampling rate) and how many different gradations (quantisation levels) are possible when taking the sample (sampling precision). Figure 2.19 illustrates both of these parameters. The original pulse shape in the figure is shown as the red line. The analogue-to-digital converter looks at the wave and picks the closest number between 0 and 18. The number chosen is shown along the bottom of the figure. By increasing the rate (the values on the y-axis) and the number of gradations (how many columns there are) the digital conversion fits the original pulse shape better each time. This is known as Wilkinson run-down ADC or Digital Ramp ADC [35].

Flash ADC involves a series of comparators, or logic gates, and an encoder. The principle however remains the same, producing a binary output. In this case the input analogue pulse is compared to a set of unique voltages. Figure 2.20 [35] shows how a 3-bit flash ADC circuit works. When the analogue input voltage exceeds the reference voltage from a precision voltage regulator the comparator outputs produce a signal pulse which is translated by the encoder to produce a digital binary output. For example, if the analogue voltage triggers the third comparator then the output digital pulse will

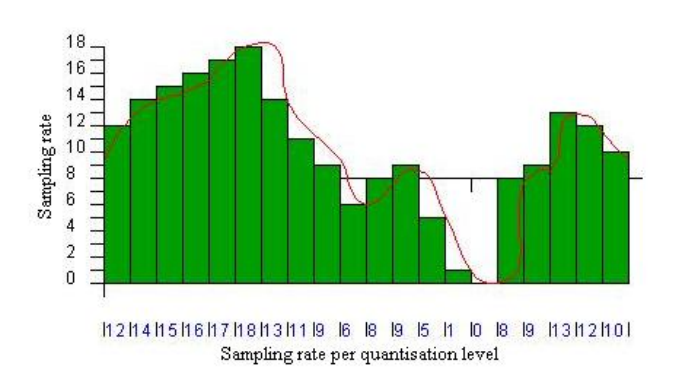
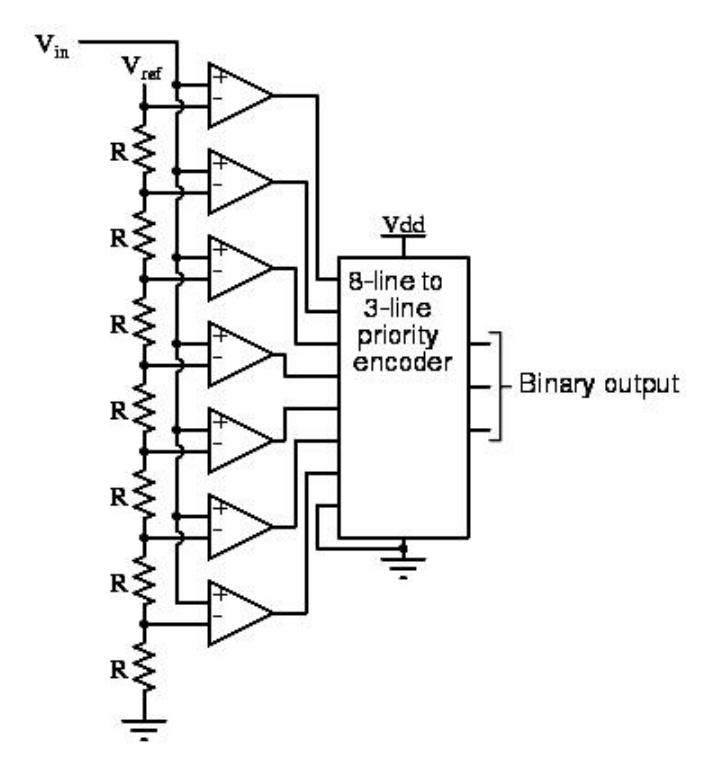


FIGURE 2.19: Wilkinson run-down method of analogue-to-digital conversion



read 00100000. This repeats until the complete digital signal has been generated.

ADC is measured in arbitrary values or measures of "least significant bit" (lsb). The lsb is the bit position in a binary number determining whether the value is odd or even. It is sometimes referred to as the right-most bit. Within ADC there is likely to be error, of which the most common is quantisation error. This stems from the finite resolution of the converter. The magnitude of this error at any given finite element of time is between 0 and one half lsb. In the previous example of an eight bit converter, an error of one lsb is roughly 0.4% of the full range signal (1/256).

2.8 Spatial Resolution

The determination of the spatial resolution of an object or medium is being able to distinguish between intensities at closed spaced points. The spacing of these points and how well a detecting system can record radiation intensities at these points is what determines this. The requirement for spatial resolution in position sensitive detectors is much stricter than for imaging systems, dependent upon application. In high energy experiments, a position resolution in the order of micrometers can be very common. Spatial resolution is a key parameter to characterising a detection system and is therefore commonly application dependant; i.e. the requirement of what type of detection system needed for an application will depend on the systems spatial resolution. Spatial resolution is often limited by the pixel size on the detector. A smaller pixel increases the spatial resolution of an imaging device as the array of pixels will be increased. Although this is beneficial with regards to the signal-to-noise ratio (the photon flux that smaller pixels receive is reduced), carrier crosstalk is more likely to occur. This is not the only cause of degradation to the resolution: aliasing may also typically occur.

2.8.1 Crosstalk

Crosstalk is essentially the detection of electrical signals from nearby signal lines and devices [19]. There are many electrical components in a detection system, as seen with LAS. Signals received by an individual channel can be transferred to a neighbouring channel. Detectors based on a single area of material are most likely to be affected. Within LAS carrier crosstalk is therefore most profound in stitching blocks A and D in figure 2.17 containing the reset circuitry, the readout shift registers and the row logic. The signal charge carriers in the detector become scattered due to undesired capacitive coupling from one part of the circuit to another. The detector then provides alternative paths and the charges are picked up by neighbouring channels. This problem is rendered

with increased spacing in the detectors structure, re-wiring or shielding from electrical discharge.

2.8.2 Aliasing

An image can obtain unwanted information, i.e. data that the original object did not contain. The image produced by the detection system is then untrue and has been altered from what should have been detected. In other words, a blurring of the true image. This effect is known as aliasing.

The unwanted information is artificially produced by wrong image construction or wrong sampling. Sampling is the gathering of spatial information at regular time intervals. It is this information which is then passed to the converters. When an irregular time interval gets sampled, this is wrong sampling. The NyquistShannon sampling theorem states: "An image can be faithfully reconstructed if the sampling frequency is greater than or equal to twice the bandwidth of the input signal" [36]. At different spatial intervals shades occur in the image. Each of these have different frequencies due to irregular variations. A Fourier spectrum clarifies the number of frequencies which exist, with the maximum corresponding to the bandwidth of the system. Mathematically the Nyquist-Shannon theorem can be expressed as:

$$f_s > 2B \tag{2.17}$$

where f_s is the sampling frequency and B is the detector bandwidth. 2B can also be classified as the Nyquist frequency (f_{Nyq}) as the bandwidth coincides with the highest frequency of sampling. It can therefore be written as:

$$f_s < f_{Nua} \tag{2.18}$$

When this statement holds true it can be said that the image will be aliased. Reconstruction of an image can be accomplished by either multiplying the convoluted frequency spectrum or with the use of a sinc function [19]:

$$sinc(x) = \frac{sin(\pi x)}{\pi x} \tag{2.19}$$

The function represents the Fourier transform after convolution of the frequencies. For further explanation into aliasing and reconstruction of images, see reference [19].

2.8.3 Spread and Transfer Functions

The spatial resolution's point spread function (PSF) of the generated image determines how well a detector is able to distinguish between two non-aliased points separated in space. The line spread function (LSF) is similar to this whereby it uses a technique to quantify the spatial resolution. Basically, the image of an ideal line (or point for the PSF) is recorded. The pixels are regarded as individual detectors separated by a small distance. Assuming the radiation is monochromatic and perpendicular to both surfaces the lines (or points) are detected upon, a Gaussian distribution can be obtained. This is because the highest intensity will be in the middle of the image and will rapidly decrease towards the edges. The Gaussian must be plotted as intensity against any one co-ordinate. If the distance between adjacent points on the line (or two spots for the PSF) is equal to or larger than the full width at half maximum (FWHM) of the Gaussians, then the detector will be able to distinguish between points on the line or equivalently for the PSF. This is demonstrated in figure 2.21. However, light sources are not always monochromatic, hardly ever perfectly perpendicular to the surface and never produce an ideal line. The solution is the edge spread function (ESF).

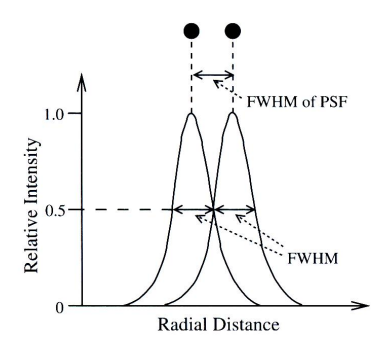


Figure 2.21: PSFs of two points as images, separated by a distance equal to their FWHM

2.8.3.1 ESF

Determination of the ESF is a much more convenient route to obtaining the LSF as it works on the principle of a step function. Metaphorically, an image is "cut" where uniform intensity exists to reveal a knife-edge; figure 2.22. This essentially becomes the ideal line previously sought after. Differentiation at the step function of the knife-edge image will allow the derivation of the LSF.

$$LSF(x) = \frac{d}{dx}[ESF(x)]$$
 (2.20)

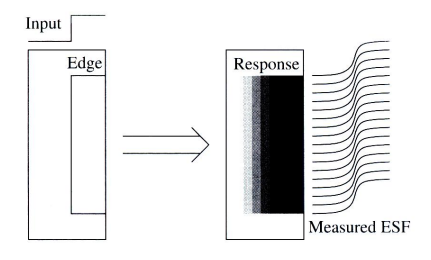


Figure 2.22: An object with sharply defined edges placed between the light source and detector can produce a knife edge image from which the ESF and therefore the LSF can be obtained

2.8.3.2 The Modulation Transfer Function

The modulation transfer function (MTF) is the end and optimum result for determining the spatial resolution of a detector system and is the most widely used index. It is the transfer ratio between the imager input and output signal modulations as a function of the input signal, i.e. it determines how much contrast of the original object has been maintained by the detector [19]. The optimum resolution is achieved when the MTF is 1.0 on a normalised plot; however this is near impossible. In theory the modulation function needs to found and understood. The MTF is then simply the modulation of the image as perceived by the detector divided by the modulation of the stimulus (the object).

Contrast is defined as the amount of light transmitted which is analogous to the amount of light measured in terms of luminescence [28]. When plotted graphically this will remain positive at all points, as proven in figure 2.23.

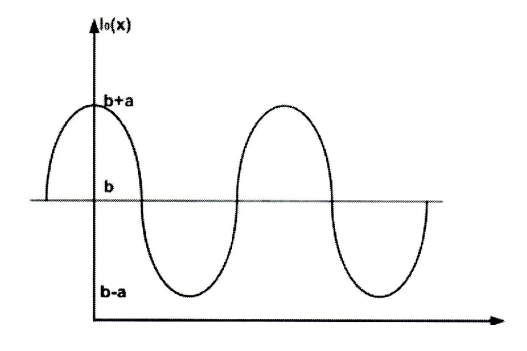


FIGURE 2.23: A representation of any convenient function for quantifying the contrast

The modulation can be defined from the graph as simply

$$Modulation = \frac{a}{b} = \frac{N_{max} - N_{min}}{N_{max} + N_{min}}$$
 (2.21)

where N_{max} and N_{min} are the maximum and minimum values of the function used to quantify the contrast. There is modulation in both the image and object however, so the modulation transfer ratio (MTR) is simply image modulation divided object modulation. At each varying spatial frequency the (MTR) must be calculated as it is a function of spatial frequency. The dependance of this is the modulation transfer function.

2.9 Quantum Efficiency

The definition of quantum efficiency (QE) depends on the system it is in reference to. In the case of the photomultiplier tube quantum efficiency is the ratio of number of incident photons and the number of generated photoelectrons. This is not the case for x-rays or a detector. Each individual element of a system carries its own efficiency, and the combined effect of these need to be taken into account to obtain a realistic measure of the signal-to-noise ratio. That directly related to the process of detection is known as quantum efficiency. Quantum efficiency in this circumstance characterises how efficiently X-ray photons are absorbed in the detector volume. This is because absorption efficiency is directly related to the generation of electron-hole pairs resulting in the efficiency of signal generation and hence detection.

The passage of photons through matter can be described by the following form:

$$\frac{I_o - I}{I_o} = 1 - e^{-\mu x} = QE \tag{2.22}$$

Here I is the photon intensity at an attenuation length x, I_o is the incident X-ray intensity and μ is the attenuation coefficient. The numerator over the denominator equates to the quantum efficiency of the material.

Detective quantum efficiency is similar to that of the quantum efficiency, however the result is the product of the resolution and noise on the system as well as the QE. It is a measure of the systems overall performance. The theory and evaluation behind this parameter can be found elsewhere [19] [37] [38] as it is not discussed here as it is not used. This is because of the time limit and impracticality of such a parameter. The work carried out in this investigation is to produce a suitable detector system which meets the needs of the application to the best of our ability in the time given. In time

one could research more detailed specifications and bring the detector system up to a more effective performance: i.e. characterisation of the systems detective quantum efficiency [29].

Chapter 3

Experimental Arrangement

Throughout each important stage of the investigation it is necessary to explain the procedures took in arriving at the results collected. This chapter of the report looks at how programming software, additional products, the CMOS APS (LAS) and its software, a silicon pin detector and the types of scintillator material used will all play a major part in obtaining the results required to aid in the production of a high energy X-ray imaging detector for I12 at the Diamond Light Source. Firstly a discussion regarding how the whole set-up is going to be operated including new hardware and existing apparatus upgrades.

3.1 LabVIEW

At the very start of this placement, before any experiments could begin being carried out, the set-up of the apparatus needed modifying. The investigation was to use a Seifert, Tungsten filament X-ray machine. The head of the X-ray set was controlled by a laboratory software program named LabVIEW (Laboratory Virtual Instrumentation Engineering Workbench), using safety interlocks on the doors of the set to ensure movement of the head could only occur when these were locked shut. A LabVIEW code had previously been written to control movement in x- and y-axes. The front panel screen (one of the user interfaces; the other being the block diagram screen) of the existing code is shown in figure 3.1. This was the main "controller" for the head movement.

Each LabVIEW code is named as a Virtual Instrument (VI): a program which implements functions of an instrument. In the block diagram screen of the program various VI's, control switches and indicators are joined together to form the output on the front

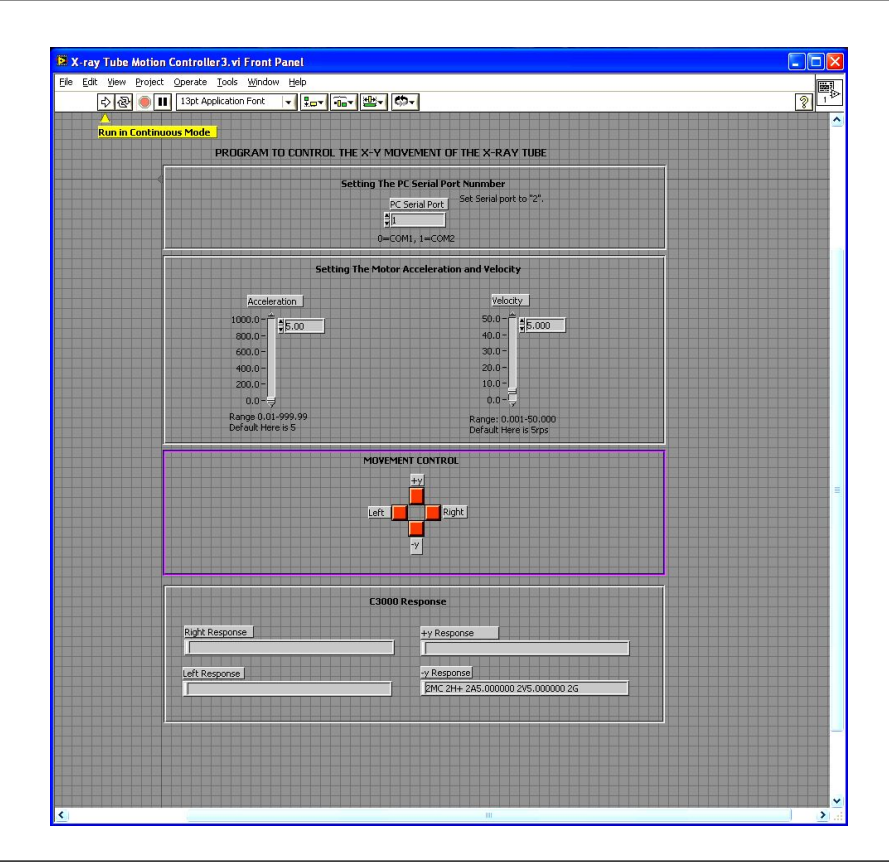


FIGURE 3.1: Front panel view of the X-ray Tube Motion Controller VI

panel. Similar to before there was a code previously written for a similar application to this investigation which controls the X-ray head for scanning pixellated detectors. This program needed combining with a unique code yet to be written which shall control the movement of LAS and the hardware it is to be mounted upon.

3.1.1 Linear and Rotational Movement of LAS

The investigation would use an XPS Motion Controller, a z-axis linear movement stage and a theta rotational movement stage (all purchased from Newport Spectra Physics), of which the two movement stages will be used as a platform for the LAS stack. The built in driver cards in the XPS will control the stages using a LabVIEW program; the VI's of which are pre-programmed into the XPS' software. Via ethernet connection to a regular desktop PC the VI's can be used with the existing LabVIEW program. A program was then able to be written and combined with the pixellated detector scanning code which would control the movement stages and the X-ray head. Movement inside the X-ray cabinet could now be controlled in x-, y-, z- and theta rotational axes. The front panel for the combined program is displayed in figure 3.2.

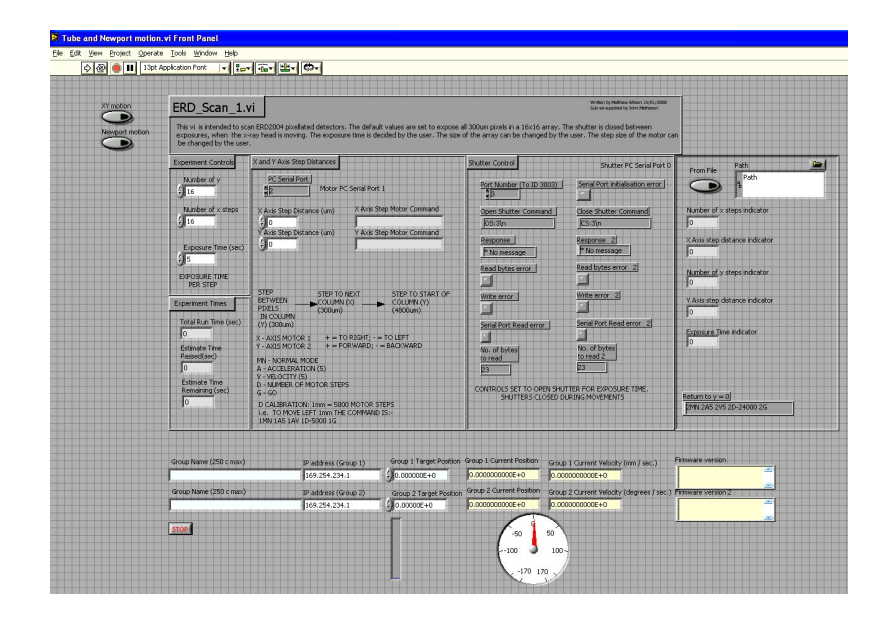


Figure 3.2: Front panel control for the movement of the X-ray head and Newport stages

The majority of the boxed in commands and controls are the original pixellated scanning program written by Matt Wilson in January 2008. Some of this has been modified however to allow for the conversion to LAS. The further most right hand box was one of the modifications made. This allows for data to be read into the program from a .txt or .xls file for example. The two "push buttons" in the top left corner are the most important however; these are essentially the primary on/off switches for the X-ray head movement and the Newport stages.

Towards the bottom of the image is the new code that had to be written into the existing program. The two group names are GROUP1 and GROUP2 which control the linear and rotational stages respectively. The other control and output panels indicate the target position, current position and velocity of the two stages. The block diagram view for the addition of the Newport stages and its code is seen in figure 3.3. Note: the rotational stage is set at a mid position of 0 and can move either 170° anticlockwise or 170° clockwise from this position; hence the values on the adjustable dial controller.

3.2 X-ray Cabinet Upgrade and Workshop Products

To allow for the insertion of the Newport stages into the X-ray cabinet the X-ray set needed upgrading. The stages were to fasten securely to the existing framework built into the cabinet by use of additional scaffolding specially designed to attach via vertical and horizontal platforms. The Aluminium scaffolding is secured in placed by bolts

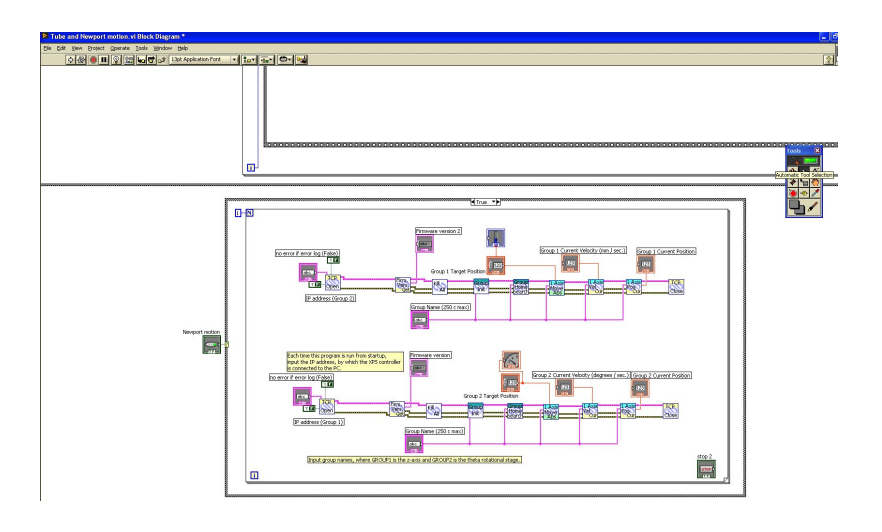


FIGURE 3.3: Block diagram for the Newport stage movement and addition to the original program for the X-ray head control. This is the panel where the controls parameters and outputs on the front panel are programmed in

and specially designed nuts which fit the runs inside the rigging structures. Figure 3.4 displays the X-ray cabinet with the upgrades made. The added platforms required for the fastening of the Newport stages are seen in the center of the photo with the theta rotational stage mounted on top (the linear z-axis stage is on then on top of that). The X-ray head is seen towards the top with the photo taken from the front of the cabinet where the doors are located.



Figure 3.4: X-ray cabinet with horizontal Aluminium platforms added to secure the Newport stages in place

To mount and securely fasten the LAS stack to the z-axis movement stage, mounting plates had to be ordered from Newport Spectra Physics once again as well as being made by the workshop in building R12 on the RAL campus. Calculations, designs and officiated sketches were produced to allow for the connection to LAS. An example can be found in Appendix A. One mounting plate was designed and produced by the workshop as well as three different masks. These were of great importance to results as well as the procedure.

It was known at this point that a scintillator with a surface area equal to that of the effective area of LAS had to rest on top of the CMOS APS. To secure this in place, a carbon-fibre mask was designed and further created by the workshop once again which would hold the scintillator material in place. So as not to affect the attenuation properties of the APFPI a square area equal to that of the sensing area of LAS was cut from the center of the carbon-fibre, except for a 3mm overhang perimeter. This 3mm ledge would then press down on the scintillator holding it in place. Clearance holes were drilled at calculated points which would secure the mask to the LAS stack via M3 threaded screws. An identical replica was made out of 2mm lead for higher energy applications and again out of carbon-fibre, however this time without the central window cut out (again, for high energy application). A photo of the four manufactured workshop products are shown in figure 3.5.

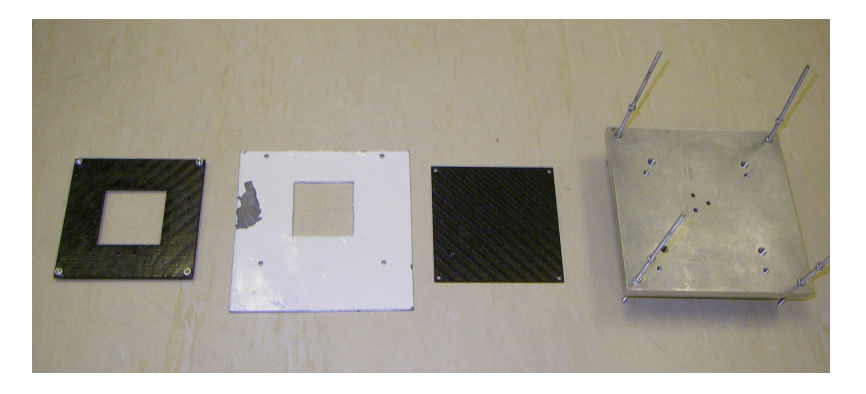


Figure 3.5: Manufactured mounting plate (far right) and scintillator securing masks in lead (painted white here) and cured carbon-fibre

3.3 LAS and OptoDAQ

The set-up of LAS is key to this investigation, both hardware wiring and software operation must be known extensively. With help from Andy Clark the correct configuration of the ethernet connection to the PC and the FPGA board (Field-programmable gate array), the power supply connection with mains to the FPGA board and a 12V DC

potential to the LAS stack and the IDE cable between the board and the stack was easily replicated. The software with its OptoDAQ program had a steeper learning curve. OptoDAQ is the name of the in house developed Data Acquisition (DAQ) system, the opto part refers to the fact that the communication with the PC is via a fibre optic ethernet cable.

3.3.1 Hardware

There are two main parts to the LAS operation in terms of hardware: the FPGA board and the stack, connected to one another by an Integrated Drive Electronics (IDE) cable. Figure 3.6 shows the FPGA board to the left and the stack to the right. The LAS stack can be seen to have the carbon-fibre mask mounted to it in this photo. To initiate operation of the sensor the the FPGA board must first be turned on with the on-board on/off slider switch, only then can the DC power supply to the stack be turned on. To shut the sensor down this must be completed in reverse order. This protects the electronics from any sudden power surges and was indicated by Andy Clark as the safe way to start up and power down the sensor.

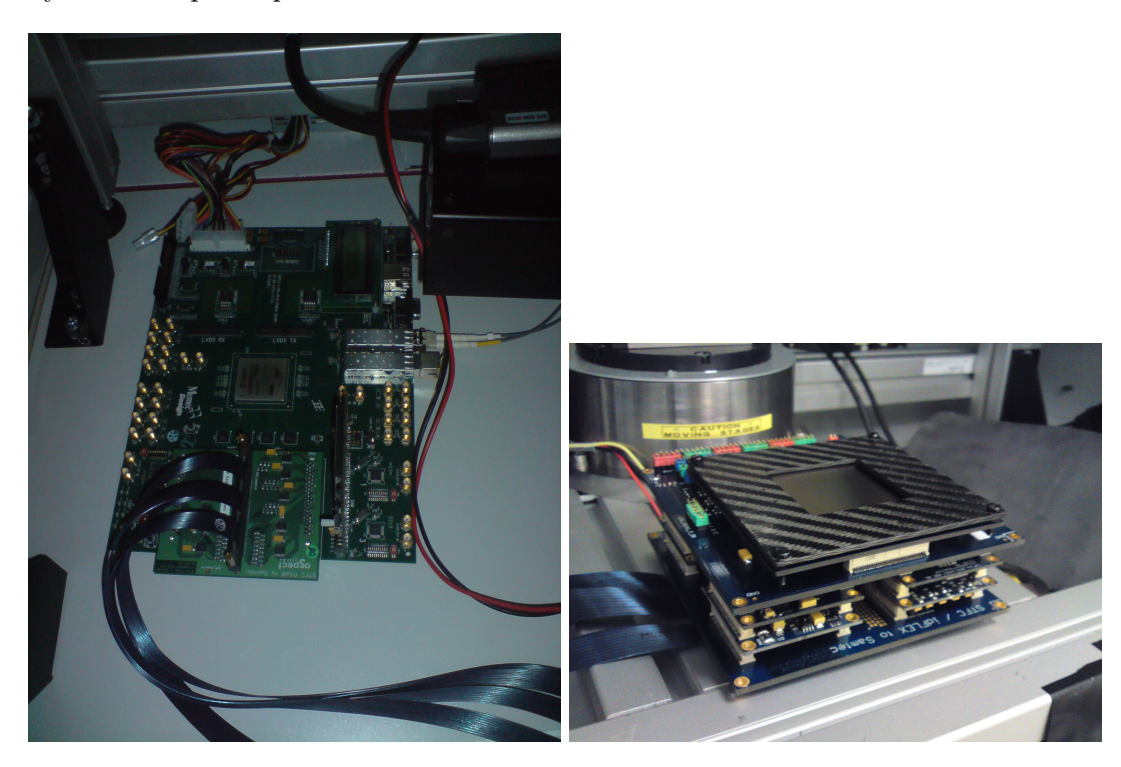


FIGURE 3.6: FPGA board (right) and LAS stack (left)

3.3.2 Software

Once the hardware was powered up the OptoDAQ software could be run. Initiating the software would take the DC power supply up to 1600mA (which was set as a limit on the current scale) from around 900mA. The full operation of all the OptoDAQ properties can be found in Appendix B; the OptoDAQ User Manual.

With referring to figure 3.7 the software is started by clicking "Restart" and then the new page icon followed by "Live View" once loaded up. An image should now appear in the central viewing screen; this is what the sensor is detecting. The histogram in the bottom right corner quantifies the abundance of ADC levels being detected, comparison between the left and right images in figure 3.7 aid in understanding this feature.

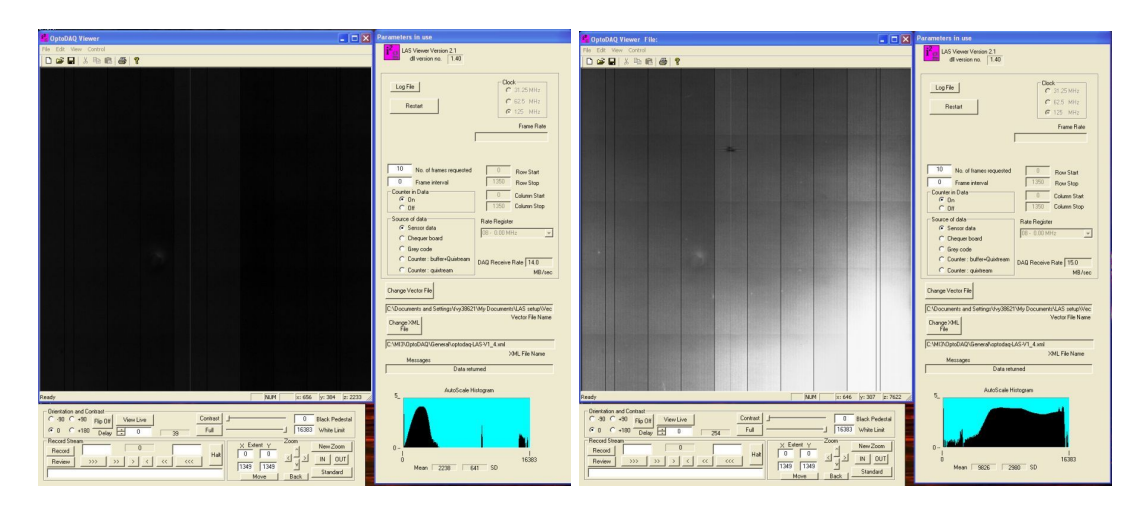


FIGURE 3.7: The OptoDAQ program used to run LAS and record the data the sensor images

In both images in the figure, stitching errors and columns of readout error are present. These are explain in more depth in the following Results chapter.

3.4 Dark box set-up and Temperature Correction

It was observed in this investigation that temperature response of LAS was quite a significant problem. Discussed to a fair extent in the Results chapter of this report are the experimental findings of such an effect.

To carry out temperature experiments on LAS, it was placed in a radiation sealed (although not necessary), dark box where a fan could be introduced into its environment to aid in monitoring the temperature. The box was covered with a tight fitting lid so that temperature detection would not be influenced by loss of heat from the system to

the ambient surroundings. Figure 3.8 is a photo of the set-up.

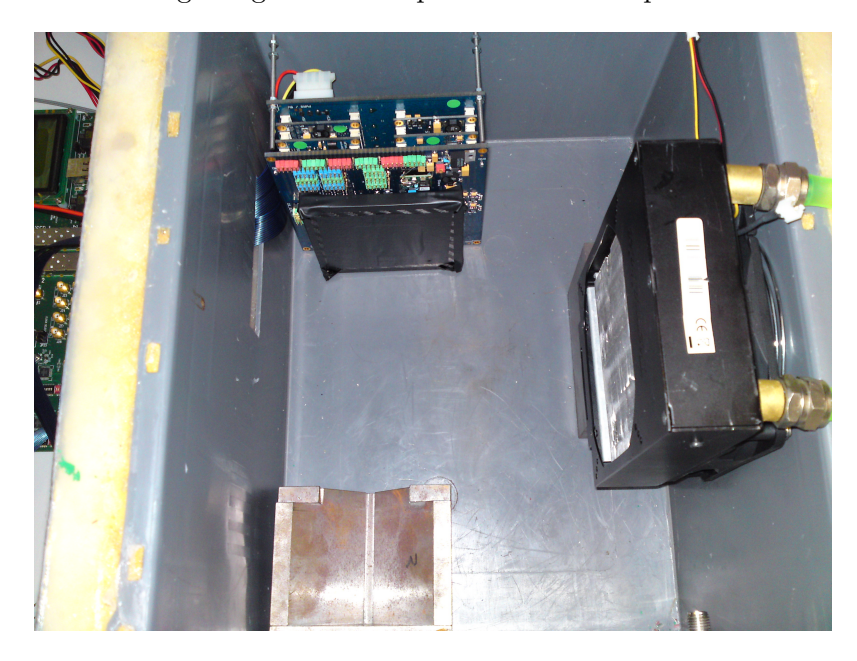


FIGURE 3.8: The LAS stack positioned in the dark box, with black tape covering the center of the carbon-fibre mask and the edges of the sensor. This method models a 'completely' dark environment and prevents moisture from the fan reaching the sensor surface

The LAS wafer (which fastens onto the stack by means of three conventional Peripheral Component Interconnect (PCI) slots) had a basic microelectronic temperature sensor fitted to the underneath of it which was itself wired to a Lakeshore 332 Temperature Controller. The fan in the box cooled LAS using a standard laboratory coolant pumped by a Grant R20828003 Coolant Holder and Grant GD120 pump from Cambridge Ltd. With this set-up results could be recorded for varying dark current on the pixels on LAS and how this was affected by temperature.

3.5 The Silicon Pin Detector

One of the most important experiments which shall be covered in this investigation is the amount of stopping power each tried and tested scintillator material possesses. Stopping power experiments are important because they will determine whether or not that specific scintillator can be submitted to light output tests with the CMOS image sensor. Ineffectiveness to stop all x-rays up to 50kV operating potential of the X-ray set, will mean that a certain percentage of x-rays will pass through the material and damage the pixellated technology of the sensor due to increased radiation dose.

Each scintillator material to be investigated with was placed over a silicon pin detector

and shone x-rays down onto it collimated at $300\mu\text{m}$, using the collimator securing into the interlock system on the X-ray head. The collimator will be placed as close at possible to the scintillator without applying any force upon it. The operating tube voltage was increased at constant increments (usually 5kV) while tube amperage was held constant at 30mA. The aim was to determine the current induced in the detector using a Keithley 6517A picoameter which also supplied a voltage of 30V across the pin detector. In theory; the varied tube voltage leads to different energy X-ray radiation incident upon the pin detector hence exciting the electrons and giving them charge. This in turn causes an induced current in the device; this is what is being measuring. Due to the excitation of the electrons the Keithley will be reading a negative current rather than a positive one from the hole-pairs the electrons leave vacant. If the wiring inside the pin detector was reversed, then -30V should be applied. This means one would measure the current across the hole pairs not the electrons. The device is set to take an average of one hundred micro-amp readings for the results. Figure 3.9 schematically shows the wiring of the apparatus between the silicon pin detector and the Keithley device.

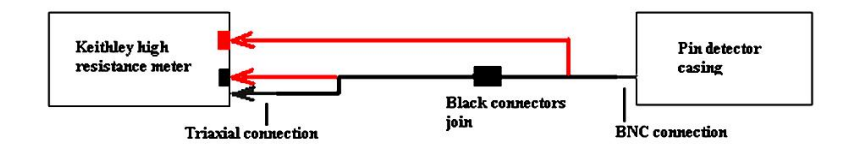


FIGURE 3.9: Connecting the detector and the picoameter using Bayonet Neill-Concelman (BNC) and triaxial connections. Red and black lines note the colour of the wires used and the terminals to which they plug into on the corresponding device

Figure 3.10 is a photo of the $300\mu m$ collimator closely positioned over one of the large area scintillator plates resting on the casing of the silicon pin detector. The collimator is adjusted in x- and y-axes so that it lies directly over the $263\mu m$ thick silicon diode.

3.6 Experimental Measurements

In addition to the operation of LAS the other main procedure in this report outlines the importance of choosing the correct scintillator materials and their expected performance. Most of this is detailed in the Results chapter also, however an introduction to the materials selected and purchased will be described in the section to follow.

The experimental arrangement of the measurements analysed and discussed in the results also encompasses a major method used to determine the modulation transfer function parameter of the combined scintillator and CMOS sensor (otherwise known as the APFPI). The most convenient methods were researched and discussed between Matt



Figure 3.10: Photo of the X-ray head with $300\mu m$ collimator placed over a scintillator plate resting on the Si pin casing

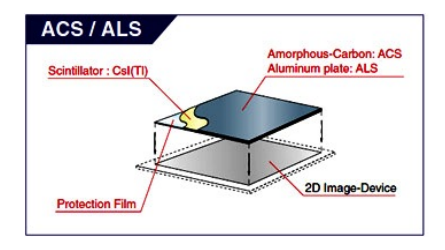
Wilson, Paul Seller and myself. The findings and agreed procedures are reported in this section.

3.6.1 Scintillator Materials

When research began on this investigation, the search was on to find a suitable, high performing scintillator which met the needs of the application the Diamond Light Source requested. Firstly four crystal samples were purchased from Hilger Crystals Inc.: Bismuth Germanate (BGO) - 5x5x1mm, Lutetium Yttrium Orthosilicate (LYSO) - 1.4x1.4x11mm, Cadmium Tungstate (CdWO₄) - 15x15x1mm and Zinc Tungstate (ZnWO₄) - 9.6x9.6x3.5mm. Reviews of these materials will include results on their stopping power, light output and spatial resolution. Some problems did occur however, for example incorrect circuit wiring

in the stopping power tests and insufficient surface area on the samples. Despite this results were obtained and are described in the following chapter.

The sample materials used for light output and stopping power testing purchased from Hilger Crystals were adequate scintillators however the size issue needed to be overcome. To solve this, a more commercially available scintillator was purchased from Hamamatsu Photonics: Thallium doped Caesium Iodide (CsI(Tl)). Previous advertising from this company within other research departments at RAL was the initial reason why such a range of products offered were drawn to the division's attention. Hamamatsu Photonics supply a wide range (up to 14 or more) of various thickness CsI(Tl) scintillators mounted upon different substrates. Figure 3.11 schematically shows the scintillator plates purchased from Hamamatsu Photonics. The fibre-optic scintillator (FOS) plate and the amorphous-Carbon scintillator (ACS) plate were purchased twice; one with a high light output property and the other with a high resolution property. The Aluminium scintillator (ALS) plate was only available in one type: 70% light output. Properties of the plates are displayed in table 3.1.



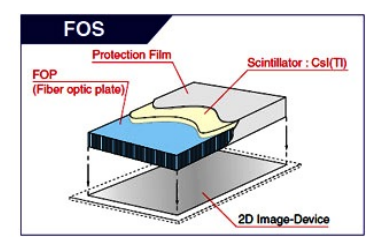


FIGURE 3.11: Purchased FOS, ACS and ALS plates from Hamamatsu Photonics [39]

Protecting the CsI(Tl) on each plate is the substrate itself (whether this is a fibre-optic plate, 500μ m of amorphous-Carbon or 1.0mm of Aluminium) and a protective film. With so many interfaces the quantum efficiency of the system will be hard to calculate, however this is something to analyse at a later date. As seen from table 3.1 the effective area of each scintillator is 2-3mm less than the substrate area. This is simply to protect the scintillator as fabrication of the plates require the Caesium Iodide to be mounted onto the substrate and then covered with the protective film. The latter covers the scintillator sides so no total internal reflection of light can be detected from the sides of the product, making it more efficient.

Apart from previous advertising of the Hamamatsu plates within RAL, good product feedback, ideal effective and substrate area and easy of purchase; CsI(Tl) was decided upon as a good scintillator for a number of reasons:

• CsI(Tl) is one of the brightest scintillator materials with a maximum, broad emission situated at 550nm.

High Light	O/P	or High Res.	HL		HR		HL		HR		N/A	
CLF	(10 lp/mm)	(%)	18		33		12		25		20	
$\mathbf{Relative}$	Light	O/P (%)	20		40		125		50		70	
Effective Substrate	$\operatorname{Thickness}$		$3.0 \mathrm{~mm}$		$3.0~\mathrm{mm}$		0.5 mm		$0.5~\mathrm{mm}$		1.0 mm	
${ m Effective}$	\mathbf{Area}		47x47 mm		47x47 mm		48x48 mm		48x48 mm		48x48 mm	
${f Substrate}$	Dimension		20x50 mm		50x50 mm		50x50 mm		20x50 mm		50x50 mm	
${f Scintillator}$	Type		$CsI(Tl)$ - $150\mu m$	${ m thickness}$	$CsI(Tl) - 150 \mu m$	$_{ m thickness}$	$CsI(Tl) - 150 \mu m$	${ m thickness}$	$CsI(Tl) - 150 \mu m$	$_{ m thickness}$	$CsI(Tl) - 150 \mu m$	${ m thickness}$
$\operatorname{Description}$			Fibre Optic	Scintillator	Fibre Optic	Scintillator	Amorphous-Carbon	Scintillator	Amorphous-Carbon	Scintillator	Aluminium	Scintillator
Product	Code		2299f		J6677-01		J8734		J8734-01		J8978	

Table 3.1: Properties of the purchased scintillator plates from Hamamatsu Photonics [39]

- CsI(Tl) has a high light output of 54 photons/keV.
- Using pulse shape analysis, CsI(Tl) can be used for particle discrimination which could be used in further testing experiments.
- \bullet No radiation damage is likely to occur as CsI(Tl) is only significantly effected above 10 Gray radiation dose.
- Maximum scintillation emission intensity for CsI(Tl) is measured at about 25-30°C.
- CsI(Tl) can be grown in a structured form with columns of 6μ m in diameter using a patterned substrate to reduce lateral spreading of fluorescent light.
- CsI(Tl) has a dual caesium/iodine K edge around 33keV.
- CsI(Tl) is superior with X-ray diffraction due to its short decay time and availability of micro-structured form.
- For Hamamatsu scintillators, packing fraction is 75% (75% of surface area of sensor is coupled with fibre core, so 25% is covered by fibre cladding). This increase the quantum efficiency of the plates.

3.6.2 MTF procedure

Determining the spatial resolution of the APFPI was an important part of the investigation. After research into former methods used by other experimentalists and trial and error with the Hamamatsu scintillator plates, a precise way of calculating the modulation transfer function was found.

As previously described in the Spread and Transfer Functions subsection in the Scientific Background and Theory chapter, the edge-spread function (ESF) of a knife-edge image needs to be evaluated. To obtain this knife-edge a semi-circular aluminium plate was originally used. At high energies this was found to be unsuccessful in stopping x-rays and so later a 4mm thick sheet of lead was used in place. Collimated to $100\mu m$ or $300\mu m$ it was not possible to obtain any kind of edge to the illuminated image. A tube of roughly 7mm was used for this instead. This allowed for the X-ray set to function as

the interlock on the X-ray head was overcome. Figure 3.12 schematically described the set-up of the apparatus and the observed illumination by LAS.

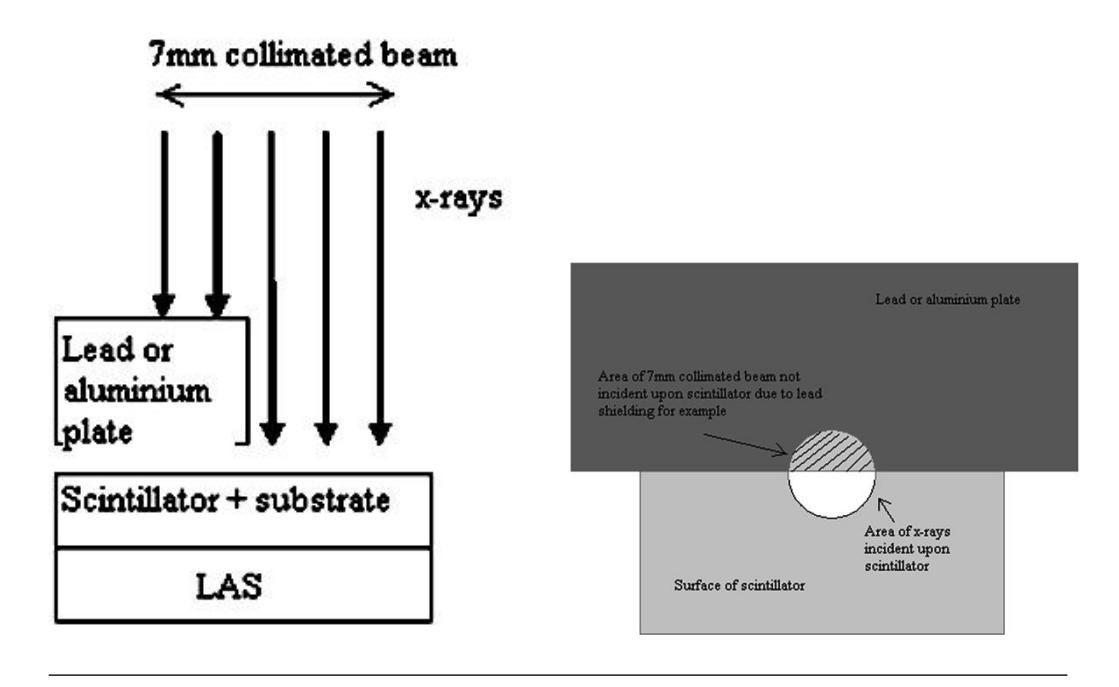


FIGURE 3.12: Collimating the x-rays using to approximately 7mm in diameter allowed for a knife-edge image to be achieved by blocking half of the circular collimation with lead

The image LAS perceives as a result of this method is shown in figure 3.13. The top edge shall be used as the knife-edge for the ESF determination. In order to obtain the ESF the output ADC is analysed down one column and plotted against row number which will be converted into a distance of millimetres (recall that each pixel has dimensions of 40μ m by 40μ m). To achieve a better result with more data points a similar method is followed to that used by Fujita et al [40]. The lead or aluminium plate shielding is placed at a small angle (approximately 2°). In theory this method uses neighbouring columns to sample signal amplitude on sub pixel distances. ADC values are taken across several adjacent columns, building up an array of data for one pixel and then repeating over the width of the sensor. For the small angle being used it is chosen that seven columns are to be analysed as too many would lead to distortion and over sampling in the data and too few would produce insignificant effect in the analysis. So when plotted instead of simply having one data point for row 700 say, there will be seven, giving a total of 9450 data points (1350 rows multiplied by 7).

The arrow in figure 3.13 indicates the direction of analysis down the chosen column with figure 3.14 displaying an up-close image of the fluoresced knife-edge clearly showing the small angle at which the edge is inclined at.

Figure 3.15 however describes the process just discussed, modified from Fujita *et al* [40]. The idea of over sampling is easier to understand with reference to this figure. For

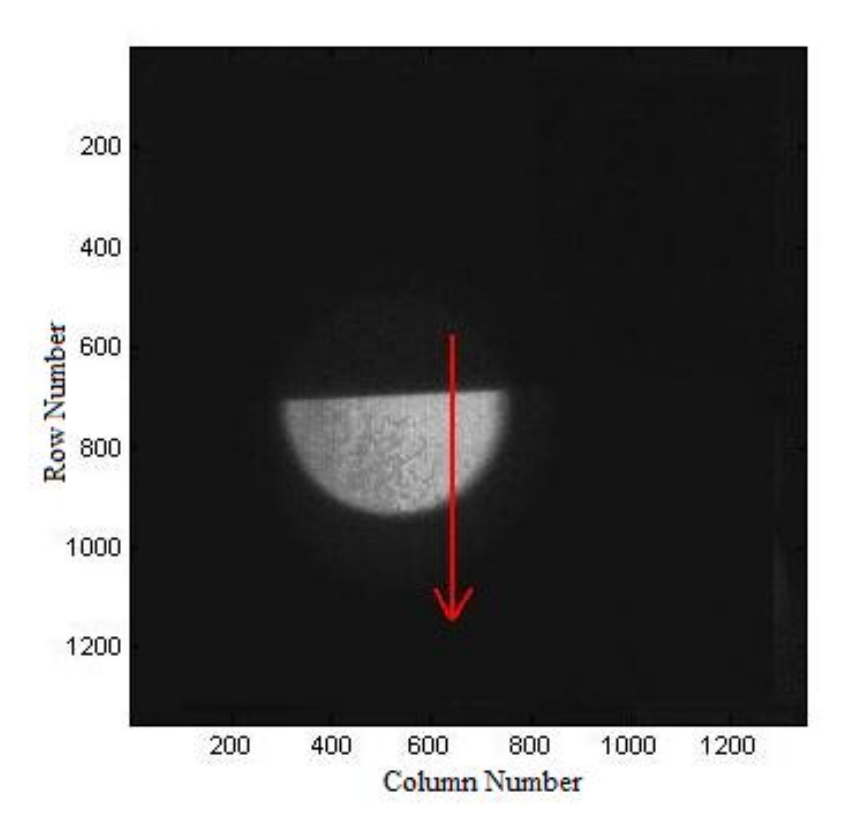


Figure 3.13: Raw image of wide collimated spot, using lead shielding to give rise to the knife-edge. The red arrow indicates the columns down which the line spectra of ADC is taken from

example, if one chose to analyse along eight columns then pixel 8 (now being adjacent to pixel 7) would contain a certain percentage of light and if this was more than pixel 9 (now the first pixel on the new analysed row) an anomaly in the ESF would be seen as a spike in the curve. Once again, this is explained in greater depth in reference [40]; page 35.

A similar method for MTF measurements is used by C. Ponchut [41] where the sampling method is used to provide the LSF FWHM for an image of a thin slit at 3.4°.

Continuing on from figure 3.15 the output ADC is plotted against pixel number (which has been converted into millimeter distance); this is the ESF curve for the original fluoresced image. Figure 3.16 shows the plotted relationship. Numbered on the curved plot are the data points corresponding to the pixel numbers in figure 3.15. A more clearly defined knife-edge will lead to a steeper rise in the ESF. However, this should be expected because the more defined the knife-edge is; the better the modulation of the imaging device.

Once all the 9450 data points are plotted the ESF will eventually look like figure 3.17. Cross-talk between adjacent pixels and aliasing effects are the greatest cause for the noise in the curve, especially seen at higher levels of ADC, as there is more error in the illuminated pixels than the other only detecting dark current.

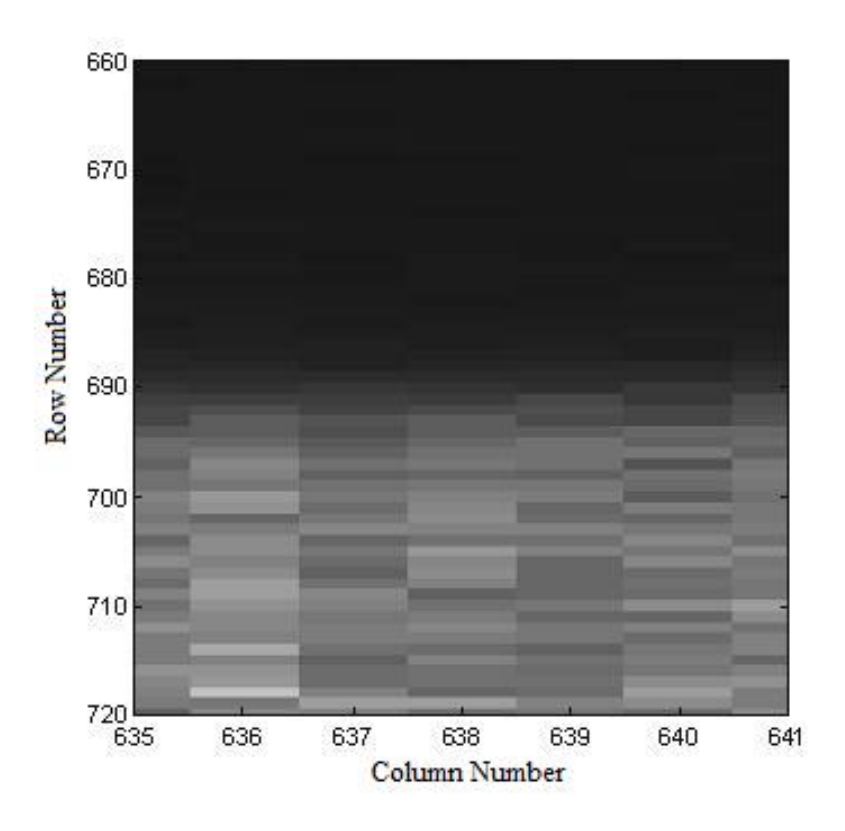


Figure 3.14: Zoomed in image of the knife-edge of the previous figure. Columns 635 to 641 were observed

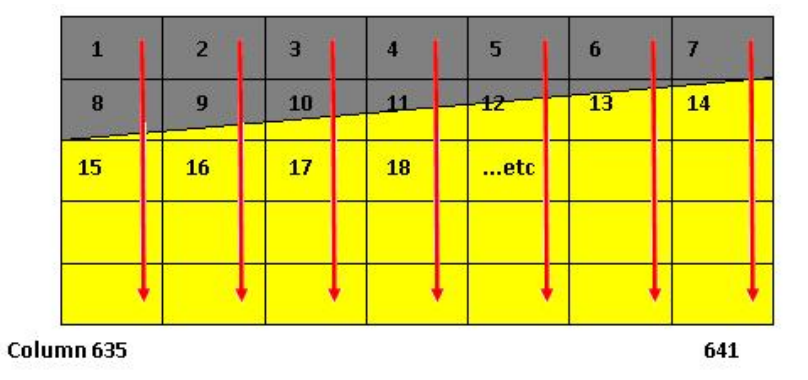


Figure 3.15: Sampling method of the seven columns analysed to obtain a good ${\it ESF}$

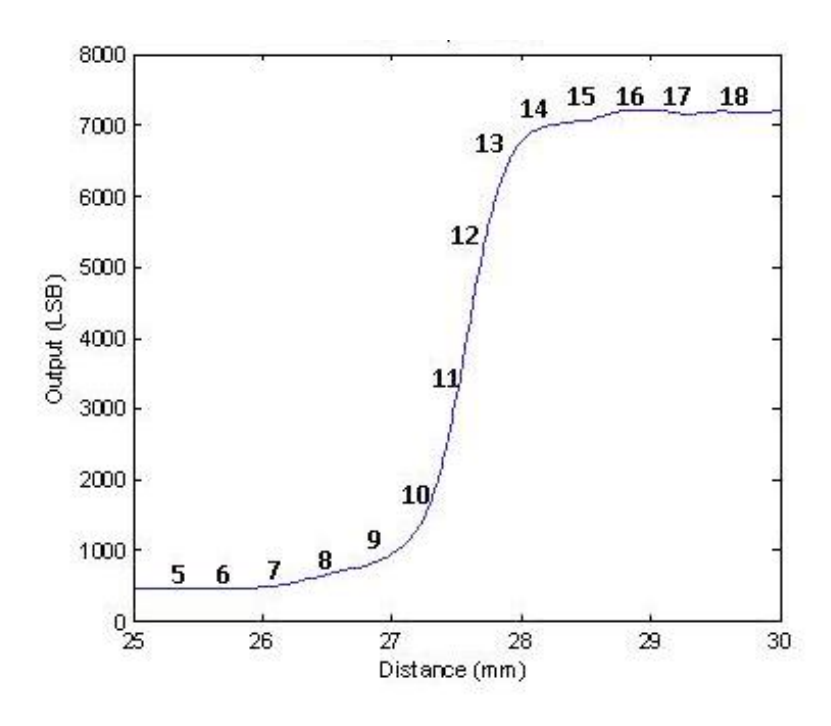


FIGURE 3.16: Preliminary calculation of the ESF curve with pixel numbers from the previous figure as an aid into understanding the sampling method described

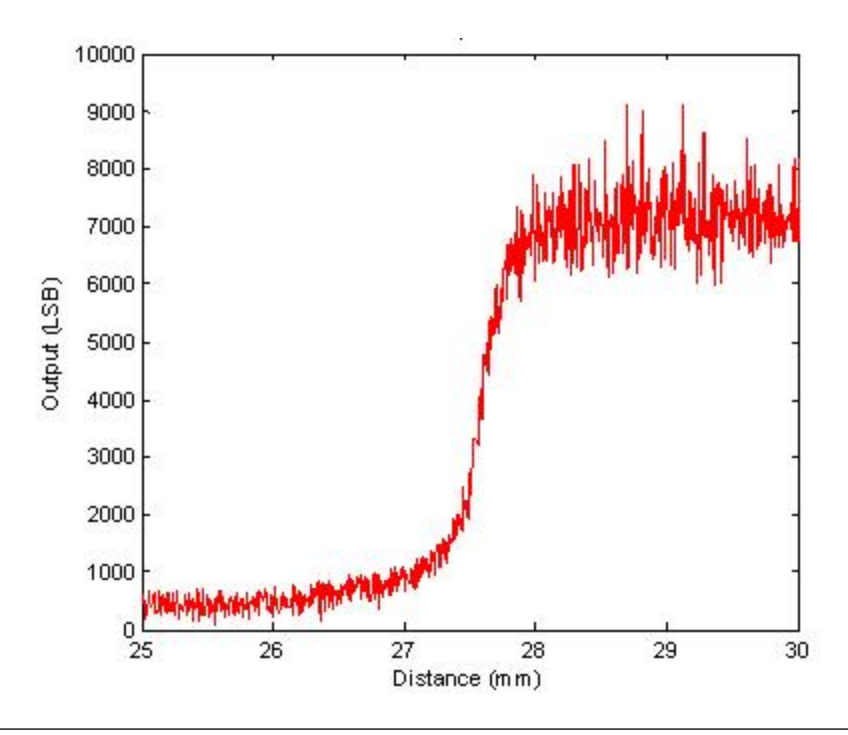


Figure 3.17: ESF curve once all data points have been accounted for, however this data requires smoothing as the noise levels are high

To reduce the effect of the noise on the final MTF result, the data in figure 3.17 is smoothed. This technique takes a series of 10 adjacent points (for example) on the curve, averages their values and plots one data point in its place. The number of points to be averaged however must be varied accordingly to the sharpness of the knife-edge; a more defined edge will require fewer data points to be averaged and hence smoothed. Figure 3.18 is a plot of the ESF curve once smoothing has been applied to it.

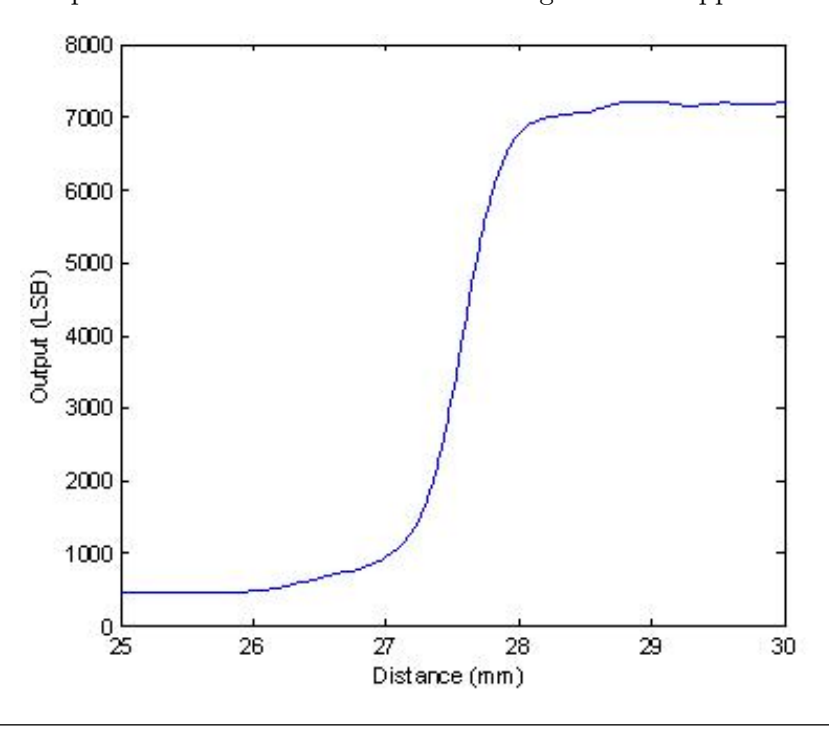


FIGURE 3.18: Smoothed ESF data using an iterative averaging technique

The smoothing for the data recorded in this investigation using either of the Hamamatsu plates required the average of 21 values of the original ESF data. A plot would result of the mean value of ESF(n) to ESF(n+21) as ESFsmooth(n). This was repeated. ESF(n+1) to ESF(n+22) as ESFsmooth(n+1) and iterated 20 times. The smoothed plot on each ESF and subsequently LSF curves have 400 values less than the data before smoothing since 20 data points (the first 10 and the last 10 values) are lost each time.

Figure 3.19 displays the LSF of the smoothed ESF normalised to the peak. The LSF is derived by differentiating the composite ESF. The FWHM in this example is approximately 0.52mm and because:

$$FWHM = 2\sqrt{2ln2} \cdot \sigma \tag{3.1}$$

the standard deviation σ for this example is equal to approximately 0.22mm. The final result of the fourier transformed LSF (the MTF curves) can be seen in the

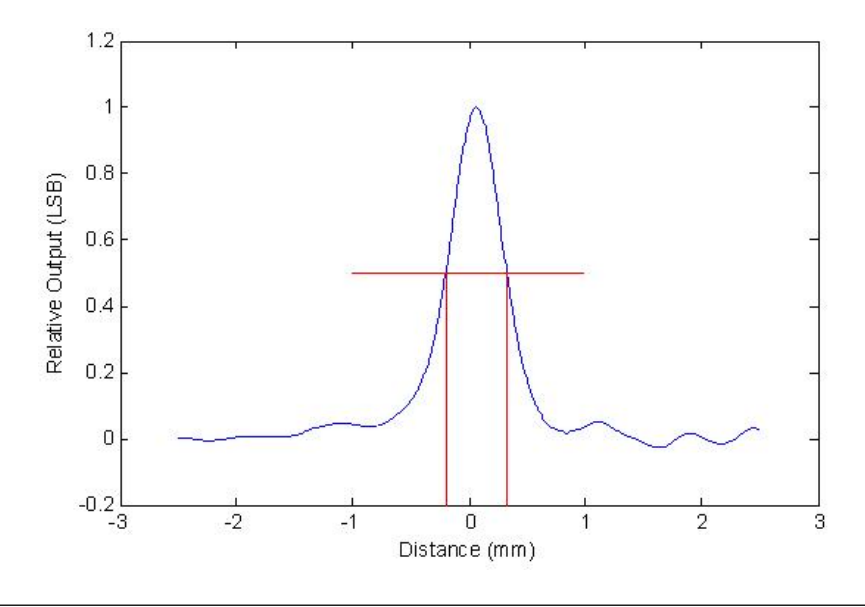


FIGURE 3.19: Normalised LSF curve; achieved by differentiating the ESF data

following chapter: Results. Operating tube voltage settings and frame rate settings on the OptoDAQ software were changed throughout procedures to give varied sets of data, so that the influences of the modified parameters could be observed.

3.7 MATLAB

MATLAB is a high level mathematical and technology programming language developed by The MathWorks. It is used often for plotting function, implementing algorithms and creating numerous user interfaces. Its use in this investigation is extremely wide and varied, producing the vast majority of the results from the raw data collected. All spatial resolution measurements will be analysed and assessed using specially written codes. Since this is high level programming, Go Ono (a placement student from the University of Bath) and Matt Wilson have aided in some of the programs written which will analyse some of the data throughout the course of the experiments carried out in this investigation.

There are two main programs written for this investigation so far, which are worth mentioning in this dissertation thesis. One of which creates the dark current pedestal file which is subtracted from the ".raw" files generated by the OptoDAQ software. Figure 3.20 shows the code for this program.

Its basic function is to take the raw file, process and average the data and then produce an output image in a grey colourmap format with square axis orientation. The clever part however is that it take this output image and formats the data into a text file which

FIGURE 3.20: MATLAB code for creating the raw pedestal data and files

is easier subtracted from another raw file as the dark pedestal than the grey colourmap image.

The second of the key programs which was written is much longer, and therefore can be seen in Appendix C. This is the code for calculation of the ESF, LSF and MTF of the raw data described in the previous section.

The Results chapter which follows will detail the findings (and to some extent the conclusions) of the raw data which was collected by means discussed in this chapter which has just been read.

Chapter 4

Results and Discussions

In this chapter of the dissertation the fundamental results both initially collected and obtained from further derivation and analysis of raw data are displayed. This is, needless to say, not all of the results collected throughout the years duration of the placement; only necessary data has been accounted for.

The format of this chapter will discuss the characterisation of the detector system and the sensors performance as an imaging device by means discussed in the previous two chapters. The effects of irradiation with $150\mu m$ and 1.5mm thick CsI(Tl) scintillators will be shown, which account for preliminary test ideas with low and high energy x-rays respectively associated with this investigation for an appropriate scintillator and imaging device for X-ray detection. Beamline test results have not been finalised however some imaging tests from an alternative X-ray set at the Diamond facility are displayed at the end of this chapter.

Test samples of scintillators acquired from Hilger Crystals will go on to be laser engraved, providing one solution to the task of production of a structured scintillator. This future work will be carried out as a means of testing even higher energy x-rays (than permitted with the 1.5mm thick CsI(Tl)) without damage to the sensor. There are also future plans to fill the laser cut fissures in the trial scintillation material which may increase light output. Additional beamline tests are inevitable to hopefully aim to characterise the detector system and any improved modifications along with new materials both structured and columnar in design.

4.1 Initial Testing and Preliminary Characterisation of LAS

Before testing and characterisation can be carried out on any scintillators some basic characterisations of LAS need to be observed and recorded. This section displays the results from dark images, any defects which were observed on first use with LAS as an operational sensor, normal light incident upon the LAS surface and any temperature response.

4.1.1 Dark Pedestal Image

Each pixel on any imaging sensor has a noise edge and a unique channel, of which each has a slightly different gain. The noise edge is the level that the voltage 'sits' on. By taking a completely dark (or as dark as possible using convenient methods such as placing the detector in a 'dark box' or covering it with a 'dark cloth') image it is possible to reduce the noise in the system so that all pixels 'sit' on the same voltage, on average. Once the dark image has been subtracted from the raw image, it is said to have been dark pedestal subtracted. Using the two different wafers of W2-2 and W3-3, a dark pedestal image could be obtained from each; as seen in figure 4.1.

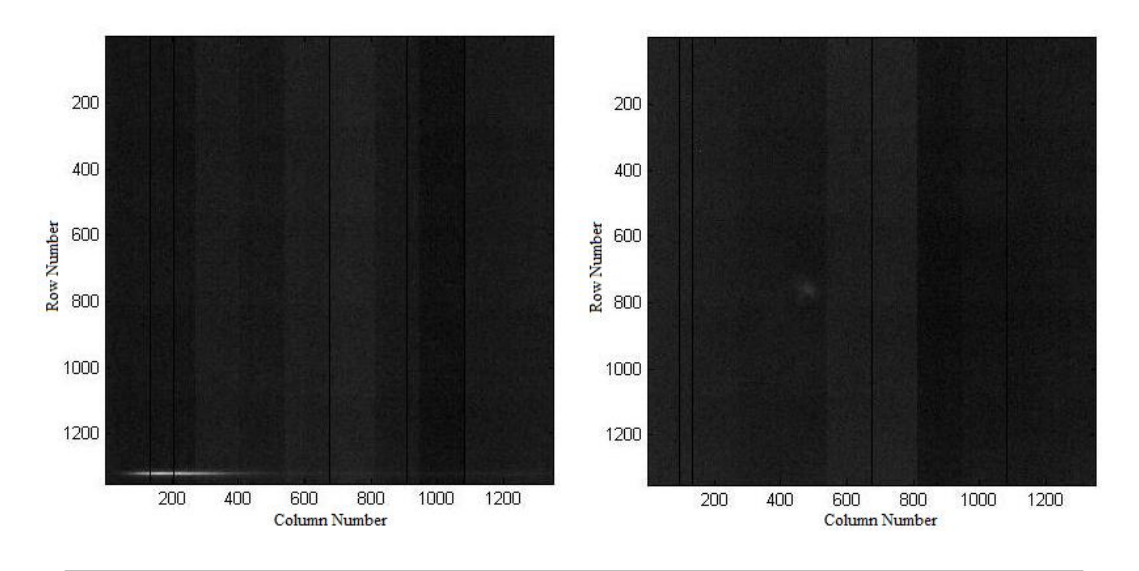


Figure 4.1: Two separate frames from a collection of 100 frames in one image for two different LAS wafers; W2-2 (left) and W3-3 (right)

Both images in figure 4.1 show one frame out of 100 taken from one image. Theoretically an unlimited number of frames can be recorded in one image using the OptoDAQ software, provided there is enough memory on the hard disk drive (HDD) the images are being written to. The more frames an image is composed of however, the longer it will take to record the data; this also depends on frame rate of the system. It is important to

understand that a dark pedestal subtraction should be taken with each change in sensor or OptoDAQ settings, as this will alter the pixel's noise edge.

Similarly, as a means of correcting the different gains on each channel per pixel, a completely saturated image is taken and is also subtracted from the raw data. The image is now said to be flat field corrected. To prevent mathematically calculating negative values of LSB on any further data, both dark pedestal and flat field correction data needs to be applied to the raw image in the following way:

$$CorrectedImage = FlatFieldCorrection - (RawImage - DarkPedestal)$$
 (4.1)

This method has been applied to all results (unless stated otherwise) in the following sections of this chapter; figures of this can be seen later on.

4.1.2 Columns of Readout Error

Noticeable on both wafers in figure 4.1 are whole columns of what appears to be dead pixels. These are in fact columns of read-out error, which are due to a yield error or broken connections in the reticle. Dust on the sensor during fabrication may also be a plausible cause. Using MATLAB to profile along one row, these read-out errors are more clearly defined when the LSB (or ADC) values are plotted; figure 4.2.

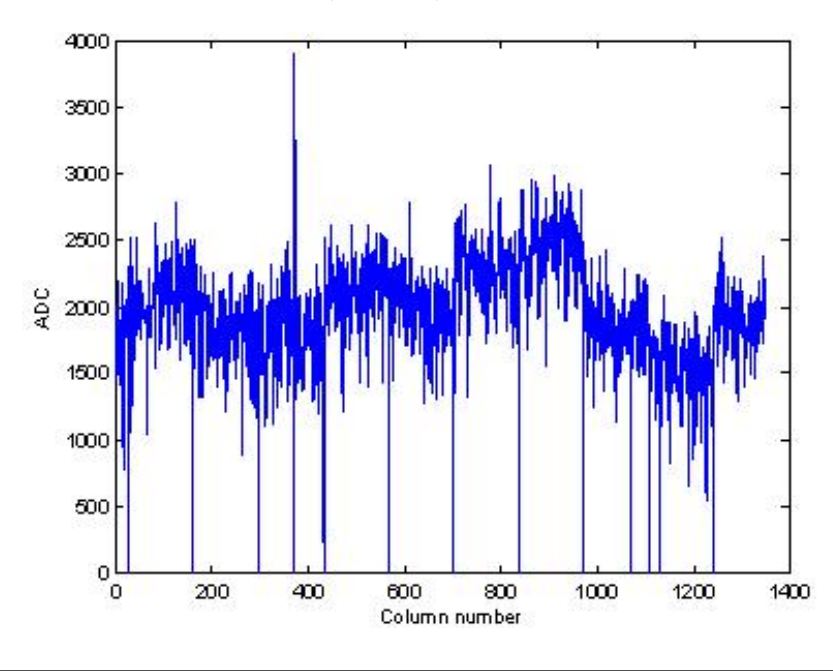


Figure 4.2: An ADC value versus column number plot profiling along row 500 of a dark pedestal image

Those defects at column numbers 680, 700 and 820 are more likely to be due to dead

columns where the reticles are stitched together, hence they are stitching errors not read-out errors. Two of the three negative spikes around the 1100 column number however are the read-out errors (the other spike represents the stitching error again). The profile in figure 4.2 is for one frame. The columns of read-out error appear to 'move' when two different frames within the same image are viewed; as shown in figure 4.3. On the left: frame 81; on the right: frame 82.

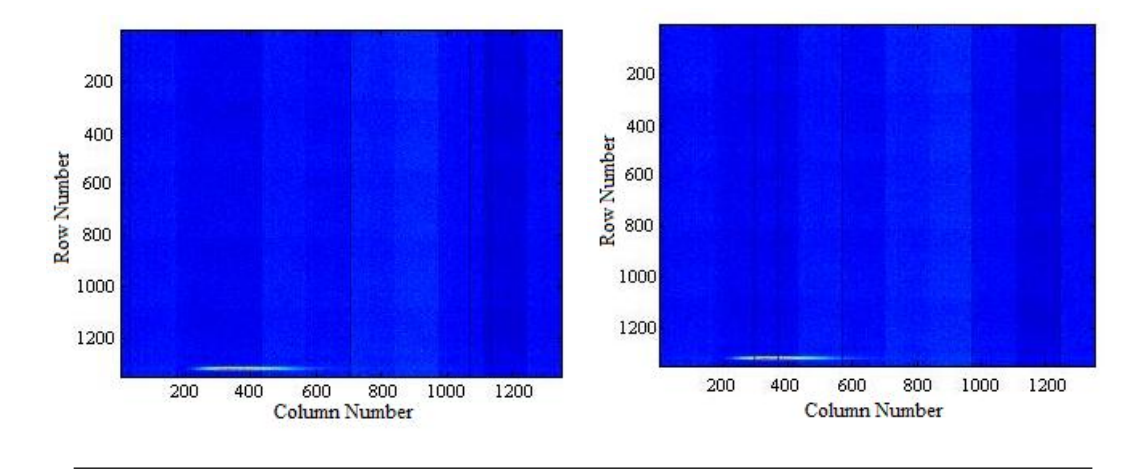


FIGURE 4.3: Frame 81 and 82 respectively from one dark pedestal image consisting of 100 frames of data

The stitching defects are apparent because of errors in column control logic where by the shift registers in each reticle are not joined correctly. It is merely a design fault and is solved by breaking the connection between adjacent pixels and implanting a new control logic whose input is grounded rather than joined to another pixel. There are two quicker solutions however to minimising stitching and read-out errors from the raw image without altering any electronics. Using MATLAB it can be incorporated into the code to simply make each column of read-out error have the same values of LSB as its neighbour. I.e. pixel (135,500) will be a duplicate of pixel (134,500), pixel (135,800) will be a duplicate of (134,800) and so on for all 1350 pixels. The second method is to simply average the plot for all 100 frames in the image along the same row resulting in an average profile of figure 4.4.

4.1.3 Mask Testing with Polychromatic Light

By masking a section of the sensor using the carbon-fibre mask constructed from the workshop; figure 4.5, it is possible to look at the ESF produced from the difference in the contrast of polychromatic light onto the sensor's surface. By following the method explained in the MTF procedure in the Experimental Arrangement chapter, using a well

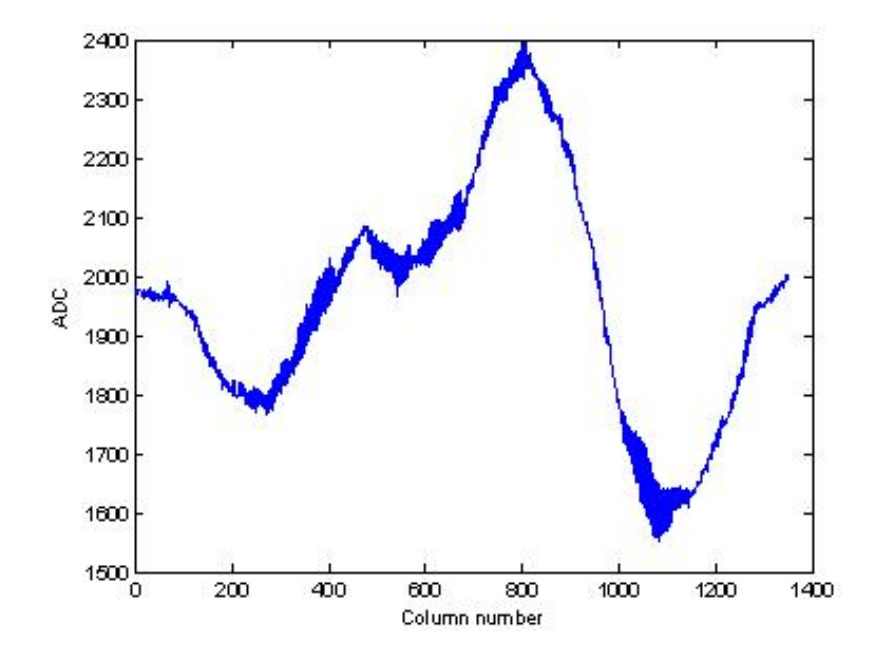


FIGURE 4.4: Correction of read-out errors by averaging data over 100 frames. Variation in ADC values from 1550 to 2400 are because of varied pixel gain and noise edge. Pedestal subtraction should reduce the ADC difference

defined knife edge, it is theoretically possible to obtain the MTF for the sensor in this way (this would be for LAS alone however, as without any scintillator mounted it is not an APFPI).

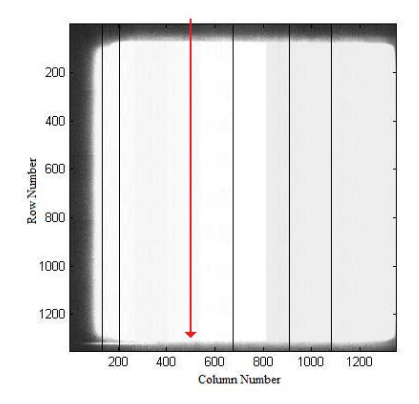


FIGURE 4.5: Polychromatic light incident upon the surface of LAS with the carbonfibre mask fitted, so that it rests securely on the bonding wire protective coating. The dark edges around the image is a shadow effect from the mask

The mask can only be placed so close to the sensor as it is not favourable to allow anything to physically touch the surface of LAS (this is inevitable though when the scintillator is placed onto the APS). The mask rests on what is called the 'Glob-Top' of the sensor. This is a protective coating engulfing the connecting wires of LAS to it's printed circuit board (PCB). The 'Glob-Top' is elevated above the sensor surface by approximately 1.0±0.1mm. Profiling down column 500 of figure 4.5 (as marked in red)

the ESF is determined; figure 4.6.

It is only desirable to analyse the boundary between the extremes in the contrast difference. Figure 4.6 is therefore observed over approximately 85 rows (3.4mm).

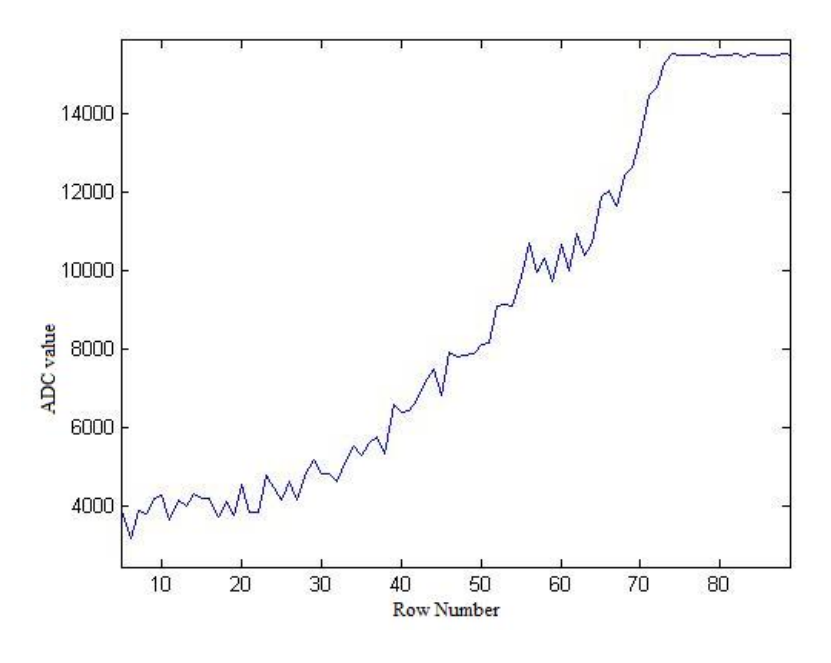


Figure 4.6: ADC versus row number analysed down column 500 from the previous masked polychromatic light image

With a rough rise in the ESF differentiation to produce the LSF would not be practical as a poor MTF would result. Smoothing could be applied to the image as explained in the "Experimental Arrangement" section, however the mask is not inclined at a desirable enough angle for the MTF to be calculated. The rise is also not steep enough therefore producing a greater FWHM in the LSF.

4.1.4 Temperature Dependance on Signal Output

When the OptoDAQ and hence LAS are turned on, the electronics in the hardware uses power which dissipates as heat. The power consumption of LAS has not been measured and perhaps something to consider with future investigation, however the instantaneous electrical power delivered to the sensor is approximately 20 Watts. It has been discovered that one needs to wait until the temperature of the sensor reaches the point at which the environment can remove the same amount of energy as is being generated; an equilibrium. Taking this effect into consideration, the temperature difference of the sensor was recorded over a period of one hour. This was possible by using a Lakeshore 332 Temperature Controller with a standard temperature sensor loosely fastened to the underside of the LAS wafer. Figure 4.7 displays the results in a graphical form.

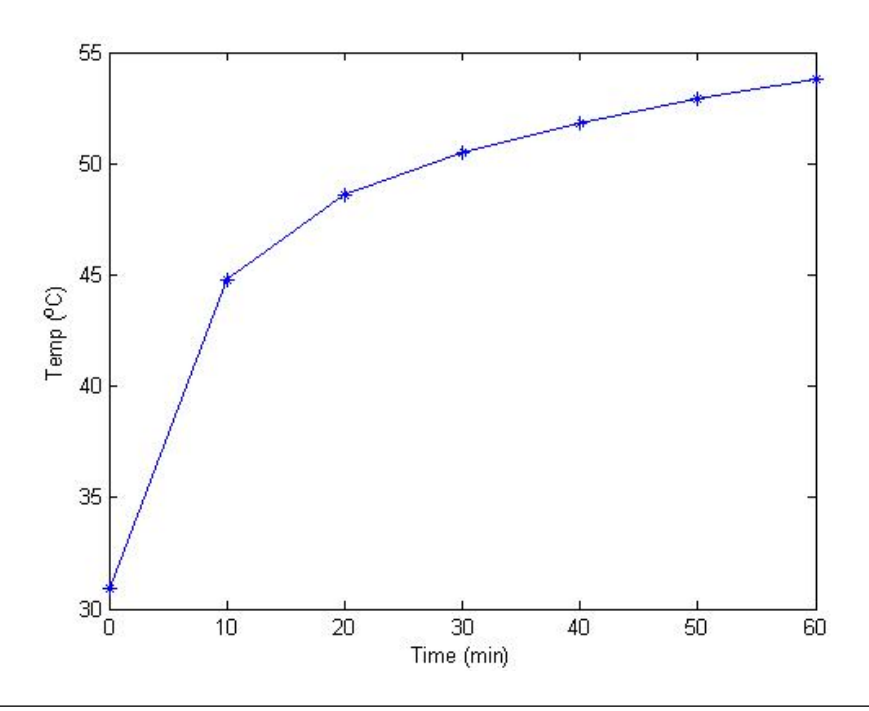


FIGURE 4.7: A temperature versus time plot over a one hour period to monitor the temperature response of the LAS wafer

Reaching such a high temperature of roughly 53°C (326K) and evidentally still rising beyond the hour the data was recorded for, temperature stability would certainly be a key importance when recording further data. Temperature stability is important as many performance parameters are proportional to temperature such as dark current (which doubles every 7 degrees) and reset noise (which is equal to kTC; where k is the Boltzmann constant, T is temperature and C is the charge applied).

As dark current is reported to be affected by temperature response the energy in units of LSB was studied over the same hour period from which figure 4.7's results are obtained from. Dark current as has been previously discussed throughout this report is an important parameter of the signal output from the detector. Figure 4.8 displays the seven, 10 minute interval readings as in figure 4.7, of energy (a.k.a ADC) (which correspond to different temperatures) and the number of events instantaneously recorded (N(E)). The data was recorded and plotted in such a way that one hundred frames of data were recorded and averaged, then subtracted from one frame in that same file. This enables a zero value for the energy along the x-axis. Due to the integration time of 9.8 fps and the abundance of pixels on the wafer (1350x1350) a large number of events are recorded for the dark current at an instantaneous moment. Considering human error as a limiting factor, the first instantaneous measurement is taken when the LAS system is started. There appears to be no or little increase in energy. It can be seen from figure 4.8 though, that as time and subsequently temperature is increased the energy begins to raise up to 200 LSB above the normalised count due to the subtraction of 100 frames of dark current

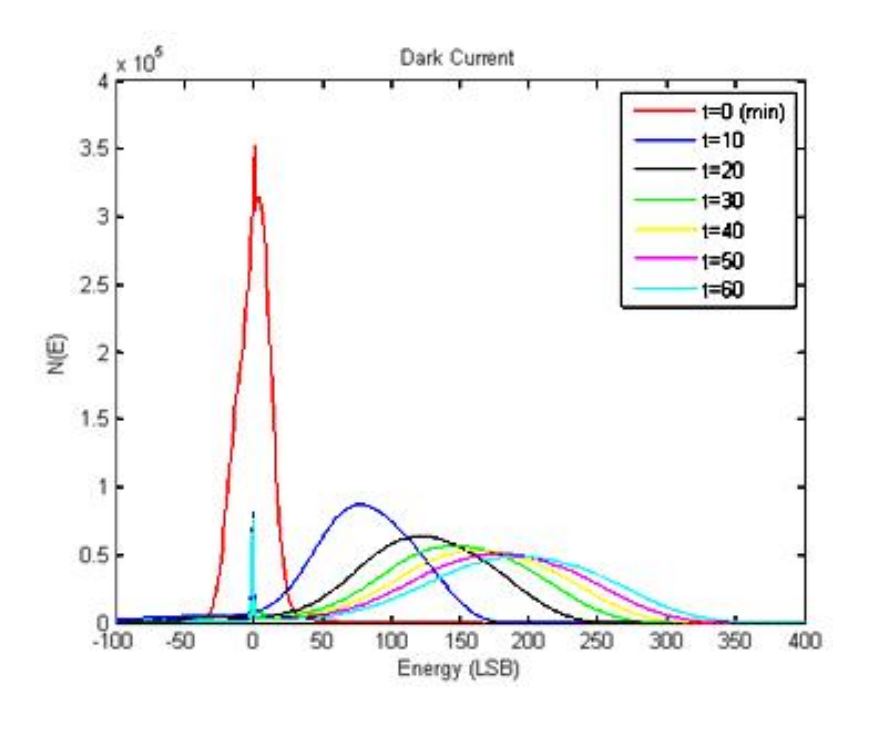


FIGURE 4.8: The number of events of dark current detection as a function of time

data. The integral of each data curve however (the total area under the plot) remains constant. The FWHM of each curve increases with time (or temperature) because the reset noise in each pixel is affected by temperature. The spikes on the negative LSB side of each peak are due to a row or column read out error and can be corrected by widening the bin width of the histogram.

The results from figure 4.8 were obtained with the LAS stack placed in a sealed box so that temperature detection would not be influenced by loss of heat from the system to the ambient surroundings. This was more important though when a fan was introduced into the box which cooled LAS using a standard laboratory coolant pumped by a Grant R20828003 Coolant Holder and Grant GD120 pump from Cambridge Ltd. The exact procedure was carried out as before, with the data generated by averaging a hundred frames of dark data and subtracting this from one frame in that same file. Figure 4.9 displays the results.

Dark current data is unstable with temperature, however it is possible to reach equilibrium very quickly when the operating system is cooled thus determining a threshold noise. Although FWHM differs from peak to peak in figure 4.9, a threshold value of roughly 100 LSB can be predicted. Therefore when cooled in future experiments, the data recorded will have a threshold noise error of 100 LSB. Temperature stabilised around 24.2±0.5°C. The error here is from absolute and relative error analysis associated with the temperature controller, the temperature reading on the coolant pump and human oversight.

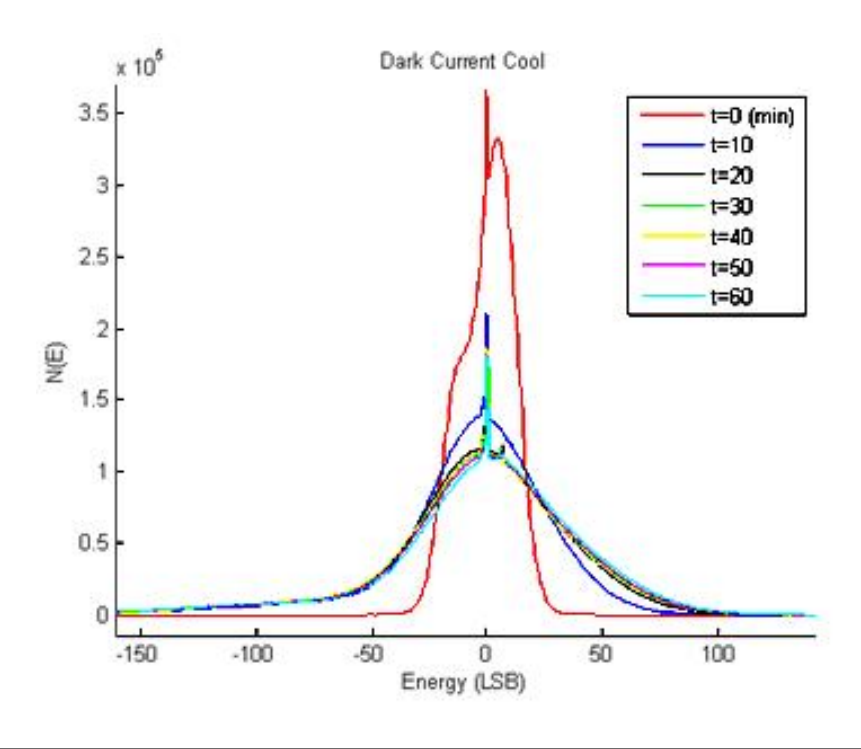


FIGURE 4.9: The graph layout is displayed as the previous figure, except the system has been cooled in this instance

In order to be able to monitor temperature response and fluctuations throughout periods of data collection or even basic operation of LAS, a temperature sensor would need to be engineered into the LAS stack or even mounted onto the wafer itself. This would require a sufficient amount of re-designing the stack and software up-grades as indicated by Andy T. Clark, the initial designer of the sensor. Success of this project with LAS and the APFPI could certainly be cause alone for such a structure change to the LAS electronic engineering, proving useful to further testing and characterisation, as levels of LSB have been shown to vary significantly with temperature variation.

4.2 Scintillators and Characterisation of the APFPI

With preliminary characterisation having been carried out on LAS and its operating system, key results can start being taken: the characterisation of the active-pixel flat panel imager (APFPI). In the previous chapters it has been clarified that the APFPI is the name given to the combined system of the scintillator and the detector. Before results can be collected and analysed in this way many different scintillators had to be researched in order to find the most suitable.

This following subsections outline the key points that were experienced throughout the

duration of the investigation. The research into suitable scintillator materials is discussed followed by the results from the first stopping power experiments. The effect of fluorescence from a test scintillator is then studied, with the intention to get the best results possible for light detection. Some more test scintillators are then studied courtesy of Hilger Crystals Inc. again focusing on their relative stopping power of X-ray radiation and light output. The important results however are displayed when the scintillator plates from Hamamatsu Photonics are tested. Stopping power, light output and the first set of modulation transfer function calculations are discussed when researching with these products.

4.2.1 Researched Scintillators

When research began on this project the most fundamental area to be investigated was the scintillator material which would be mounted onto the MAPS device. To meet criteria such as ample stopping power, good light output and low afterglow, it would be essential that the correct material was used. To begin with the optical and physical properties of various different materials were researched. Table 4.1 details in depth the characteristics of interest of many common and easy to obtain scintillator materials. The more widely used compounds have only been researched, as more obscure scintillators from the glasses or plastics range are not likely to be readily available in the quantity required for this investigation. Such examples would be boron silicates or a polystyrene solvent.

The properties listed in table 4.1 were collected over a couple of months, as new ideas such as varied percentages of attenuation at different energies became necessary throughout the progress of the investigation.

Tables 4.1 and 4.2 are combined, with the latter including additional comments noted about each material and the reference of such comments if necessary.

For the complete names of each material, please see the abbreviations page at the beginning of this report. The data was originally research in mid May, with Cadmium Tungstate (CdWO₄), Lead Tungstate (PbWO₄) and Double Natrium-Bismuth Tungstate (NBWO) added a few days after. Other materials such as Gadolinium Oxide (GadOx) and Zinc Selenide (ZnSe(Tl)) followed. The hardness parameter was introduced much later, in mid June, when the idea of a structured scintillator was discussed. The hardness would be of importance then as the idea of laser cutting techniques could be applied to a scintillator to give it a structured appearance.

Density, decay time and light yield were the initial important parameters which needed to be studied from the table. A material with a high density would imply a small attenuation length of x-rays (a greater stopping power). To check this theory the 50%

															,			
Light	Yield	$(\mathrm{ph/keV})$	32	20	26	6	90.0	14	0.5	22	54	49	63	10	41	38	49	80
50% Attenuation	Length	$(\mathrm{mm}) \ @ \ 662\mathrm{keV}$	11.0	14.2	90.6	10.0	Unknown	10.0	Unknown	16.0	20.0	23.0	18.0	11.8	20.0	25.0	11.2	Unknown
Decay	Time	(ns)	41	09	20	300	4	14000	20	300000	1000	28	16	20	630	230	28	2000
Hygro-	scopic		No	No	No	No	No	No	No	Slightly	Slightly	Yes	Yes	Yes	Yes	Yes	Yes	Yes
Peak λ	for light	o/p (nm)	420	425	430	480	495	540	540	440	530	350	380	380	410	415	420	610
Density	(g/cc)		7.10	6.71	4.54	7.13	8.28	7.9	7.57	7.1	4.51	3.85	5.08	8.35	4.51	3.67	7.35	5.42
Material			LYSO(Ce) (Prelude 420; Saint Gobain)	GSO(ce)	YSO(Yb) or (Pr)	BGO(V) or (Pr) or (P)	$PbWO_4$	$CdWO_4$	NBWO	GadOx	CsI(Tl)	$LaCl_3(Ce)$	$LaBr_3(Ce)$	LuAP(Ce)	CsI(Na)	NaI(T1)	LSO(Yb) or (Pr)	$\operatorname{ZnSe}(\operatorname{Te})$

TABLE 4.1: A concise summary of the useful criteria required to aid in choosing a suitable scintillator material to carry out testing upon

Material	Additional Comments / References
LYSO(Ce) (Prelude 420; Saint Gobain)	Fast and dense, background from ¹ 76Lu activity
GSO(ce)	High stopping power, lower light yield than LSO
ASO(Yb)	LSO and YSO properties obtained using optical gel [42]
BGO(V) or (Pr) or (P)	Compact detector with low afterglow
$PbWO_4$	High Z likely to have excellent stopping power
CdWO_4	Low afterglow, commonly used with photodiodes
NBWO	New scintillator, seldom tested. Able to emit Cerenkov radiation
GadOx	Most properties gathered from reference [43]
$\operatorname{CsI}(\operatorname{Tl})$	Rugged and a good match to photodiodes. 550μ m thickness gives 80% X-ray absorption at 60keV
$LaCl_3(Ce)$	General purpose scintillator, good energy resolution
$LaBr_3(Ce)$	General purpose again, one of the best energy resolutions
LuAP(Ce)	53% of decay is 20ns, remainder is 180ns [44]
CsI(Na)	Commonly tested scintillator in R and D
NaI(TI)	General purpose, good energy resolution
LSO(Yb) or (Pr)	The original LYSO before addition of Yttrium and becoming patented
$\operatorname{ZnSe}(\operatorname{Te})$	Multicrystal, rarely tested

TABLE 4.2: Additional comments for each material, perhaps required in choosing a suitable scintillator

attenuation length at 662keV column was written, having used XCOM once again to obtain the data [20]. 662keV is used as it is the dominant scattered photon energy from Compton scattering. The table clearly shows that a lower attenuation length corresponds to a higher density or vice versa. This is good as one of the key parameters in the search for a suitable scintillation material is for it to have a high stopping power. This must be combined with the effect of a fast decay time (to limit after glow) and a high light yield. From the tables; LYSO, BGO, PbWO₄ and CdWO₄ fit the desired criteria. Although CsI(Tl) is theoretically not as superior as the other materials, this will also be tested. This is because cost and fabrication size is also a limiting factor to what material can be used, recall the size of LAS is 54mmx54mm, any material mounted onto LAS will need to be roughly this size.

4.2.2 Amorphous GadOx and Stopping Power

A high stopping power is essential to this investigation and also to the safety of the CMOS sensor and it's chip-on-board electronics. Preliminary testing of this was carried out on the researched material; Gadolinium Oxide. The scintillator was being used insolution by the Nano-particle division at RAL. If the results from this were acceptable, GadOx would certainly be another material worth considering for the investigation. Adnan Malik from RAL supplied the investigation with four quartz slides. One of which was plain, the others had 50ml, 100ml and 150ml of GadOx in solution upon them. Using the method previously explained with the silicon pin detector (see the section titled "The Silicon Pin Detector" in the Experimental Arrangement chapter of this report), stopping power measurements were taken with each of the four quartz slides.

As explained in the Experimental Arrangement chapter of this report (chapter ??, the current on the Keithley Picoameter was noted as the operating tube voltage of the Seifert RP149 X-ray machine was increased to a maximum of 50kV. The tube current was held constant at 30mA. A plot of this data is displayed in figure 4.10. With an error of 10% on the Keithley (as indicated in the user manual) it is clear that the results for the four quartz substrates lie within each others error range. Once the tube voltage reaches its maximum however, the data separates more; hence there is some stopping power differential between the different volumes of amorphous GadOx on each substrate: 150ml of solution enables the lowest picoameter current.

Although the amorphous GadOx is making a difference to the dose rate received by the silicon pin detector, it is not stopping the X-rays enough to be used as a trial material with LAS. This is especially important as the dose rate is dependant upon the thickness of the layer being irradiated. The silicon pin is 263μ m thick, whereas the epitaxial layer in LAS (where any radiation damage in a CMOS device will occur) is much thinner; in

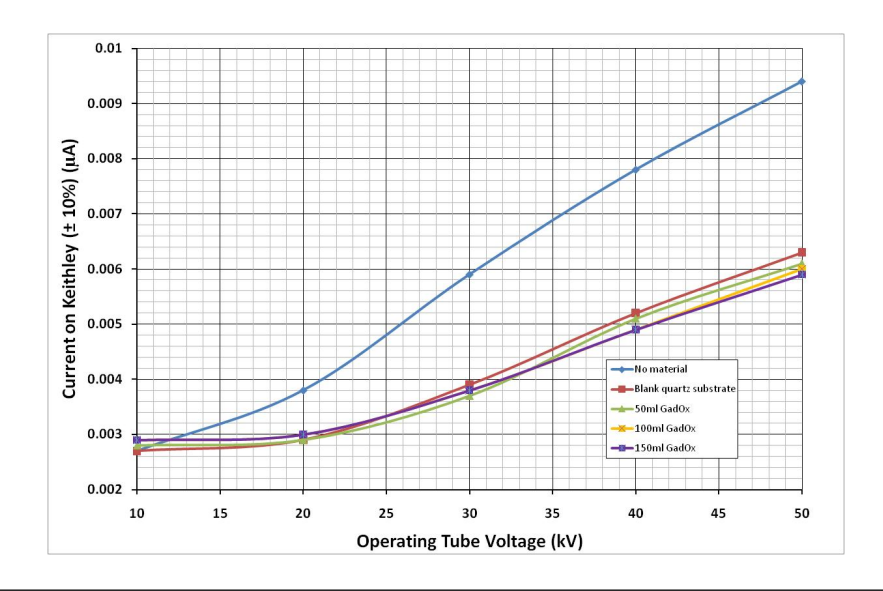


FIGURE 4.10: Stopping power tests for four different amorphous GadOx solutions on quartz substrate. The current profile for no material covering the silicon detector is also plotted. All stopping power plots are produced in Microsoft Excel

the order of 10's of μ m's. Therefore the dose rate will be higher in LAS than for the silicon pin detector. To conclude, the investigation will require a material which stops all 50kV X-rays as any detected by the silicon pin will have a worse effect on LAS. Using XCOM once again it is possible to determine the percentage of X-rays passing through the GadOx and quartz substrate. Taking,

$$\frac{I}{I_o} = e^{-\mu t} \tag{4.2}$$

(where μ is the linear attenuation coefficient of the material in question and t is the thickness of it) it is possible to calculate the percentage required. XCOM gives the following results for GadOx (Gd₂O₃):

m Energy(MeV)	Total Attenuation(cm ² /g)
1.00E-02	1.11E+02
2.00E-02	1.80E+01
3.00E-02	6.16E+00
4.00E-02	2.92E+00
5.00E-02	1.67E+00

Table 4.3: The results as given by XCOM for the total attenuation of GadOx for five energies

To make the exponential of equation 4.2 dimensionless each total attenuation value in table 4.3 must be multiplied by the density of GadOx: 7.41gcm^{-3} . The thickness of each amorphous solution of GadOx had to be measured using the Zeiss SteREO Discovery V8 microscope. Conveniently this was found to be $100\mu\text{m}$, $200\mu\text{m}$ and $300\mu\text{m}$ for each

of the 50ml, 100ml and 150ml solutions respectively. Therefore for the 50ml solution at $50 \mathrm{kV}$:

$$\frac{I}{I_o} = e^{-12.37cm^{-1} \cdot 100\mu m} \tag{4.3}$$

$$\frac{I}{I_o} = 0.884$$
 (4.4)

Which implies 88.4% of the original intensity of the beam passes through 50ml of GadOx. Following this procedure through exactly for quartz, and knowing that the substrates were 500μ m thick, the combined results indicate $85.1\pm4.1\%$ of the original intensity and energy of the x-rays passes through the 50ml GadOx coupled to the substrate. The error in this result of approximately 5% originates from the error in XCOM and the determination of the solution thickness with the stereomicroscope.

Recall, this is the percentage of X-rays passing through the materials covering the silicon pin detector, it is not the percentage being detected. This is due to scattering off the surface of the detector or absorption within the silicon or even the probability that an X-ray will traverse through the detector itself.

Figure 4.11 is a photograph of the 100ml amorphous GadOx. Note how moisture has collected under the GadOx and caused the amorphous material to crack. When testing was carried out on these substrates the collimator on the X-ray set was positioned directly above that material which had not cracked.

As a conclusion, it should be noted that although the stopping power of the chosen scintillators to investigate with is crucial, it is merely an observational result rather than a numerical one. As seen above however, this could be calculated with XCOM given the time.

4.2.3 Scintillator samples courtesy of Hilger Crystals

The measurements on GadOx were used to develop the technique used to access the relative stopping power of different scintillators. Having chosen suitable materials for testing from table 4.1, samples were ordered from Hilger Crystals Ltd. These were BGO, LYSO, CdWO₄ and ZnWO₄.

Using the same method as before, the stopping power of these samples were tested to see what tube voltage would be suitable to use in further experiments with the materials. Figure 4.12 displays the results obtained.

As can be seen in comparison to the data for no material present (covering the silicon pin



FIGURE 4.11: 100ml Amorphous GadOx solution on a quartz substrate. Sufficient cracking can be seen due to moisture retention between the quartz and the GadOx

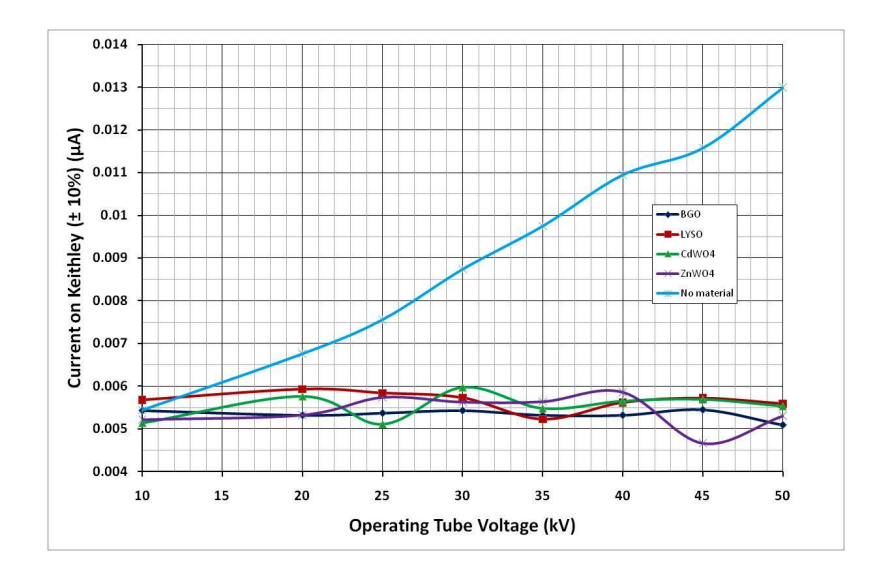


Figure 4.12: Stopping power plot for the four materials purchased as samples from Hilger Crystals. Tube current was held constant at $30\mathrm{mA}$ for all materials

detector), all the samples possess sufficient stopping power to stop up to 50kV X-rays. This is taking into account the error assigned to the Keithley picoameter however, as data seems to be slightly erroneous in some places. The main factor however is that both 10kV and 50kV data points for all materials produce the same current reading within the 10% discrepancy range.

The four materials could then be tested for light output, with tube settings not to exceed 50kV. As a scintillator was now being mounted to the detector, an optical grease was used as a coupling gel between the scintillator and LAS. This would act as a loose adhesive but more importantly; as an aid in transmission of photons once they had been generated in the scintillation material to the surface of the detector. A $300\mu m$ collimator was used on the X-ray set which was positioned at a height directly above the sample material, almost in contact (by a millimetre on human judgement). With the OptoDAQ software of LAS set to run at a mid-range 9.80 fps, images were collected of the luminescence spot from the collimated x-rays. Analysing the data was best done in ImageJ, a multi-formatting piece of imaging software, due to the uncommon format of the frames in each image captured by the OptoDAQ software. These were ".raw" files. Results of the analysis of the more concentrated and higher ADC values on the image (i.e. the collimated spot from the fluorescence of X-rays in the scintillator material detected by LAS) can be seen in figure 4.13. The values of average ADC in the figure represent the signal intensity, as it is the energy of fluorescence which is being measured.

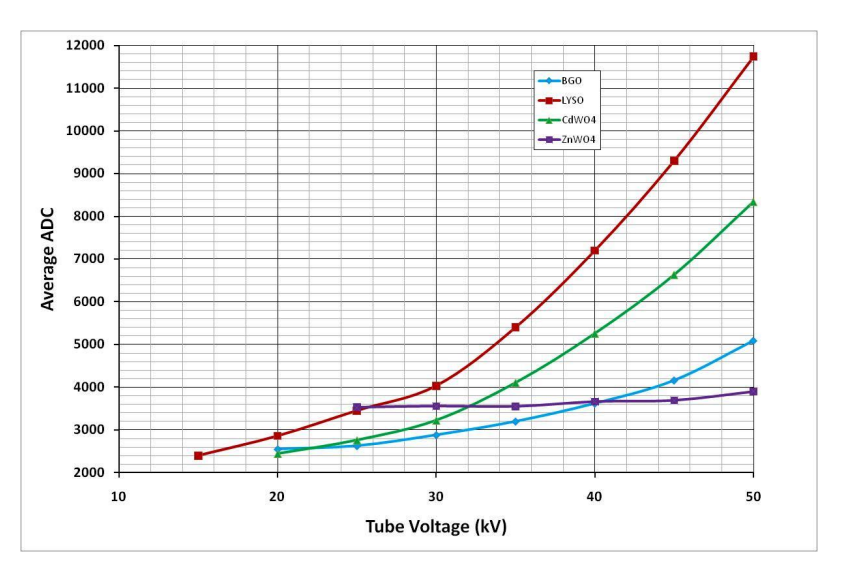


Figure 4.13: Highlighting the area of fluorescence from the collimated X-rays, the ADC levels (signal intensity in this case) are measured and recorded

With tube voltage increased in increments of 5kV, the results are more recognisably varied. The samples are made up of varying thicknesses of their constituent material. Therefore figure 4.13 arguably displays unfair data. I.e. ZnWO₄ does not appear to produce a very high light yield however it is 3.5mm thick compared to say 1mm of LYSO

or CdWO₄. Hilger Crystals claim that ZnWO₄ has as high a light output as BGO (if not slightly higher), yet at a tube voltage of 50kV fluorescence from BGO produces ADC values of over 1000 more than ZnWO₄. Due to the minimal gradient of the Zinc Tungstate curve, it can be assumed that ADC saturation occurs at approximately 25kV for this material. This is not too surprising due to the low yield apparently characteristic of this material. At 1.4mm thick LYSO is not the thinnest of the samples, however due to having the highest light yield (32,000 photons/MeV) by more than double CdWO₄, it produces the highest ADC values per operating kV. LYSO clearly produces the best results (both experimentally and theoretically as seen in table 4.1) and so is the material which should be considered as being purchased on a larger scale, in order to cover the effective area of LAS. The samples tested here are only a few square millimetres in surface area and 1mm deep. This is insufficient for measurements which need to be taken in order to obtain the Modulation Transfer Function of the combined APFPI. This is because none of the sample materials have a large enough area for a knife-edge to be obtained from. The main problem in using LYSO on a bigger scale is the cost. It is a patented scintillator owned by Hitachi, and therefore extremely expensive to get 50mmx50mm area samples.

Figure 4.14 is a colourmap image generated in MATLAB, from the original ".raw" file taken by the OptoDAQ software. It shows the BGO sample. The main circular pattern centering at approximately (1040,730) is the fluorescence pattern from the collimated X-rays. This sample has been subjected to enough stress to overcome its elastic properties and has resultantly fractured (indicated by the bright curved line just above the collimated spot). Higher levels of ADC are apparent at the crack and more noticeably around the edge of the sample, not because of fluorescence from the scintillator, but rather total internal reflection from within the material.

It is possible to use this image to crudely assign a result to the spatial resolution of the system. It has already been discussed that it is not possible to obtain a knife-edge image using the $100\mu m$ or $300\mu m$ collimator. Both of these simply produce too narrow a beam to stop a portion of the X-rays using lead or any other high stopping power material. The wider steel collimator of ~1cm in diameter cannot be used either as the samples from Hilger Crystals are not large enough and so X-ray radiation would be incident directly upon the surface of LAS. The only possible way of characterising this parameter is to use a MATLAB code to determine the width of each collimated image. The code is designed to take the column where the suspected widest part of the circular pattern is and plot the ADC against row number, where each row contains 1350 pixels (the array of LAS). In the case of figure 4.14, column 1040 is analysed. The results are seen in the line-scan; figure 4.15.

Taking into account the error in human judgement the area of interest is between rows 700 to 757 (as indicated by the red markers on the figure), as this represents the region

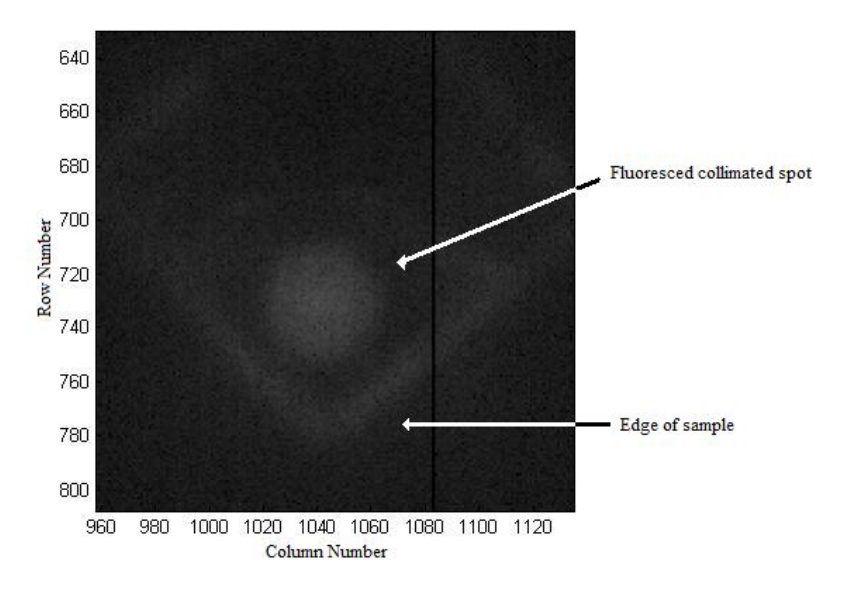


Figure 4.14: OptoDAQ data for a 300 $\mu \rm m$ collimated spot fluoresced from the BGO sample

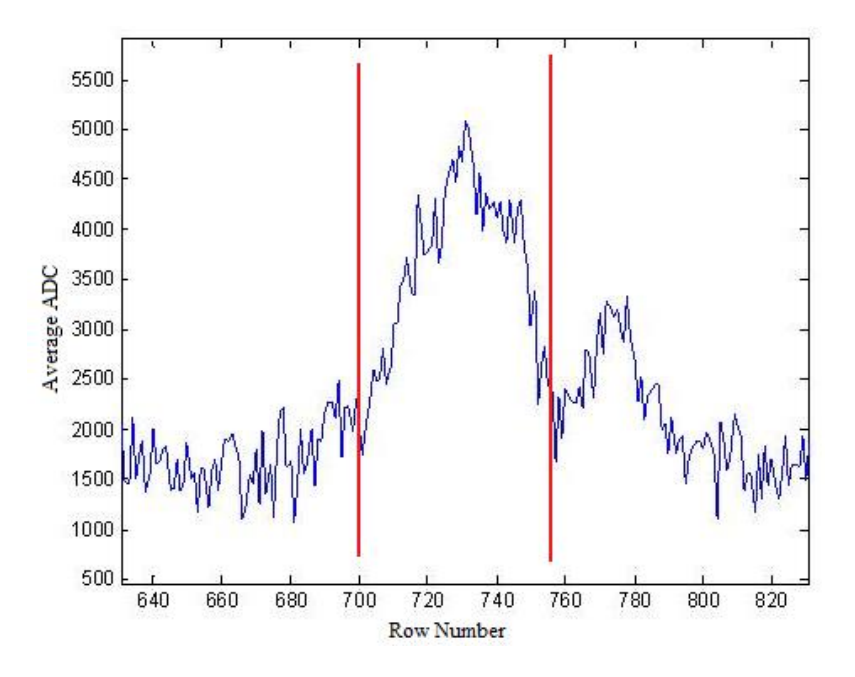


Figure 4.15: ADC profile down column 1040 of the collimated fluorescence spot from the previous image in BGO $\,$

of fluorescence from the collimator image. Therefore as each pixel is $40\mu m$ in width and the fluoresced area appears to have a diameter of 57 pixels (± 5 pixels), this equates to a resolution of $2280\mu m$ or $2.3\pm0.2mm$ (to one decimal place). This is huge and clearly shows much error in this method as a $300\mu m$ collimator was used. Human error, spread of light off the surface of LAS (due to certain amounts of reflectivity) and total internal reflection are likely to be the largest contributors to error in this case. From this it can be concluded that the spread of light in BGO is particularly bad. In future, the Modulation Transfer Function of the APFPI will be calculated to represent the spatial resolution.

4.3 Hamamatsu Scintillators

The results obtained from the Hamamatsu bought scintillators are discussed in this section of the report. The measurements made previously on Hilger Crystals' samples were repeated on Hamamatsu scintillators. Modulation Transfer Function (MTF) data is finally able to be calculated and discussed as a means of spatial resolution assignment thanks to the large surface area of the Hamamatsu plates. After some further investigation into the clarity between various MTF data (this is discussed in the following results) it was taken into account that the angle of the collimator when secured into the X-ray set was not completely perpendicular to the surface of LAS and hence the scintillator. A height correction was made using basic trigonometry which is discussed toward the end of this section.

As discussed in the section "Initial Testing and Preliminary Characterisation of LAS", it was mentioned that a Flat Field Correction Image needed to be taken in order to obtain a completely true image (after correcting for noise edge settings and gain differences in the pixels); this was completed for each different scintillator plate. The method used is to basically illuminate as large an area as possible with x-rays (using the 1cm steel collimator) and sweep over the entire area of the exposed scintillator plate, recording an average of 10 frames per spot position. Go Ono and the author created a code in MATLAB which would then sum the separate ".raw" files for the different positioned collimated spots and using an iterative technique combine the data resulting in the following complete flat field correction image; figure 4.16.

The edge of the Hamamatsu scintillator plate is clearly defined in this figure, indicating a small boundary of a couple hundred μ ms of exposed effective area of LAS. This however is not damaged by X-ray radiation due to the presence of the cured carbon-fibre mask which overlaps the edge of the scintillator plate by approximately 1mm, as explained in the previous chapter, section 3.6. To the right of the plate is an area of brighter contrast, this is simply a high abundance of the optical grease used from Cargille Laboratories

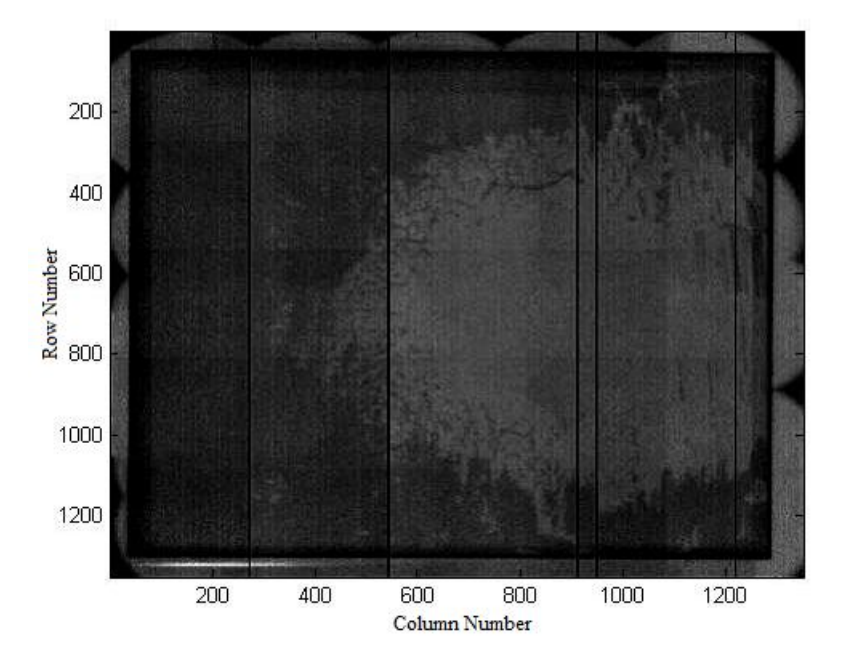


FIGURE 4.16: Complete illumination of the Fibre-Optic Scintillator plate bonded to the surface of LAS. This method was carried out for each of the scintillator plates

which has not spread out evenly across the detector surface. Application of the grease is difficult, however to avoid air bubbles the best procedure involved applying the grease evenly over the correct side of the plate and smearing the grease around LAS once the plate was placed on top. Thickness of grease layer was important as; too thin - air bubbles will appear; too thick - optical spreading between adjacent pixels will be high. Using the silicon pin detector once more the stopping power had to be studied for the five different plates which were purchased from Hamamatsu Photonics. Figure 4.17 displays the findings. After just 20kV the high resolution amorphous-Carbon scintillator (ACS) (50% light output ACS in the figure) and the Aluminium scintillator (ALS; scintillator not substrate as this is the name given to the product by Hamamatsu) begin to show signs of low stopping power with increased radiation being detected by the silicon pin. By 30kV both ACS and the ALS plates are out of the 10% error range. Continuation of rising Keithley current concludes that these scintillator plates are not suitable for X-ray testing above 20kV operating tube voltage, when mounted to the CMOS device. The remaining high light output and high resolution fibre-optic scintillator (FOS) plates on the other hand, produce good results and shall be further used in light output characterisation tests.

Due to the low stopping potential of the 150μ m CsI(Tl) comprising the ACS and ALS plates, a 1500μ m thick CsI(Tl) high light output ACS plate was purchased from Hamamatsu. With this increased volume of absorbing material the results for the stopping power should be better, as well as producing a greater light output due to a thicker layer of CsI(Tl). With more scintillation material for the X-rays to interact in, there

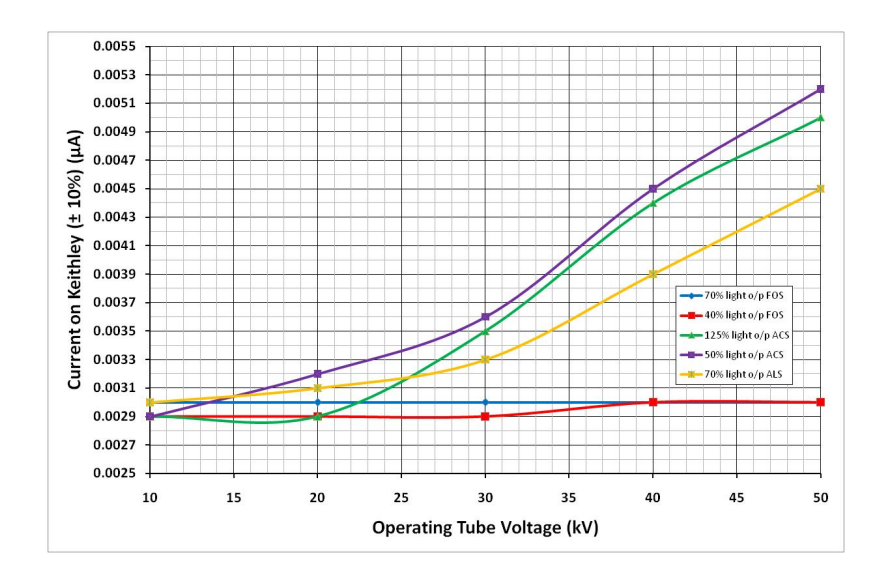


FIGURE 4.17: Plots for stopping power of five different substrate CsI(Tl) scintillator plates from Hamamatsu Photonics. Tube current was held constant again at 30mA

should be a higher conversion of photoelectrons (more active sites in the lattice for luminescence to occur). ACS was chosen over ALS because of the rise in Keithley current seen in figure 4.17. Hence it was deduced that amorphous-Carbon has a greater attenuation than Aluminium in the energy range concerned with for this investigation. This is because the substrate of the scintillator plate was on the top surface. I.e. the surface not bonded to LAS. With a lower attenuation, less X-rays will be stopped, therefore a greater number will pass into the CsI(Tl).

Figure 4.18 displays the plot of the $1500\mu m$ CsI(Tl) ACS plate in comparison to the results for no material covering the silicon pin detector.

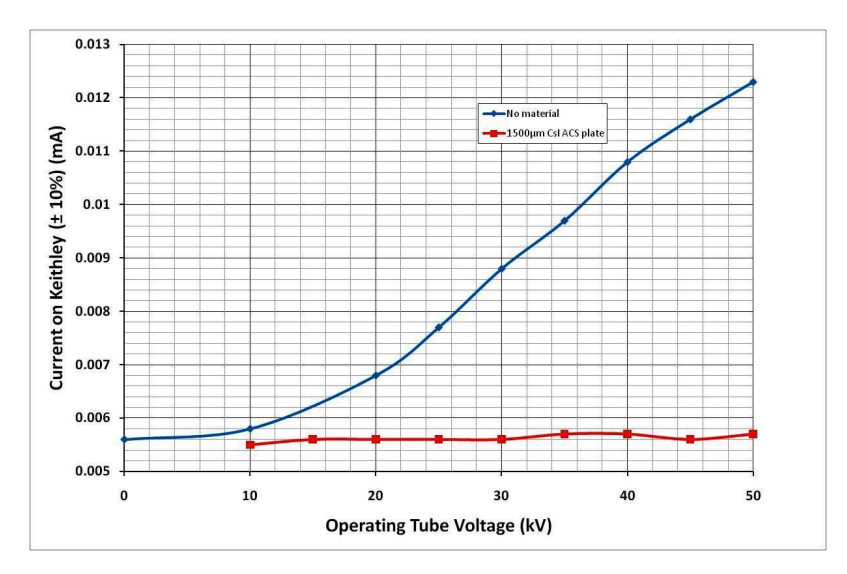


Figure 4.18: The stopping power data for 1.5mm of $\mathrm{CsI}(\mathrm{Tl})$ bonded to an amorphous-Carbon substrate

It is clear that this material, like the two FOS plates, prevents up to 50kV x-rays being detected by the underlaying detector.

It was decided that the 150μ m ACS and ALS plates would not be used for the following experiments, even at low X-ray energies as the risk of radiation damage occurring to LAS and the chip-on-board electronics was too great. The light output tests for the remaining plates were carried out following the same procedure as for the Hilger Crystals' samples. The results in figure 4.19 indicate that saturation occurs in all scintillators; whether this happens suddenly in the case of the 1500μ m CsI(Tl) ACS or gradually as the high resolution FOS plate shows. With all the plates, no results (increased ADC pattern) were observed below an operating tube voltage of 10 kV; the light output was merely not high enough characteristic of Caesium Iodide likely to be due to self absorption within the plate.

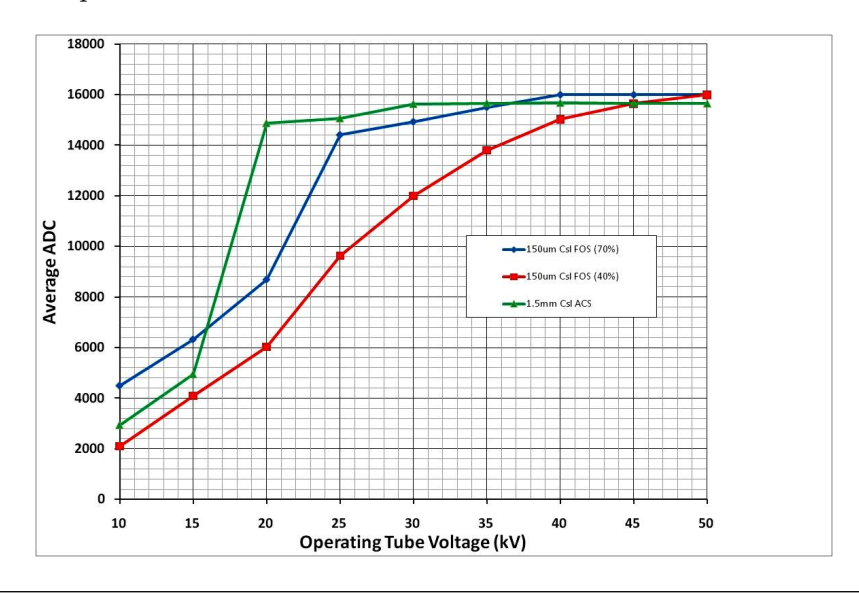


FIGURE 4.19: Light output testing for the two FOS plates and the thicker Caesium Iodide ACS plate with OptoDAQ frame rate running at 9.80 frames per second. Tube current is again held at 30mA

The proposed theory previously discussed regarding a thicker layer of scintillator material seems to be correct, as the $1500\mu m$ CsI(Tl) gives nearly double the ADC level at 20kV than the high light output FOS plate, even though it starts with a lower ADC at 10kV; where the results begin. The sudden rise in the data for all three plots, yet more effectively seen in the thicker Caesium Iodide is because of more efficient excitation. Concerning the ACS plate, the light output tends to rapidly decrease between 20kV and 15kV. This is likely to be due to insufficient energy from the X-rays. Hence there exists a threshold between these energies where the electron leaves the valence band, moving into the conduction band and leaving a hole pair. So the excitation energy ranges between 20kV and 15kV. Further investigation revealed the plot is steepest between 17kV and 18kV. The X-ray set does not go to 0.1kV however and only works in

integers. Given the apparatus supplied therefore, the excitation energy of the electrons is concluded as between the region of 17kV to 18kV; for the ACS plate at least. This is not seen to be due to any of the photoelectric absorptions edges observed with XCOM.

4.3.1 Frame Rate Alteration

All data for light output testing up until this point has been collected with the OptoDAQ software running at 9.80 frames per second (fps). This essentially means that there are 9.80 snapshots of data taken every second by LAS. So if a single image consists of say 100 frames, it will take 10.2 seconds to record the ".raw" file of this image. More importantly if the frame rate was sped up (integration time slowed down) to the maximum the software can record (20.69 fps) then the light output should be less; and vice versa if frame rate was slowed down. Figure 4.20 shows exactly this phenomenon.

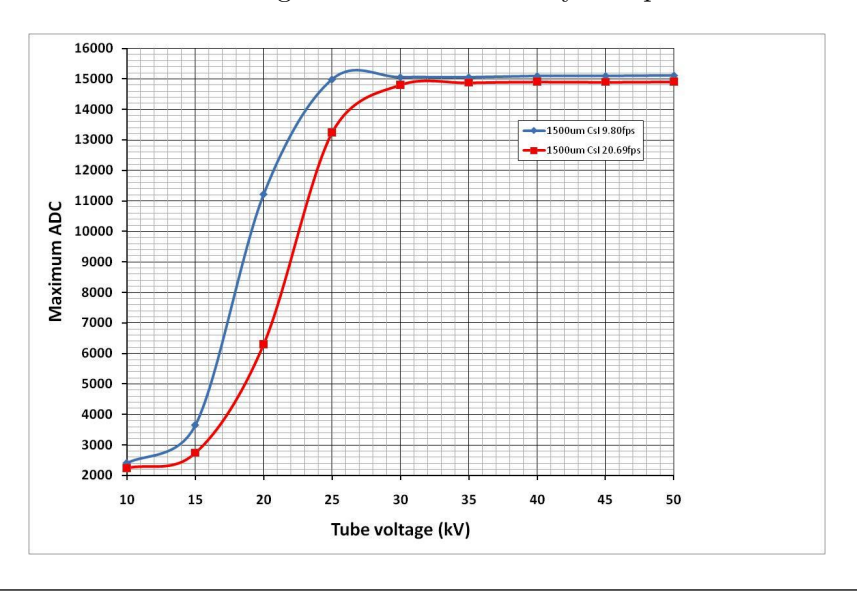


FIGURE 4.20: The effect of changing frame rate (or integration time) of the OptoDAQ on the light detection of the system

With a faster frame rate, less light can be gathered by the detector per "snapshot". It does allow 100 frames to be recorded more efficiently though. As figure 4.20 suggests, the system requires a higher intensity of X-ray radiation in order for saturation to be achieved. i.e. no more photoelectrons can be detected in that given time.

Using this mode of operation it is possible to vary the light output of the scintillator material without actually having to modify the physical make-up of the APFPI.

4.3.2 Spatial Resolution Measurements

Unlike previously with the Hilger Crystals' samples it is possible to obtain a clear and defined knife-edge image using the scintillator plates from Hamamatsu. Due to the substrate's area it is possible to use the wide collimated steel tubing (as again it is near impossible to get any kind of edge using the 300μ m collimator used for the light output tests).

At the end of the previous chapter it was discussed how a MATLAB code was written to analyse the data obtained from the knife-edge images, finally resulting in the calculated MTF after processing edge spread function (ESF) and line spread function (LSF) data. The following final results are therefore produced in MATLAB as normalised plots. They are also the final stage of the procedure in section 3.6 which details the method of how the MTF was calculated from the raw data taken by LAS.

The first of the MTF results, figure 4.21, is purely associated to the high light output FOS plate only. By recording data prior to the excitation energy, after it but before saturation and finally once saturation has been reached (20kV, 30kV and 40kV respectively), the MTF can be analysed throughout the course of the scintillation mechanism as intensity is increased.

Note: for the clarity of the image, the tube current remains at a constant 10mA rather than 30mA. This simply reduced the amount of X-rays bombarding the scintillator material, not their intensity. Frame rate is also returned to 9.80 fps.

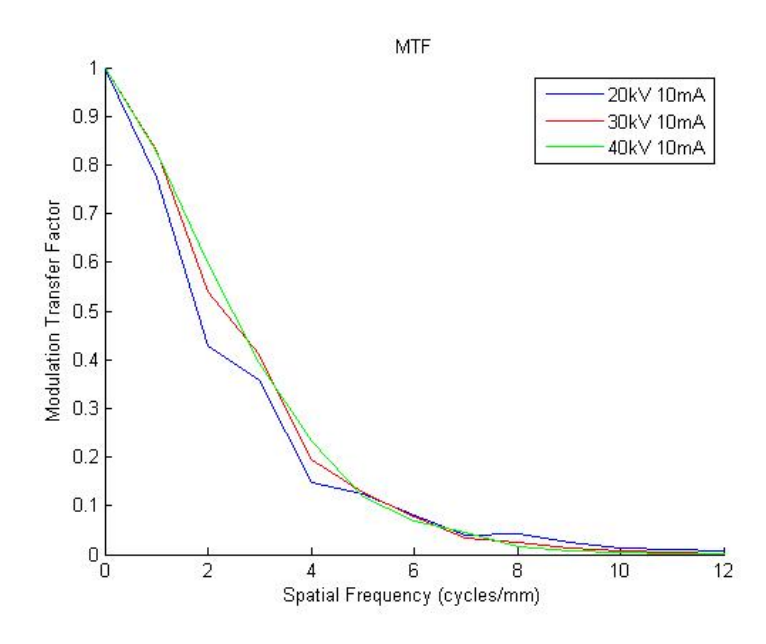


Figure 4.21: Normalised MTF result for varied X-ray intensity upon the 70% light output FOS plate

As the first set of MTF results, it is noted that for the 20kV and 30kV plots more

points along the LSF curve needed to be assessed. This would have smoothed the data more. However it can still be seen that at a spatial frequency of around 3 cycles/mm the saturated data is best. This is not too much of a surprise as in this state the image exhibits a greater contrast difference. At a modulation transfer factor of 1, i.e. 100% modulation of the image (the true image is perfectly replicated by the CMOS sensor), the spatial frequency is zero. This implies that one would require no image in order to achieve 100% modulation. A meaningless situation as no imaging device in science or nature is "perfect". This was discussed in the theory section of this report. Ultimately the results for this data proves the theory correct; as spatial frequency is increased (the number of cycles a wavefunction will perform every millimeter) the modulation of the replicated image by the imaging device decreases with an exponential relation.

By carrying out the same method as before (recording data at tube voltages corresponding to different stages of the scintillation mechanism) on the $1500\mu m$ CsI(Tl) ACS plate, it is possible to observe the difference between the high light output FOS plate and the ACS. Firstly, figure 4.22 shows the plotted MTF results for the amorphous-Carbon.

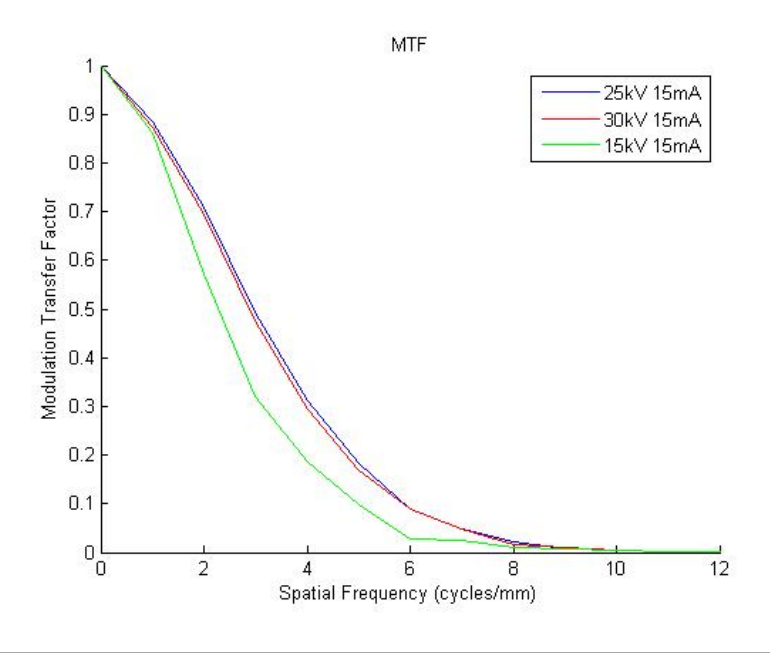


FIGURE 4.22: MTF data for the thick CsI(Tl) mounted onto an amorphous-Carbon substrate

The plots follow an identical pattern to previous set of data, resembling an exponential decay. The curvature is much smoother here however, due to better sampling, smoothing of the data and more points analysed in the ESF and LSF stages of the procedure to obtain the MTF. Importantly, it is the higher ADC values (generated by the higher tube voltage) which once again give the best modulation for a given spatial frequency. To determine which substrate is producing the best results, the data for each plate must be closely compared. Figure 4.23 plots the best curve from figures 4.21 and 4.22 against

one another. It may be said that this is an unfair evaluation as both tube voltage and current vary on both plots, however saturation has occurred in both circumstances.

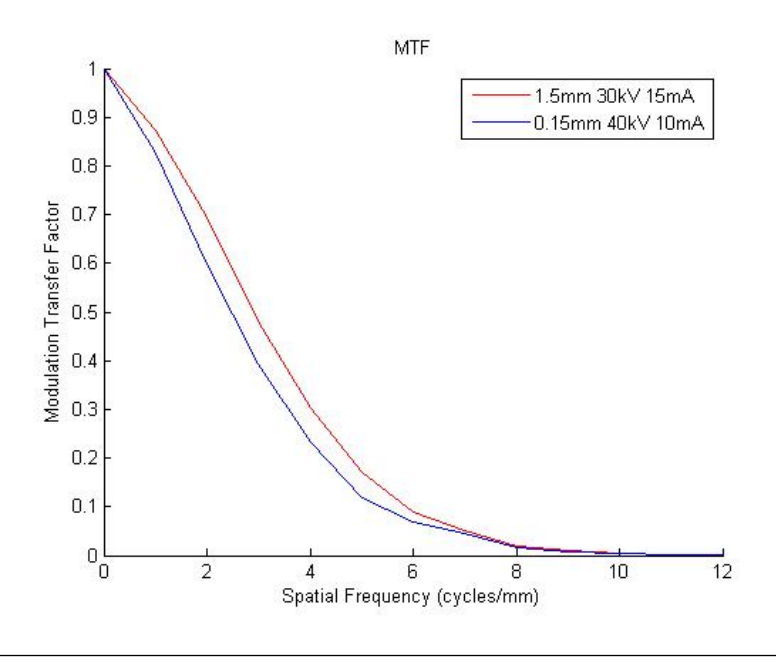


FIGURE 4.23: MTF comparisons between the FOS and ACS plates

It is noted that the two best results from the two plates is that of the highest X-ray intensity. The Fourier transform equation depends on the variable of the function in the transform and the variable of the transform equation itself. Therefore, it is not surprising that the higher ADC values give a better spatial frequency at a set MTF. Using this understanding the best MTF will be achieved when the tube settings are as high as possible (maximum light output) with no scattering of light (so as to get a sharp rise on the ESF curve from the knife-edge image); this has now been proved experimentally. There may be an error assigned to the plots in figure 4.23 and the previous data discussed in this subsection, however as the results have been generated by a MATLAB code it is difficult to accomplish this. There is certainly an error in the raw data from the OptoDAQ software as well as that in the modulation itself from LAS. The error in the optical transfer of radiation and photoelectrons between adjacent "levels" of the APFPI is also something worth noting. MATLAB itself may also carry a significant error to the final result, not to mention any human error involved throughout the investigation. This is all something to consider in future testing.

The method of Hiroshi Fujita *et al* was previously discussed in section 3.6, this is where the idea of smoothing and sampling the data originated for use in the MTF MATLAB code. Fujita *et al* finalises his report [40] by discussing the modulation transfer factor dependency with spatial frequency for the presampling data of a detector in a digital

radiographic system. The LSF is generated from a single slit exposure to the detector. By measuring the MTF at different sampling distances in the system, aliasing is neglected. His results however do not compare as closely as what has been discovered in this experiment. I.e. The images obtained from LAS are 50% modulated at more than 3 cycles/mm (for the best data) whereas Fujita only manages approximately 1.5 cycles/mm at this resolution. To conclude, the system which has been used together with the methods in these set of experiments produce a greater spatial resolution at a given modulation compared to Fujita et al's findings.

4.3.3 Height Correction

For the purpose of spatial resolution measurements, it was always necessary to keep the collimator as close to the surface of the scintillator as possible. This is because of the effect height correction has on the level of ADC in the fluoresced image. Figure 4.24 clearly shows the ADC value as a function of operating tube current. The three plots represent different heights of the collimator. The measurements of these heights in millimetres is the distance between the bottom of the X-ray cabinet and the position of the X-ray head without any collimator mounted into it. Essentially it is the scale on the z-axis of the X-ray head. 619.1mm corresponds to the z-axis height at which the collimator is flush with the scintillator plate. 872.3mm is the maximum height the z-axis will retract to. Keeping a fixed X-ray intensity of 30kV, the results can be used to analyse the relationship between the abundance of X-rays produced by the Tungsten filament and the ADC values.

Saturation occurs in the two lower z-axis readings, as the distance of the X-ray source to the scintillator material is reduced. X-rays are produced in a dimension of 4π therefore a greater concentration of radiation is incident upon the material when the separation is less. The ADC levels rise rapidly after 5mA in the 619.1mm and 672.3mm plots as energy is not sufficient enough to overcome the bandgap energy of the Aluminium protective film and CsI thickness.

4.4 Micron-Scale Spatial Resolution

Previously the spatial resolution of an image using the Hilger Crystal samples was determined by analysing the width of luminescence and comparing this to the actual divisions of the item being observed. This section continues with this method, and is also a way of displaying some of the practical imaging uses the APFPI can be used for. I.e. Basic imaging experiments.

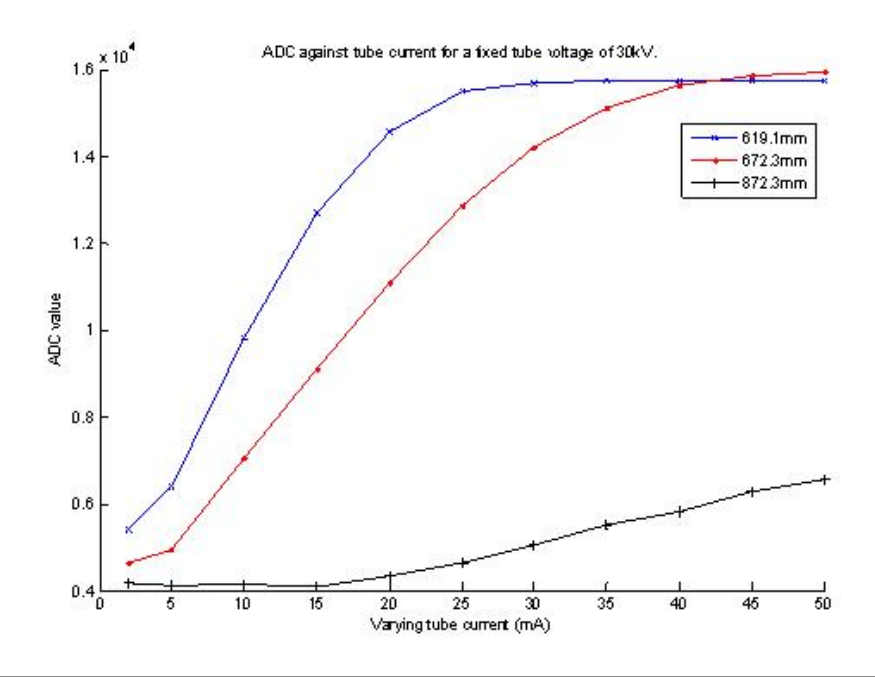


FIGURE 4.24: Varied height plots of ADC levels for the high light output FOS plate.

2mA is the lowest setting on the Seifert X-ray machine

A series of Aluminium foils were provided to the investigation courtesy of Fotofab Foils Inc. Figure 4.25 displays one of the images observed using low intensity x-rays. The $1500\mu m$ thick CsI(Tl) ACS plate was used in this example, along with the same viscosity optical grease as before (which can once again be seen in abundance to the right of the image). The image has a dark pedestal subtraction and flat field correction applied to it.

Profiling along row 800, the ADC relation against the column number can be deduced: figure 4.26. A MATLAB code was once again generated to obtain these results. From the left hand image the profile is clear and easy to assume that there is approximately a 50 pixel width for each small hole observed in the original image. Zooming in however on the smallest of the holes, furthest to the right, a width of 15 ± 2 (human judgement) pixels is determined. This is the right hand profile in figure 4.26. A hole width of this size is equivalent to $600\pm 80~\mu ms$.

Using the Zeiss stereomicroscope it is possible to measure dimensions on the foil to a better accuracy than the profiled ADC plot would suggest. Figure 4.27 is a photo taken of the same foil as seen in figure 4.25. Although the stereomicroscope carries an error in it's dimension measurements it is small enough to be neglected when comparing the data to the ADC profile as this error is the superior.

The measured width of the smallest hole in the figure is approximately $500\mu m$, resulting in a $16.7\pm2.2\%$ error in the combined MATLAB code and human judgement of the data. To conclude, the spatial resolution of an imaging system is much better determined by

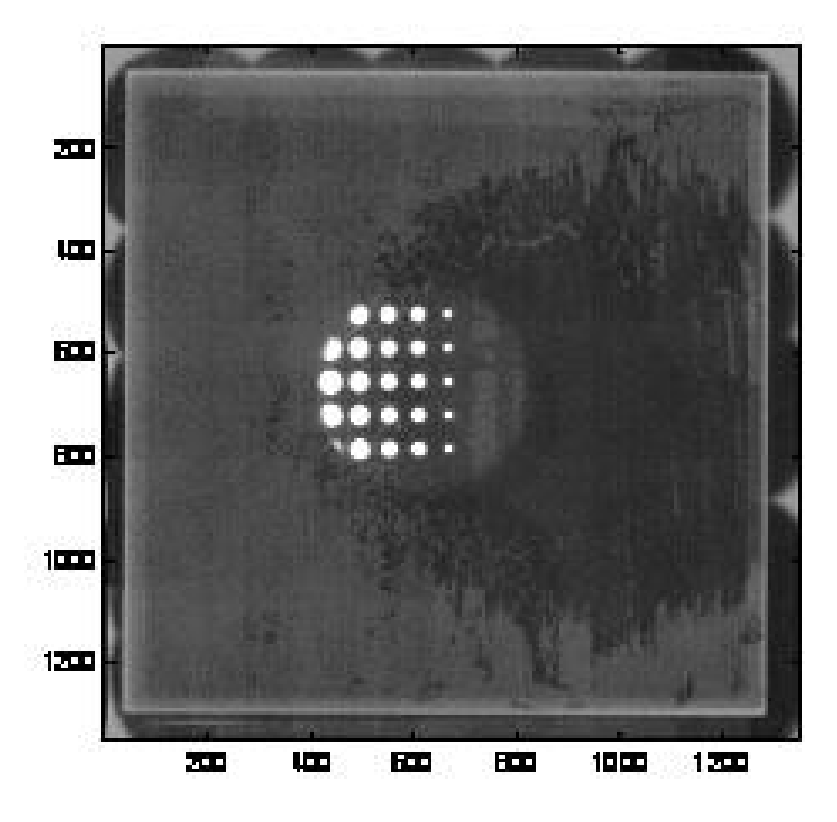


Figure 4.25: Imaging experiment with an Aluminium foil containing engraved patterns. Tube settings were at 20kV, 15mA. OptoDAQ frame rate at 9.80 fps and collimator flush against the foil resting onto of the ACS plate

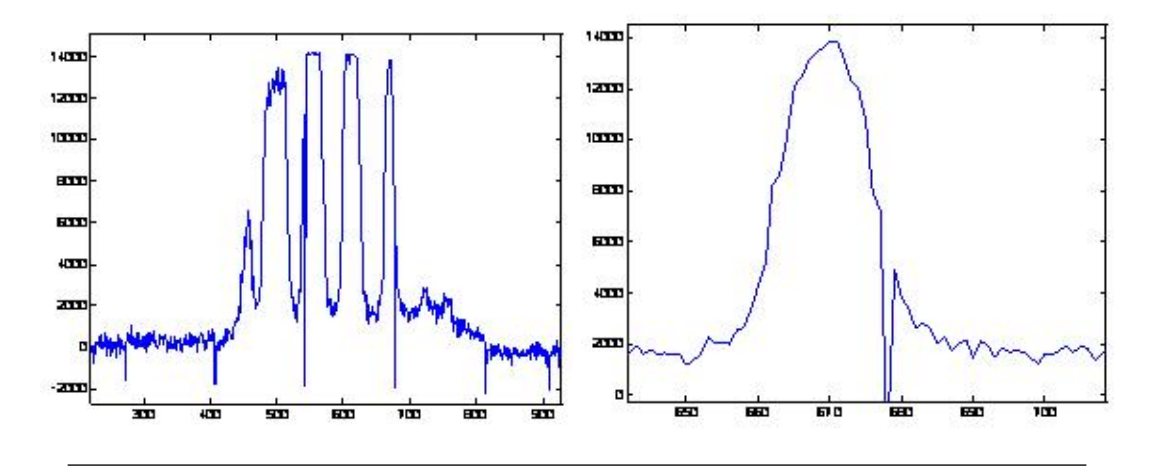


Figure 4.26: ADC profiles of the Fotofab foils for the previous image, showing all four holes (left) and a zoomed in view of the smallest hole (right)

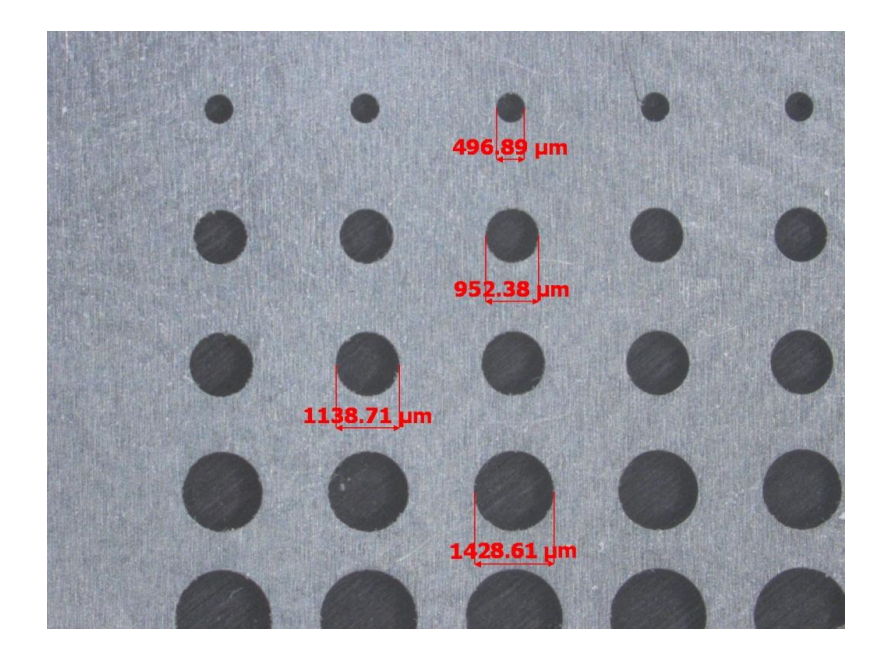


FIGURE 4.27: Accurate measurements taken of the same foil using the Zeiss stereomicroscope

observing the degree of modulation of the original image the system can produce. Although some error lies in profiling the amount of ADC, such error is only resultant due to how well the CMOS imaging system can depict between actually illuminated pixel and cross-talk or over detection of light on the sensor. The human eye also has to differentiate between true data and what is classified as being an error in the light detection. In other words, the clarity and hence modulation of the image.

Where spatial resolution is better to be quantified mathematically; such as using the MTF method, it can also be identified visually. However this latter method takes into account the largest error possible; the accuracy of the human eye. Therefore, by calculating the MTF of the system one is simply obtaining the desired result for the modulation of the APFPI without encompassing more error.

4.5 Imaging Experiments

This section concludes the results of the experiments carried out to date on this investigation. The images seen here, whether they are of a rat's skull (figures 4.28 and 4.29), a pocket watch (figure 4.30) or a mobile phone (figure 4.31) indicate the usefulness and wide application of the APFPI used as an imaging device. All images use the 1500μ m CsI(Tl) ACS plate (as it has been concluded that this produced the best results), with desired tube settings to make the images more effective.

A rat's skull was lent to the investigation for the mere purpose of definition of an image.

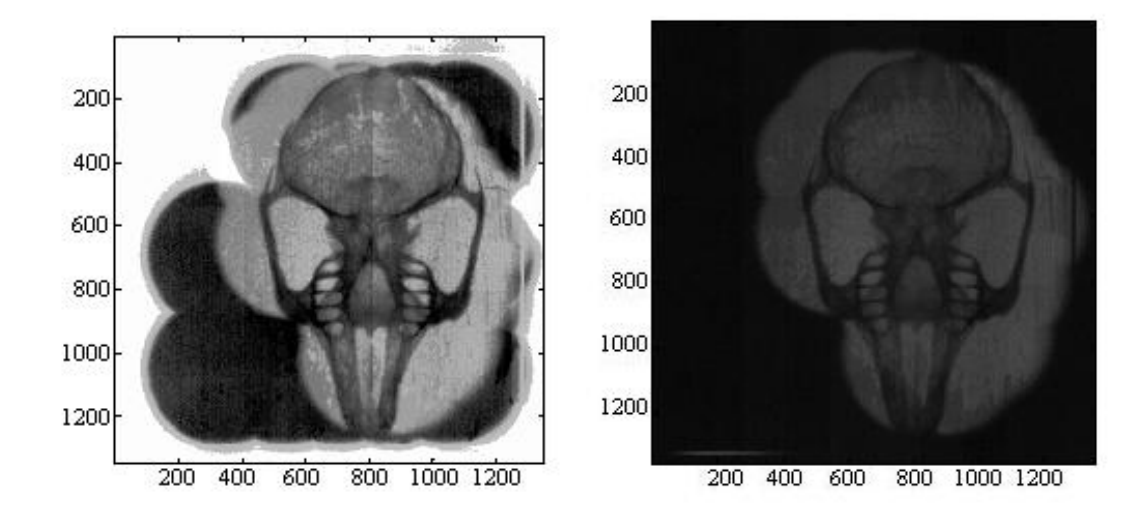


Figure 4.28: Image of a rat's skull with flat field correction (left) and dark pedestal subtraction (right)

Being made of bone, tube settings were reduced in order to achieve a good resolution; ideally around 15kV, 15mA. In comparison figure 4.29 shows how the skull appears under a microscope. The close likeliness indicates good light output and resolution of the system.



Figure 4.29: Microscope image of the rat's skull

4.5.1 Imaging at Diamond

Towards the end of the year placement, the opportunity arose to visit the Diamond Light Source and run basic tests with their X-ray setup. One of the fundamental drawbacks to the investigation so far has been the limited size of the collimator on the X-ray head. At Diamond the x-rays can be collimated to a size comparable to the area of LAS. Preliminary tests were tried and tested with this situation by imaging a pocket watch (figure 4.30). By the time testing was able to be carried out at Diamond, the investigation had received an updated LAS stack which could allow for a camera lens to be fitted to it. With new hardware came new software, of which the most beneficial characteristic was the ability to be able to set "regions of reset". This would mean that up to three regions on the observed image could have different integration times, hence darker and lighter sections on the image. This was excellent and proved very useful when the pocket watch was imaged, as to observe some of the mechanism in the watch the image would require a high X-ray potential, however some of the other features would not be seen then as X-ray radiation would pass through at these points.

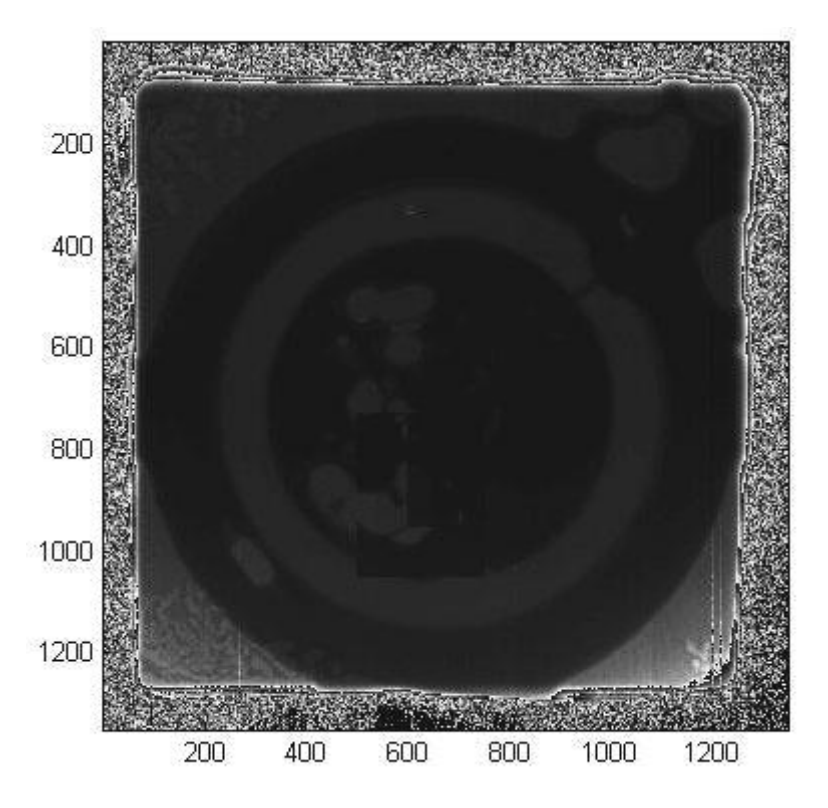


Figure 4.30: A pocket watch imaged with regions of reset visible using the X-ray set at Diamond

Regions of Reset can be seen in figure 4.30 around column column 500 to 700 and row 700 to 1000. This region allows the second hand to be observed by setting the frame rate lower (or integration time higher).

The same method has been used to view the inside of a mobile phone.

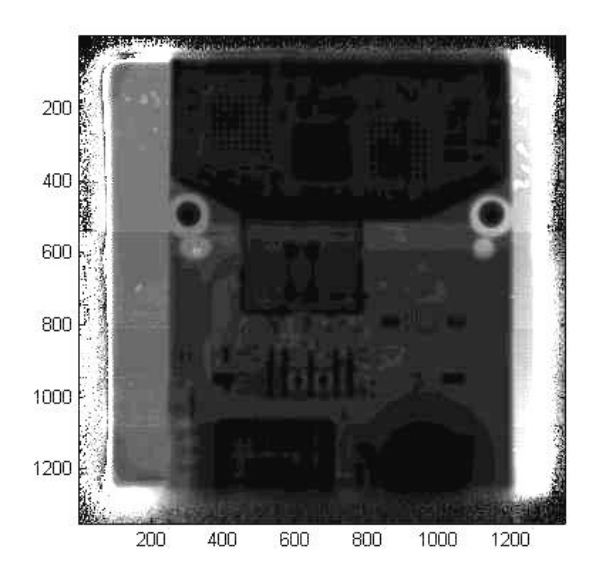


FIGURE 4.31: The inside of a mobile phone

Experiments with the new LAS stack and it's upgraded software shall form the key part of the investigation in my absence from the project. Other results such as the quantum efficiency of the system will also need to be analysed before Diamond can accept the project to be used on the I12 beamline. Further testing into these parameters shall be carried out by the replacing student on this investigation.

Chapter 5

Conclusions

This investigation has discussed and analysed theory, procedures and results as the start of a new project for the detector division at the Rutherford Appleton Laboratory: the production of a high energy X-ray imaging detector for the I12 beamline at the Diamond Light Source. So far the investigation has proved that various different scintillator materials can be mounted onto the surface of CMOS technology MAPS devices to form a detector system for X-rays up to 50kV operating potential.

5.1 Pedestal Images and Temperature Dependance

The dark pedestal images were generated using a MATLAB code which formats the data into a text file which is can then be easily subtracted from a raw file carrying the data which is required to be analysed, whether this is for MTF or light output testing. Flat field correction images are then taken for all materials tested which can then be combined with the dark pedestal data and the raw data to be analysed using the equation in the Dark Pedestal Image subsection in the Results chapter. This is done to lower the noise edge on each pixel and equate the gain to one another, hence reducing error in the final corrected image. Once columns of readout error and stitching columns have been adjusted for on the corrected image; polychromatic light testing may be carried out (or if advanced from this procedure, stopping power tests, provided a suitable scintillator has been chosen).

Temperature dependance on the system was researched and experimented upon. Placed in a sealed box temperature was recorded to reach in excess of $53.0\pm0.5^{\circ}$ C. It was researched that temperature stability was important as many performance parameters

are proportional to temperature such as dark current (which doubles every 7 degrees) and reset noise (which is equal to kTC). Placing a fan pumped by laboratory coolant in the box with the system, it was observed that the temperature of the LAS wafer stabilised at $24.2\pm0.5^{\circ}$ C. Therefore when cooling the system's surroundings the data recorded for the dark current will have a threshold noise error of 100 LSB compared to up to 350 LSB when not cooled. Cooling the experiments inside the X-ray cabinet however is not possible using the same apparatus set-up previously used. Temperature stability therefore is not able to be maintained; hence all results obtained to date could have a lower noise floor if a means of permanent cooling were to be introduced into the experimental set-up. This is perhaps something to consider in further investigations.

5.2 Researched Scintillators

After the research of many scintillator materials the key parameters required were; a high density (resulting in a high stopping power), a good light yield, a quick decay time, a low attenuation length in millimeters, commercially available in a large area (up to approximately 50mmx50mm) and cost effective. Making some compensation among these parameters four samples were purchased from Hilger Crystals Inc: LYSO, BGO, PbWO₄ and CdWO₄. All were found to have lower enough attenuation lengths (high enough stopping powers) to enable light output testing to be carried out, as surface areas of all samples were too small to obtain MTF data from. From this experimental procedure LYSO produced the best fluorescence energy (ADC) results shortly followed by CdWO₄. It was concluded though that unfair testing was apparent, as thickness of samples varied and LYSO and CdWO₄ were the thinnest of the Hilger materials. A thinner layer of scintillator will allow for ease of transmission of photoelectrons through the material, hence giving a more efficient light output. However a thicker scintillator will produce more photons at a higher energy, but have a lower transmission for light output therefore hindering photon movement at low energies. This theory must be considered when purchasing and testing all scintillator materials.

5.3 Hamamatsu Characterisations and Results

An additional, more widely used scintillator was then purchased from Hamamatsu Photonics which was available in areas up to that which met the requirement of 50mmx50mm:

CsI(Tl). With the presence of the dopant the light output of this material peaks at 530nm compared to the undoped emission of 310nm (outside of the visible range). Stopping power experiments confirmed that only two of the original five scintillator plates based on varying substrates were able to be mounted onto the surface of LAS, as the ACS and ALS plates only stopped up to and including 20kV x-rays from being detected by the silicon pin detector. On concluding this a thicker CsI(Tl) ACS plate was purchased from Hamamatsu. CsI(Tl) in the original FOS plates were characterised at being $150\mu \text{m}$ thick, however the new ACS plate's CsI(Tl) was ten times this at $1500\mu \text{m}$. This was sufficient enough to stop up to 50kV x-rays (likely to be higher however the X-ray machine used in this investigation peaked at 50kV operating tube voltage). As a result of the thicker Caesium Iodide the light output observed from the two different substrate plates was sufficiently better in the ACS plate. This is again due to the transmission properties previously discussed. Frame rates were also briefly observed as a changing variable to the experiments, with conclusion that a longer frame rate yields a lower light detection and hence fluorescence energy (ADC). This is because there is a shorter time period for the sensor to detect the incident light.

Normalised MTF data was calculated and analysed using a MATLAB code written with the assistance of Go Ono and Matt Wilson. The results were achieved by following the method laid out in the Experimental Arrangement chapter of this report. The extent of modulation of the image recorded by the CMOS MAPS was determined and given as a percentage as a function of spatial frequency. The images obtained from LAS were 50% modulated at more than 3 cycles/mm spatial frequency given by the ACS plate; concluding the best data and plate to use. This was compared to existing results recorded by Fujita et al where only he manages approximately 1.5 cycles/mm at the same resolution. The system used in these sets of experiments, the methods to which the data was recorded by and importantly the classification of the APFPI produce a greater spatial resolution at a given modulation compared to Fujita et al's findings.

5.4 Further Work and Summary

The quantum efficiency (and to a greater extent the detective quantum efficiency) of the system was hoped to be studied in this investigation. To date is has not been and certainly will need to be looked at in further experimentation. Essentially deriving the number of x-rays converted into photoelectrons and then actually being detected by the sensor wafer, it is an important parameter to know and understand. However, in hindsight this investigation had been started with the commencement of the placement and to get to a good evaluation point was a goal in itself, well completed. The project

began with research and has gone on to see construction of apparatus in readiness for experimental procedures both carried out and yet to be tested, plus the important testing application and analysed results. All this has subsequently lead to further funding from the CfI program to continue the application for a high energy X-ray imaging detector for the I12 beamline at the Diamond Light Source and to develop further imaging devices within the Detector Division at RAL with the use of scintillators bonded to APS technology.

Appendix A

Workshop Sketches

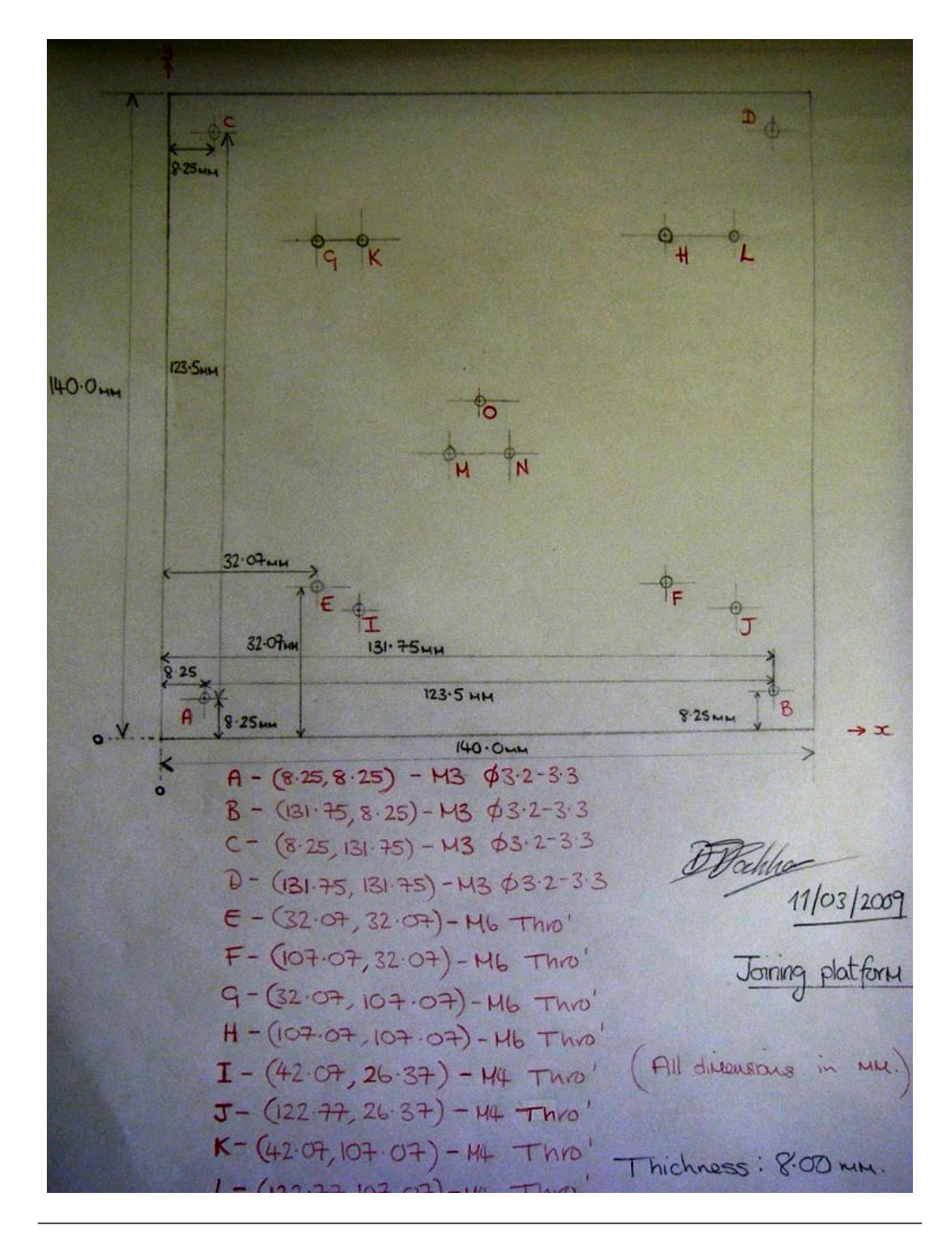


Figure A.1: Workshop sketch for the aluminium manufactured mounting plate for the LAS stack to the Newport linear, z-axis movement stage

Appendix B

OptoDAQ user manual



CMOS Sensor Design Group

MI3 OptoDAq User Guide for the Large Area Sensor (LAS)

Document Revision V1.0 Andy Clark 18 July 2008

Document History:

Author	Comment	Revision code	Date
Andy Clark	Draft	0.1	18/06/08
Andy Clark	Release	1.0	25/06/08
Andy Clark	Updated following user comments	1.1	21/07/08

TABLE OF CONTENTS

	Related	d Documents	2
1.	Intro	duction	3
2.	Syste	em	3
	2.1	Hardware	3
		Host PC Requirements	
		Software	
		Firmware	
		p	
		System Board	
		SystemACE Module	
		Camera Stack	
		Power Supply	
		Computer Setup	

RELATED DOCUMENTS

Document Title	Author
LAS Operations Manual	A Clark
MI3 LAS DLL Guide	C Angelson
LAS Vector Wizard User Guide	A Clark

Table 1: Table Detailing Documents Related to this Manual

1. INTRODUCTION

The MI³ OptoDAq system is designed for the control and image retrieval of Active Pixel Sensors such as the RAL StarTracker and sensors developed under the MI³ Basic Technology Grant. The system is based around a Memec Virtex-II Pro™ 20FF1152 FPGA development board which generates the require control signals for the target device and is equipped with an optical transceiver to enable upload of the image data to a host PC at Gb/s speeds.

Once uploaded to the host PC the image data is transferred efficiently to the supplied viewer application (or other software environments such as Matlab or LabView) via dedicated C++ middleware.

This document outlines the principles of operation of all stages in the data flow from sensor to the controlling application and a description of the supplied user interface.

2. SYSTEM

2.1 HARDWARE

The base OptoDAq system consists of a number of component parts, if have not received all the parts listed below then please RAL:-

Memec Virtex-II Pro™ 20FF1152 development board ATX Power Supply D-Link Gigabit Ethernet Adapter (PCI) 1Gbit LC Optical Transceiver LC to SC Optical Duplex Cable SystemACE Module 32MB Compact Flash Card CF Card Reader Samtec EQCD 120-way high performance coaxial cable

In addition the system contains sensor specific parts for LAS:-

P160 to Samtec adapter board Camera stack assembly (including 9 PCB boards, not to be disassembled) Sensors mounted on Chip on Board (CoB) cards

All these parts are supplied by RAL.

2.1.1 HOST PC REQUIREMENTS

The minimum PC requirements are:-

PC Running windows XP or 2000 Pentium III or Equivalent/Higher 1GB of RAM PCI 32/64bit slot (for Gbit Ethernet Adapter) The recommended system which should be sufficient to control the future PEAPS system operating at full frame rate are:-

PC running windows XP
Pentium IV or Equivalent/Higher
2GB of RAM
PCI(-X) 64bit 66MHz slot (for Gbit Ethernet Adapter)

We have procured such a PC for approximately £1000; we can supply you with details of the PC and a supplier if required.

We have also successfully operated LAS from a Laptop using a specially procured Ethernet card. WE can provide details of the laptop and the network card on request but please be aware that it may not be possible to operate at the higher end of frame rates from a laptop.

2.2 SOFTWARE

From the first LAS release the software distribution has changed slightly compared to previous DLL releases. The DLL and associated files will now support only one type of sensor; this should prevent the use of multiple DLL files with the same name for different sensors.

The main body of software is contained in the DLL release. The current version is 1.2 and is available on the MI3 website. The file is called "LAS_Software_V1_2.zip" and contains the following files:-

Quixtream.dll mi3_las.dll mi3_las.h mi3_las.lib optodaq-LAS-V1_2.xml las viewer 1 2.exe

If you wish to interface OptoDAq directly with your own software in LabView, Matlab or something similar; then please see the LAS DLL user guide for more details of the DLL interface. If you do not wish to write custom interface applications we have supplied a graphical interface executable program 'las_viewer_1_2.exe'.

The final part of the computer software is the vector generator which has been written as a Matlab program but is also available pre-compiled as a standalone executable if a Matlab licence is not available.

The Matlab version contains the following files:-

las_pat_wizard.fig las_pat_wizard.m LAS_run1.m write_bin.m write_mif.m

The precompiled version contains the following files:-

las pat wizard.ctf

las_pat_wizard.exe

To use the precompiled version of the vector wizard you must also install the Matlab Compiled Runtime Installer from the same page on the MI3 website.

2.3 FIRMWARE

The latest version of the FPGA firmware for LAS is currently 1.1. The firmware is available as an image for the compact flash card including the latest versions for Vanilla and StarTracker. The file is called "St_v1_1-OP_v3_0-Van_v4_0-LAS_v1_1.zip".

Installation of the above sets of files is described in the following section.

3. SETUP

The setup process is defined below. If you have previously used the OptoDAQ system for another sensor most of these steps can be ignored. However, there are some new settings required for the latest Vanilla or LAS releases marked in bold.

3.1 SYSTEM BOARD

The system board is a Memec 2VP20FF1152 development board including a Xilinx Virtex-II Pro™ 20FF1152 FPGA.

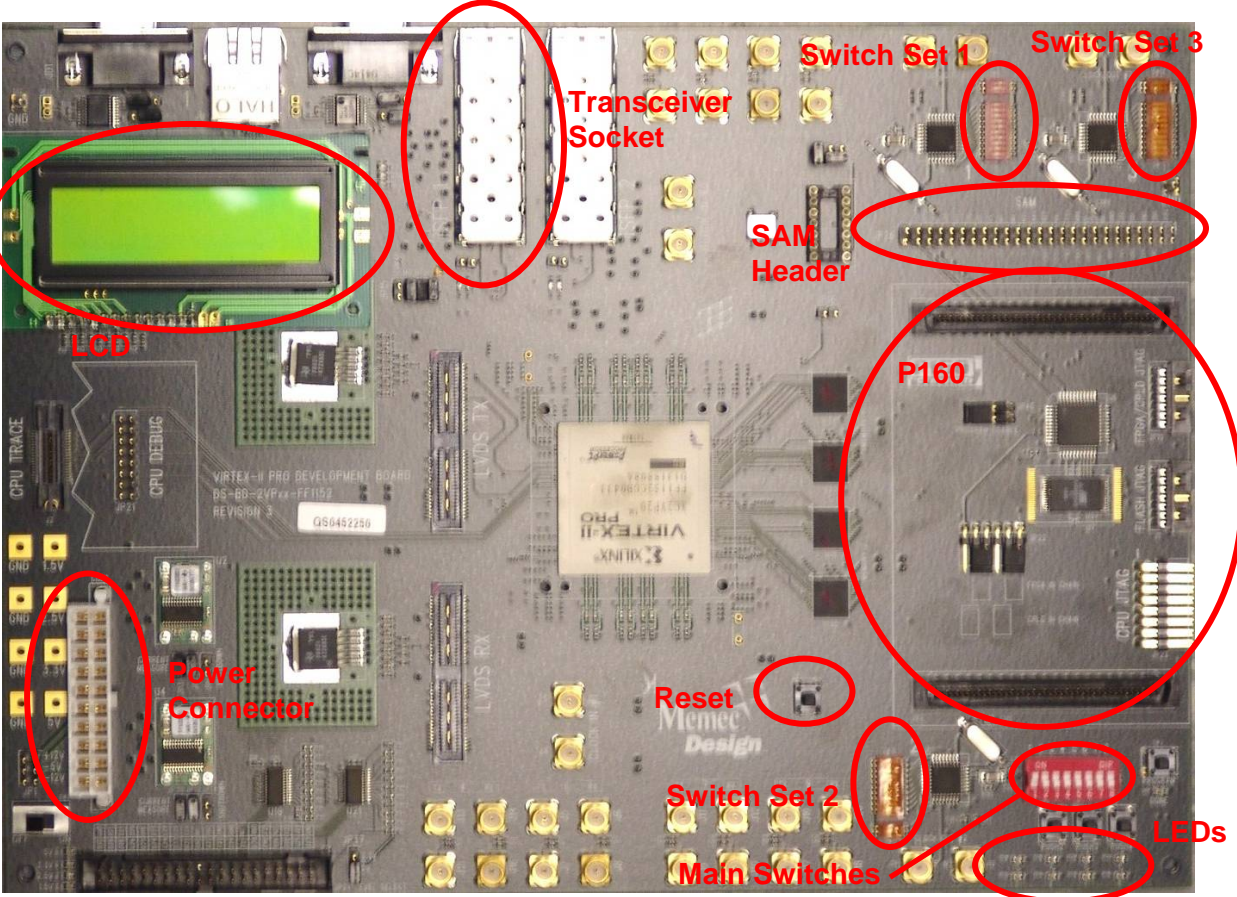


Figure 1 - OptoDAq base FPGA board

The four banks of switches show in Figure 1 need to be configured as shown in Table 2, Table 3 and Table 4. **Note: These settings are new for the latest versions of Vanilla and LAS but should not affect the operation of previous sensors and versions.**

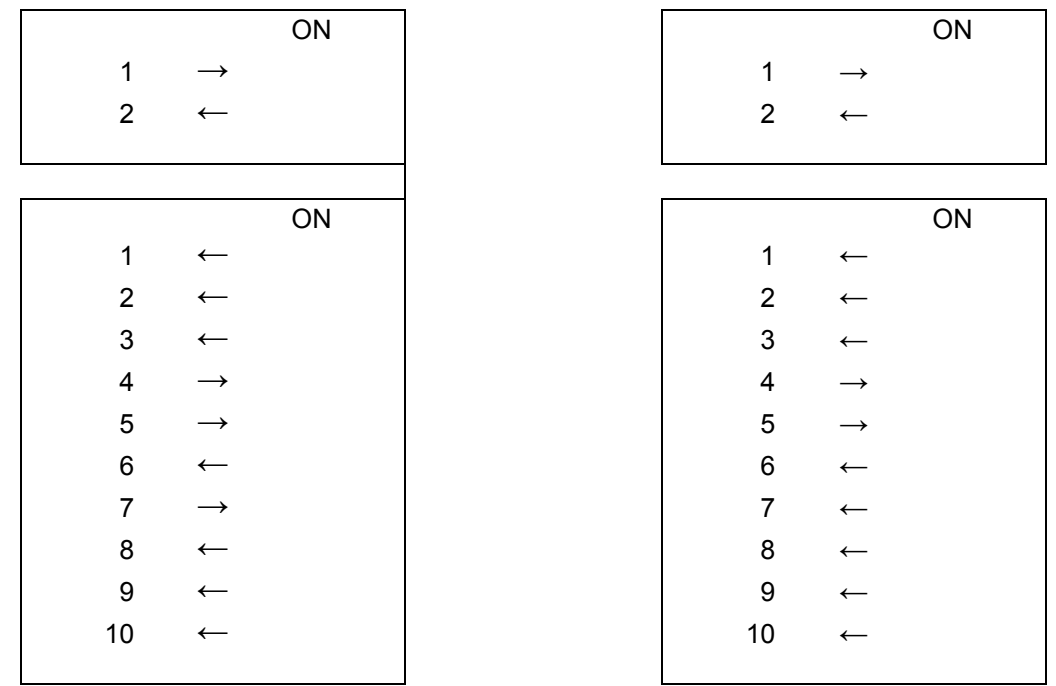


Table 2 - Switch settings for switch sets 1 and 3

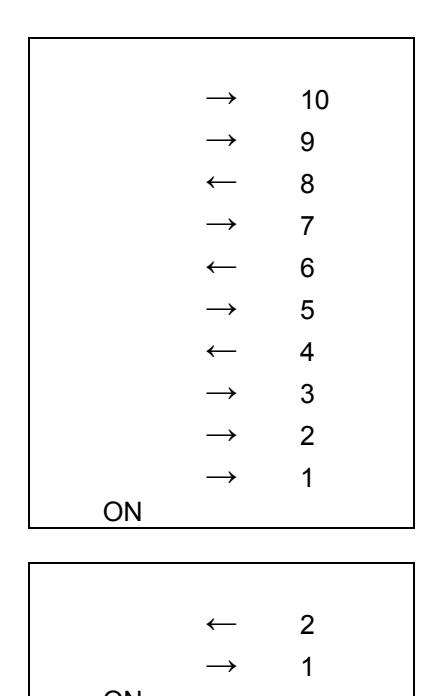


Table 3 - Switch settings for set 2

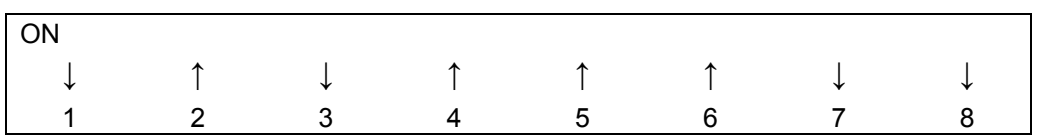


Table 4- Switch settings for main switch bank

3.2 SYSTEMACE MODULE

The systemACE module (Figure 2) should be attached to the SAM header on the system board (Figure 1). To enable the systemACE configuration the on board PROM should be disables by removing JP40 from the system board, this can be found between the P160 connectors. The SystemACE voltage should also be set to 3.3V by adjusting the supply jumper on the systemACE module.

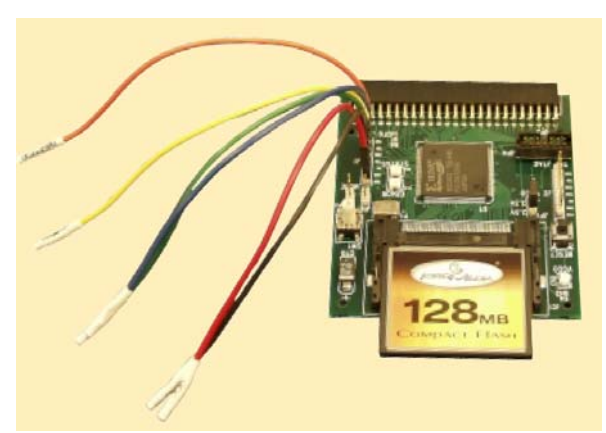


Figure 2 - SystemACE Module

The systemACE module allows up to 8 different configurations for the FPGA to be selected using the rotary switch. To avoid confusion MI3 sensors have been allocated specific locations on the systemACE file, as shown in Table 1.

Location	Sensor
0	StarTracker
1	OPIC
2	Vanilla
3	LAS
4	Not Yet Used
5	Not Yet Used
6	Not Yet Used
7	Not Yet Used

Table 5 - SystemACE Index

Configuration files can be downloaded from the MI3 website OptoDAQ page, the configuration files are in a .ZIP archive, the file name will detail the sensors and version numbers of the relevant firmware included. The archive consists of the following files and folders all of which should be copied to the route of the Compact Flash card:



Directory and file names may differ from the above but the 'xilinx.sys' files will not change. The CF cards are supplied with the correct formatting (FAT16), sometimes however the formatting can become corrupted and in this case the card should be reformatted. It is not possible to do this correctly with windows, however a third party application is available called mkdosfs. This can be found on the MI3 website. The mkdosfs.zip file should be

extracted to a directory such as c:\mkdosfs. The program can then be executed with the following command:

C:\mkdosfs> mkdosfs G:

Where G is the drive letter which refers to the CF card.

With a configuration loaded onto the Compact Flash card, the FPGA is programmed when the CF card is inserted into the systemACE module or the system board is powered up. The FPGA can be reprogrammed at any time by pressing the 'reset' button on the systemACE board. After programming it is advised that the FPGA is reset using the 'PUSH1' button on the system board.

3.3 CAMERA STACK

The LAS camera stack shown in Figure 3 contains sensor biasing and readout circuitry.

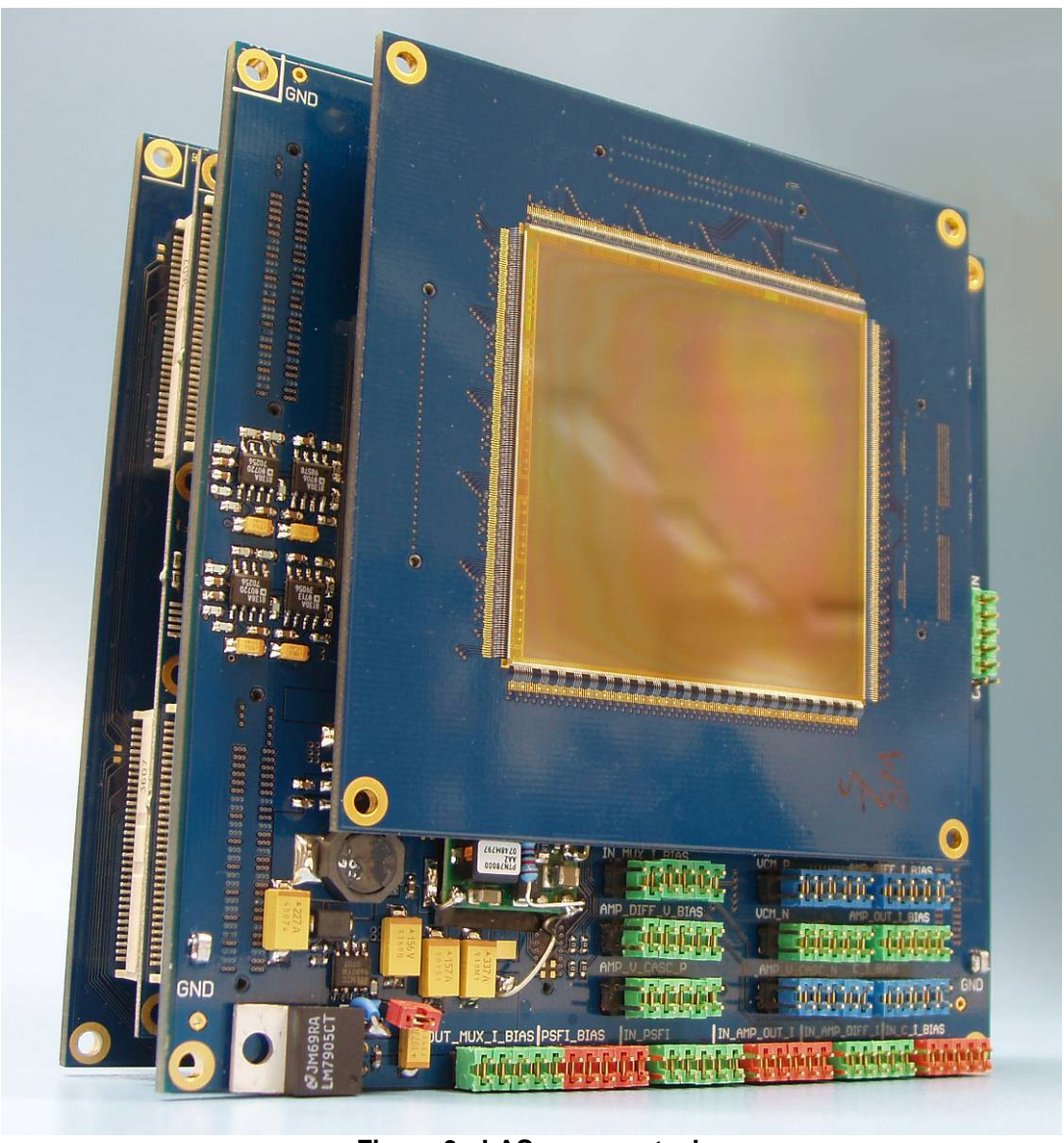


Figure 3 - LAS camera stack

3.4 POWER SUPPLY

The LAS camera stack requires a separate 12V supply. This is connected to the stack via the ATX power connector on the back. The 5V pin in the connector is not used. A cable has been supplied to connect the stack to a bench supply. It may be possible to use the same supply as the base OptoDAq board by utilizing the unused peripheral lines but this has not yet been tested. The standard OptoDAQ supply cannot supply the required 1.5A max. But there may be some change to the system noise level (for good or bad) if a single supply is used for the whole system. This will be investigated.

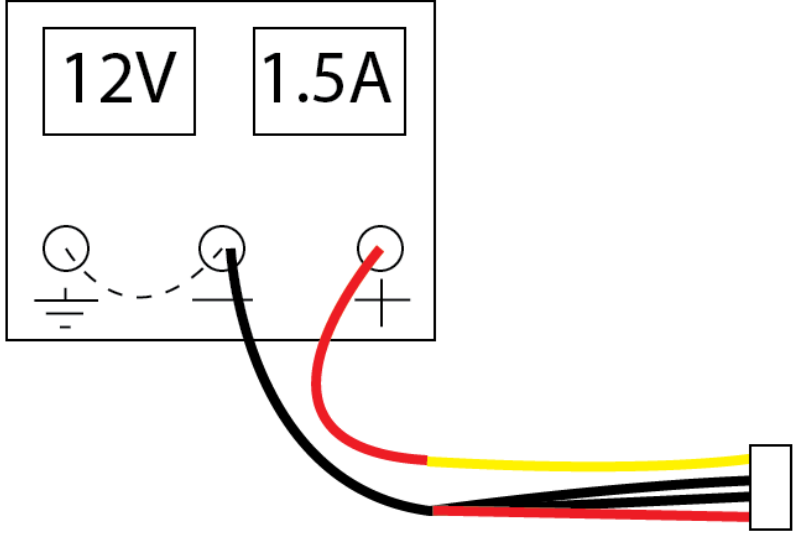


Figure 4 - Stack power supply

3.5 COMPUTER SETUP

First install the network card in the PC. A 64 bit slot should be used if available.

Before turning on the PC. Install the Optical transceiver in the iSFP1 socket on the FPGA board and LAS P160 to Samtec board on the FPGA board

Turn the PC on.

To configure the network adaptor admin privileges are required. Currently operation also requires admin privileges as the program executes an ARP assignment during setup of the UDP communications. This may change in future versions.

Please follow steps 1 to 7 to install the Network adaptor and configure the OptoDAQ system:-

- 1. Drivers should be installed from the CD provided or from Microsoft 'Windows Update'.
- 2. To configure the network adaptor, open Control Panel -> Network Connections and right click on the Local Area Connection 2 to open properties. Verify that the connection refers to the D-Link DGE-550SX card. See Figure 5.

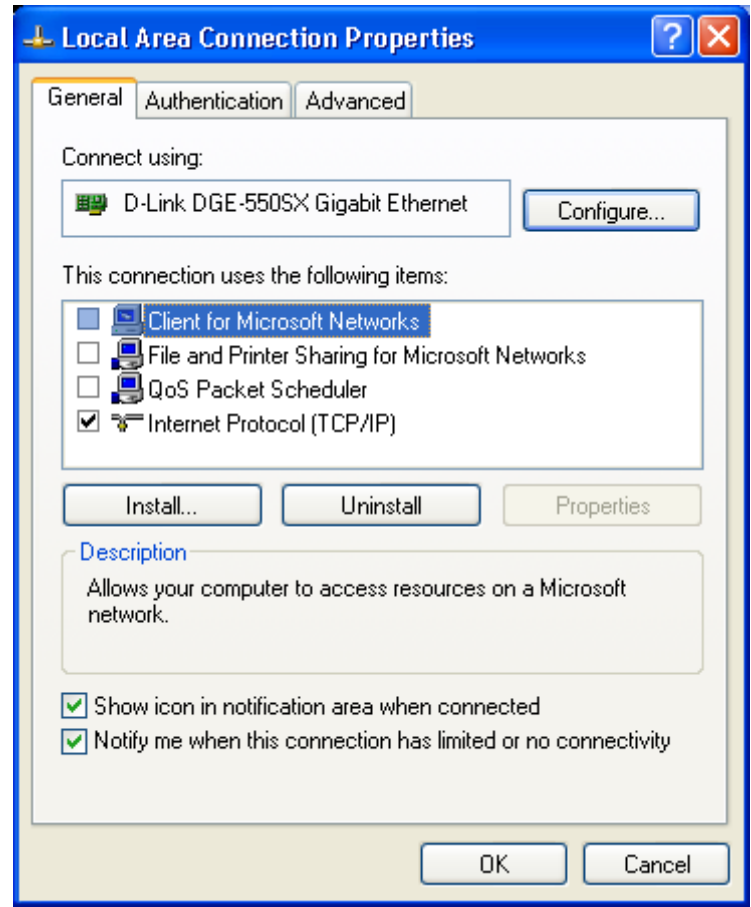


Figure 5 - LAN Properties

- a. Disable all items except the 'Internet Protocol (TCP/IP)' by un-checking the tick boxes.
- b. Click the configure option and select the advanced tab. Set the 'Connection type' to '1000Mbps Full 'duplex' and the receive buffer to the maximum value (256). See Figure 6. Then highlight the section titled 'Jumbo Frame Support' and set to enable. NOTE: This parameter is a new addition for the latest versions of the LAS and Vanilla systems. Close the adaptor properties window by clicking 'Ok'.

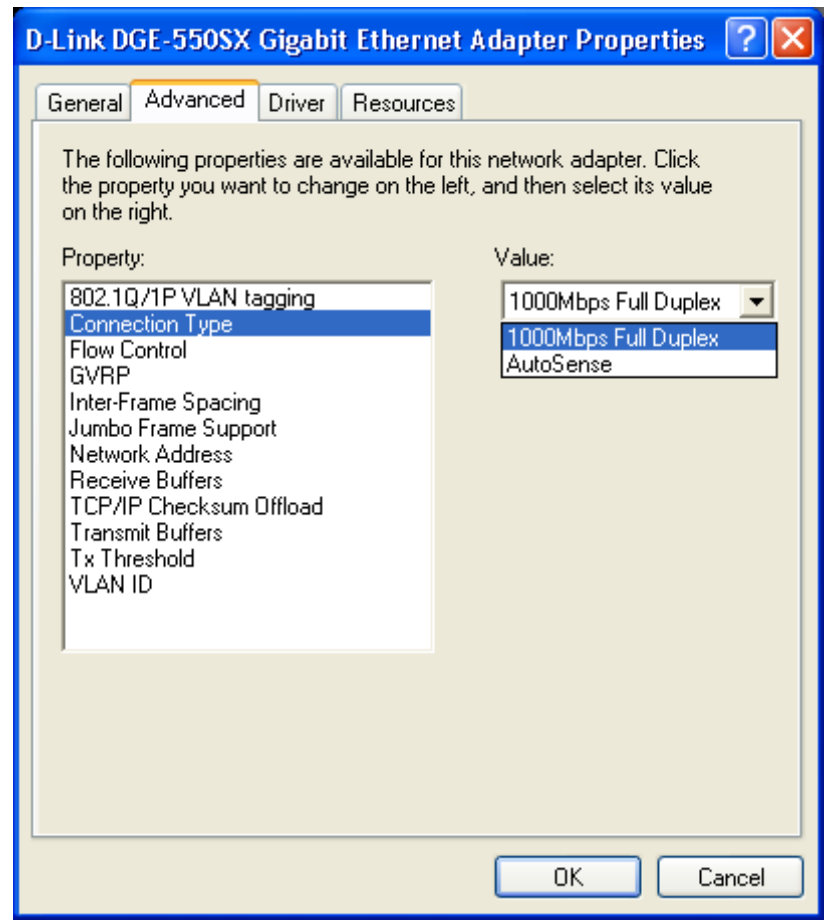


Figure 6 - LAN Adaptor Advanced Properties

- c. Highlight the 'Internet Protocol (TCP/IP)' connection and open the properties. Specify the IP address manually to be '192.168.0.1' and the Subnet Mask 255.255.255.0. Close the TCP/IP properties window by clicking 'Ok'.
- d. Make sure the tick box 'Show icon in notification area when connected' is set. Close the connection properties window by clicking 'Ok'.
- e. It is recommended that you rename the connection to 'OptoDAQ' at this point.
- 3. Restart computer.
- 4. In order to protect against having several versions of the DLL on the same machine the OptoDAQ DLL location is fixed to C:/MI3/OptoDAQ/General. The following files should be copied to this directory from the LAS Software V1 2.zip:-

```
Quixtream.dll
mi3_las.dll
mi3_las.h
mi3_las.lib
optodaq-LAS-V1_2.xml
```

The LAS distribution will work alongside an older style sensor distribution with files named just 'mi3.dll'. But is you wish to run multiple older sensors you will have to keep the second 'mi3.dll' file in an alternative location as before. The viewer file 'las_viewer_V1_2.exe' should be placed in a different location in a LAS specific area.

5. Right click on the My Computer icon on the desktop. Select Properties / Advanced. Select Environment Variables and add a user variable 'Path' containing the path to the file (e.g. c:/MI3/OptoDAQ/General). See Figure 7. Note: If you which to allow the setup to be used by all user of the PC the path should instead be added to the end of the System Variable 'Path'. N.B. If the variable path already exists the directory should be appended to the list.

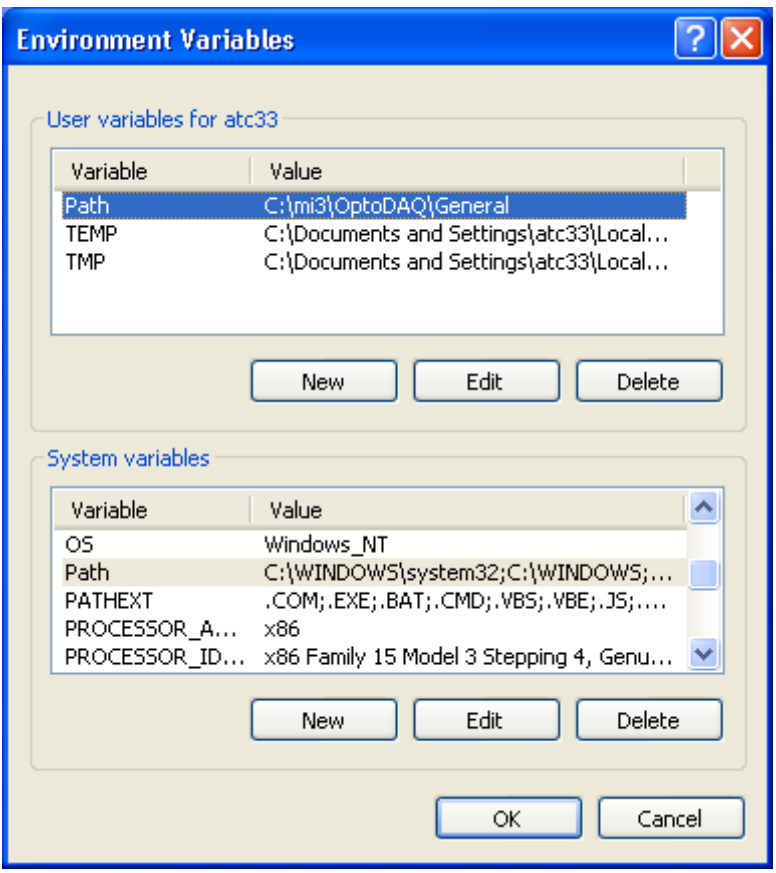


Figure 7 - Setting the path

6. To avoid recompiling the DLL for each specific host the communication settings are specified in an XML file. In order to setup the system on a specific host the MAC address of the optical Ethernet card needs to be specified. To establish the MAC (or Physical) address of your network card; run 'ipconfig /all' from a windows command prompt (see Figure 8). NOTE: Make sure to use the physical address for the optical network adapter, not that of you LAN adapter. You can also check that the card is configured properly by verifying the IP address you specified in step 2b is also present.

Figure 8 - IPConfig settings

The MAC address found under the OptoDAq connection should be substituted into line 20 of 'Setup_UDP.xml' as shown below:-

20: <MACAddress value="00-0D-88-7F-C2-55"/>

The system is now ready to be used.

4. OUTPUT FILE FORMAT

The file format produced by the DLL has been simplified for the LAS release. It is now a basic raw format which can be opened in tools such as Image J or even programmes such as Photoshop. To open the file in such programmes the user is usually prompted for some information on the file format, this information is shown in Table 6.

Parameter	Value
Number of Rows	1350 (Depending on ROI)
Number of Columns	1350 (Depending on ROI)
Header size at start of file	4 Bytes if Frame Numbers were selected
	otherwise 0 Bytes
Header size between frames	4 Bytes if Frame Numbers were selected
	otherwise 0 Bytes
Number of frames in file	Defined by the user before capture
Data Format	16bit Unsigned
Data Endian	Little Endian

Table 6 - File Format Parameters

Many of these values apart form the endian and the data format which are constant can be found in the corresponding text file which is saved alongside each data file. An example of the parameters entered into Image J is shown in Figure 9

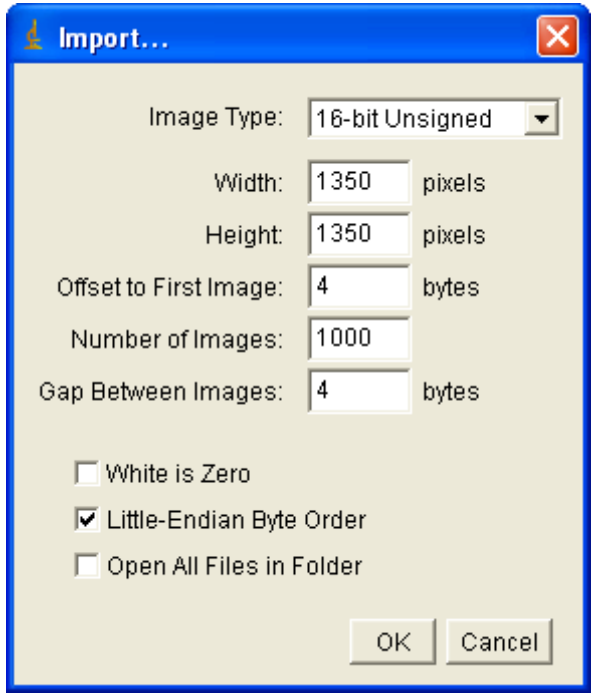


Figure 9 - Image J Import Settings

To read in the data manually into a program such as Matlab or LabView, you will need much of the same information. The pixel data is stored in the file on a row by row basis, each pixel value stored in a 16bit unsigned word. You may find it useful to verify the frame numbers (if enabled), checking they contain incremental integers, as testing for this is a great way to do some form of automated checking for any data corruption which although rare, may occur from time to time.

Appendix C

MATLAB MTF code

```
tic
%clear the memory first - good practice.
clear all
peds = dlmread('C:\Documents and Settings\Fvy38621\My Documents\RAL documents\Detector
Devision\MatLab images and code\LAS W3-3\9.8fps\dark_pedestal.txt');
% pedsa = dlmread('C:\Documents and Settings\Fvy38621\My Documents\RAL documents\Detector
Devision\MatLab images and code\FOS\20kV_10mA\skull_light_pedestal.txt');
all_files = zeros(1350,1350);
num_frames = 10;
mem_step = 20;
im = zeros(1350,1350);
sum_data= zeros(1350,1350);
for file_num=1
  % open the folder containing the .raw files
  folder='C:\Documents and Settings\Fvy38621\My Documents\RAL documents\Detector
Devision\MatLab images and code\LAS W2-2\ACS\20fps\MTF(125%)\';
  % open the file
  file_name = [folder '40kV_50mA_data.raw'];
  fid = fopen(file_name,'r');
  %read the rest of the data out of the file
  for j=1:10
```

fseek(fid, 4, 'cof');

```
raw_data = fread(fid,1350*1350,'uint16');
    %reshape the data into 1350x1350 pixels
    im(:,:,j) = reshape(raw_data,1350,1350);
    %flip to get the correct orientation
    im(:,:,j) = im(:,:,j)'-peds;
    clear raw_data
  end
  ave_im(:,:) = mean(im, 3);
  % close the file
  fclose(fid);
end
image = mean(ave_im, 3);
image(1,:)=image(2,:);
image(360:380,:)=image(330:350,:);
image(784,:)=image(782,:);
image(795,:)=image(793,:);
image(1218,:)=image(1216,:);
%image(1300:1340,1:600)=image(1240:1280,1:600);
image(:,571)=image(:,570);
%get data from multiple columns like Fujita
colmin=635;
```

```
colmax=641;
ESF = zeros(length(image(:,1))*(colmax-colmin),1);
for p=colmin:colmax
  for r=1:length(image(:,1));
    ESF(r+(((colmax-colmin)*(r-1))+(p-colmin))) = image(r,p);
  end
end
z=1;
for n=2:1:length(ESF)-1;
  ESFsmooth(z)=mean(ESF(n-1:n+1));
 z=z+1;
end
ESFsmooth2=ESFsmooth;
for w=1:20
  a=1;
  for n=11:1:length(ESFsmooth2)-10;
    ESFsmooth2(a)=mean(ESFsmooth2(n-10:n+10));
    a=a+1;
  end
  ESFsmooth2(length(ESFsmooth2)-19:length(ESFsmooth2))=[];
end
b=1;
```

```
step=4;
for n=step+1:1:(length(ESF)-step);
  dydx(b)=(ESF(n+step)-ESF(n-step))/(2*step+1);
  b=b+1;
end
c=1;
step=4;
for n=step+1:1:(length(ESFsmooth2)-step);
  dydxsmooth(c)=(ESFsmooth2(n+step)-ESFsmooth2(n-step))/(2*step+1);
  c=c+1;
end
[r,peak,v] = find(dydxsmooth == max(dydxsmooth));
peak_high=peak+300;
peak_low=peak-300;
peak_diff=peak_high-peak_low;
dydxsmooth_normalised = dydxsmooth(peak_low:peak_high)/max(dydxsmooth);
mtf=fft(dydxsmooth_normalised);
mtf_normalised = mtf/max(mtf);
% mtf2=fft(dydxsmooth);
image(:,678)=image(:,679);
image(:,543)=image(:,544);
%plot the image
```

```
figure(6)
imagesc(image)
colormap('gray')
axis square
3;
xax2= 201*(1/(colmax+1-colmin))*40*10^-3:(1/(colmax+1-colmin))*40*10^-
3:(length(image(:,1))*40*10^-3)-(202*(1/(colmax+1-colmin))*40*10^-3);
hold on
figure(7)
% plot(xax, ESF, 'r')
% hold on
plot(xax2, ESFsmooth2,'b')
% hold off
title('ESF');
xlabel('Distance (mm)');
ylabel('Output (LSB)');
%
figure(8)
% plot((1:b-1)*((40*10^-3)/7), dydx, 'r')
% hold on
plot((201:c-1+200)*((40*10^-3)/7), dydxsmooth)
% hold off
title('LSF');
xlabel('Distance (mm)');
ylabel('Output (LSB)');
```

```
figure(9)
plot((-peak_diff/2*40*10^-3)/7:(40*10^-3)/7:(peak_diff/2*40*10^-3)/7, dydxsmooth_normalised)
title('LSF');
xlabel('Distance (mm)');
ylabel('Relative Output');
xax3= 205*(1/(colmax+1-colmin))*40*10^-3:(1/(colmax+1-colmin))*40*10^-
3:(length(image(:,1))*40*10^-3)-(206*(1/(colmax+1-colmin))*40*10^-3);
figure(10)
hold on
% plot(0:length(mtf_normalised)-1,abs(mtf_normalised),'r')
plot(0:12,abs(mtf_normalised(1:13)),'black')
title('MTF');
xlabel('Spatial Frequency (cycles/mm)');
ylabel('Modulation Transfer Factor');
hold on
% plot(xax3,abs(mtf2),'r')
% hold off
```

toc

- [1] URL accessed August 2009, 2009. URL http://www.diamond.ac.uk/Home/About/Synchrotrons/Machine.html.
- [2] URL accessed August 2009, 2009. URL http://www.diamond.ac.uk/Beamlines/Beamlineplan/I12/index.htm.
- [3] Alexander Hellemans Bryan H. Bunch. The history of science and technology: A browser's guide to the great discoveries, inventions and the people who made them from the dawn of time to today. page 452, 2004.
- [4] Alexi Assmus. Early history of x rays. URL accessed September 2009:10, 1995. URL http://www.slac.stanford.edu/pubs/beamline/25/2/25-2-assmus.pdf.
- [5] History of radiography. URL accessed September 2009, 2009. URL http://www.ndt-ed.org/EducationResources/CommunityCollege/Radiography/Introduction/history.htm.
- [6] A. Gektin Peter Capper. Bulk crystal growth of electronic, optical and optoelectronic materials. page 357, 2005.
- [7] URL accessed September 2009, 2009. URL http://www.xrfcorp.com/technology/radiation_detection.html.
- [8] Glenn F. Knoll. Radiation detection and measurement. 3rd edition, John Wiley and Sons Inc. 0-471-07338-5, 2000.
- [9] Gopal B. Saha. Physics and radiobiology of nuclear medicine. 3rd edition:81–86, 2006.
- [10] Kenneth S. Krane. Introductory nuclear physics. John Wiley and Sons Inc, 0-471-80553-X, 1988.
- [11] Applied Techniques Co. Operations manual; dual radon counting system. URL accessed October 2009, September 2009. URL http://www.atral.com/operationsmanual1.html.

[12] Ralph Etienne-Cummings Orly Yadid-Pecht. Cmos imagers: From phototransduction to image processing. page 99, 2004.

- [13] Eric R. Fossum. Active pixel sensors: Are ccd's dinosaurs? Proceedings of SPIE, Vol. 1900:2–14, 1993.
- [14] Gene P. Weckler Rudolph H. Dyck. Integrated arrays of silicon photodetectors for image sensing. *IEEE*, URL accessed September 2009:196–201, 2009. URL http://ieeexplore.ieee.org/stamp/stamp.jsp?arnumber=1475068&isnumber=31645.
- [15] G. Wang D. Renshaw, P. B. Denyer and M. Lu. Asic image sensors. *IEEE*, 1990.
- [16] STFC Technology Department. Project specification high energy pixel detector for i12. Project Specification version: 1.2, page 10, August 2009.
- [17] Matthew Wilson. Expected performance of l-axis detector for i12. page 4, August 2009.
- [18] URL accessed October 2009, 2009. URL http://hyperphysics.phy-astr.gsu.edu/Hbase/quantum/xtube.html.
- [19] Syed Naeem Ahmed. Physics and engineering of radiation detection. Academic Press Inc., Great Britain 0-12-045581-1, 2007.
- [20] Xcom: Photon cross sections database. URL accessed November 2009, 2009. URL http://www.vifaphys.de/fi.php?mode=classification&lang=en&skin=gui&action=object_info&ID=682.
- [21] George G. Guilbault. Practical fluorescence. 0-8247-8350-6:5, 1990.
- [22] Joseph R. Lakowicz. Principles of fluorescence spectroscopy. page 1, 2006.
- [23] T. Jing et al. Detection of charged particles and x-rays by scintillator layers coupled to amorphous silicon photodiode arrays. Nuclear Instruments and Methods in Physics Research, 1st edition:757–764, 1996.
- [24] URL accessed October 2009, 2009. URL http://www.scionixusa.com/pages/navbar/scin_crystals.html.
- [25] Piotr A. Rodnyi. Physical processes in inorganic scintillators. CRC Press LLC, Florida USA, 0-8493-3788-7, 1997.
- [26] N.F. Mott R.W. Gurney. Luminescence In Solids, June 1938.
- [27] M.P. Kalashnikov et al. Investigation of CsI(Tl) scintillation properties at high intensity of pulse flux of X-ray radiation, 1983.

[28] Orly Yadid-Pecht Alexander Fish. Cmos imagers: From phototransduction to image processing. Kluwer Academic Publishers, The Netherlands 1-4020-7962-1, 2004.

- [29] Sarah E. Bohndiek. Active pixel sensors for breast biopsy analysis using x-ray diffraction. 2008.
- [30] U.Goerlach et al. Monolithic active pixel sensors for high resolution vertex detectors. URL accessed November 2009, 2009. URL http://ph-collectif-lecc-workshops.web.cern.ch/ph-collectif-lecc-workshops/leb00_book/posters/goerlach.pdfaccessedNovember2009.
- [31] W. Dulinski et al. Cmos monolithic active pixel sensors for minimum ionizing particle tracking using non-epitaxial silicon substrate. *IEEE TRANSACTIONS* ON NUCLEAR SCIENCE, VOL. 51, NO. 4, 2004.
- [32] N. Allinson et al. The multidimensional integrated intelligent imaging project (mi-3). Nuclear Instruments and Methods in Physics Research A, 2009.
- [33] Sarah E. Bohndiek et al. Characterization and testing of las: A prototype 'large area sensor' with performance characteristics suitable for medical imaging applications. *IEEE TRANSACTIONS ON NUCLEAR SCIENCE*, 56 (5, Part 2):2938– 2946, 2009.
- [34] Andy T. Clark et al. A 54mm x 54mm 1.8megapixel cmos image sensor for medical imaging. IEEE TRANSACTIONS ON NUCLEAR SCIENCE, pages 4540–4543, 2008.
- [35] URL accessed November 2009, 2009. URL http://www.allaboutcircuits.com/vol_4/chpt_13/5.htmlaccessedNovember2009.
- [36] W.J. Walker. Sampling theory in fourier and signal analysis: Advanced topics. Thomson Press Ltd, India 0-19-853496-5, 1999.
- [37] Peter W. Hawkes. Advances in electronics and electron physics. 89th volume, Academic Press Inc. 0-12-014731-9, 1994.
- [38] O. N. Morgun et al. Detective quantum efficiency as a quality parameter of imaging equipment. *Biomedical Engineering, Vol. 37, No. 5*, pages 258–261, 2003.
- [39] Hamamatsu Photonics Inc. X-ray scintillator. URL accessed August 2009 to January 2010, 2010. URL http://sales.hamamatsu.com/assets/pdf/ catsandguides/ACS_ALS_FOS_TMCP1031E04.pdf.
- [40] H. Fujita *et al.* A simple method for determining the modulation transfer function in digital radiography. 0278-0062/92 1992 IEEE, pages 34–39, 1992.

[41] C. Ponchut. Characterization of x-ray area detectors for synchrotron beamlines. 0909-0495 2006 Synchrotron Radiation, pages 195–203, 2006.

- [42] C. M. Pepin et al. Assessment of quick-stick 5870 high refractive index thermoplastic coupling compound. Nuclear Instruments and Methods in Physics Research A 488, page 670672, 2002.
- [43] M. Hjelm et al. Monte carlo simulation of the imaging properties of scintillatorcoated x-ray pixel detectors. Nuclear Instruments and Methods in Physics Research A 509, pages 76–85, 2003.
- [44] M. Balcerzyk et al. Perspectives for high resolution and high light output luap:ce crystals. 0-7803-8700-7/04 2004 IEEE, pages 986–992, 2004.